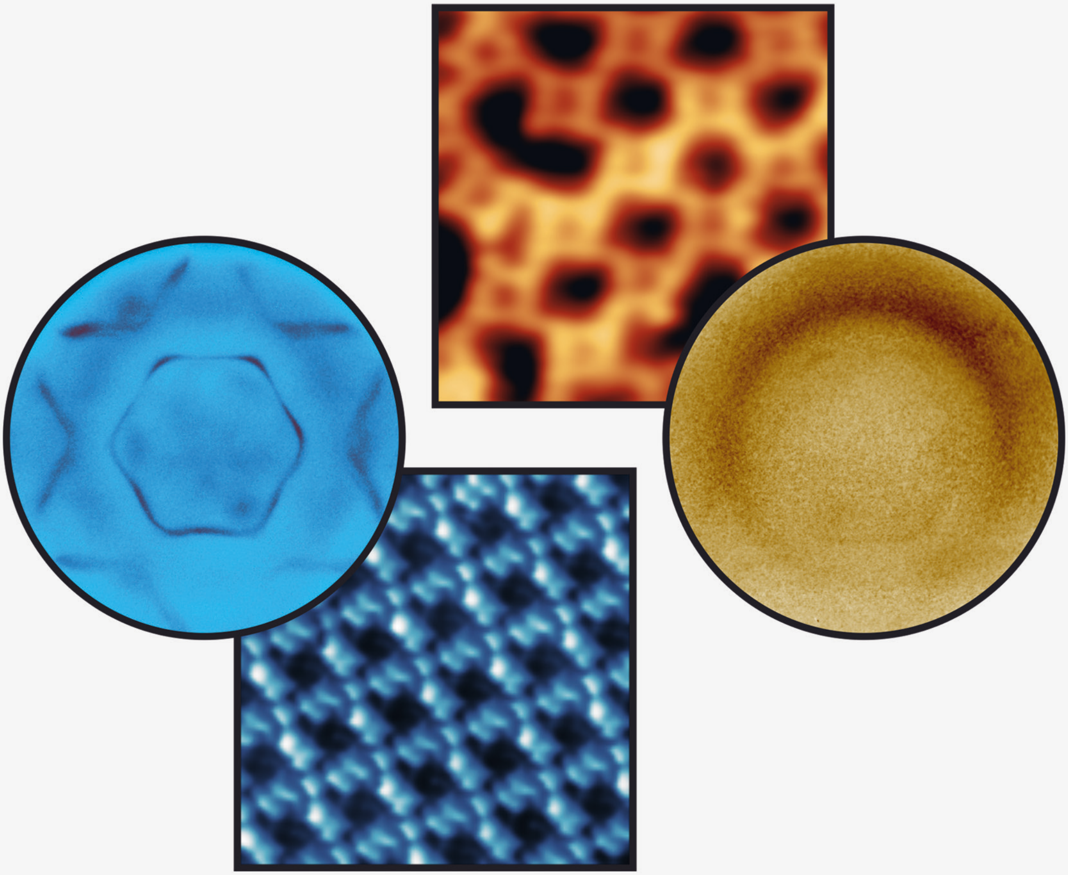

Probing the Transformation from Transition Metal Complexes to Extended Two-Dimensional Nanostructures

Daniel Baranowski

Schlüsseltechnologien / Key Technologies
Band / Volume 284
ISBN 978-3-95806-772-1

Mitglied der Helmholtz-Gemeinschaft

JÜLICH
Forschungszentrum

Schriften des Forschungszentrums Jülich
Reihe Schlüsseltechnologien / Key Technologies Band / Volume 284

Forschungszentrum Jülich GmbH
Peter Grünberg Institut (PGI)
Elektronische Eigenschaften (PGI-6)

Probing the Transformation from Transition Metal Complexes to Extended Two-Dimensional Nanostructures

Daniel Baranowski

Schriften des Forschungszentrums Jülich
Reihe Schlüsseltechnologien / Key Technologies Band / Volume 284

ISSN 1866-1807 ISBN 978-3-95806-772-1

Bibliografische Information der Deutschen Nationalbibliothek.
Die Deutsche Nationalbibliothek verzeichnet diese Publikation in der
Deutschen Nationalbibliografie; detaillierte Bibliografische Daten
sind im Internet über http://dnb.d-nb.de abrufbar.

Herausgeber und Vertrieb: Forschungszentrum Jülich GmbH
Zentralbibliothek, Verlag
52425 Jülich
Tel.: +49 2461 61-5368
Fax: +49 2461 61-6103
zb-publikation@fz-juelich.de
www.fz-juelich.de/zb

Umschlaggestaltung: Grafische Medien, Forschungszentrum Jülich GmbH

Druck: Grafische Medien, Forschungszentrum Jülich GmbH

Schriften des Forschungszentrums Jülich
Reihe Schlüsseltechnologien / Key Technologies, Band / Volume 284

D 464 (Diss. Duisburg-Essen, Univ., 2024)

ISSN 1866-1807
ISBN 978-3-95806-772-1

Ich habe fertig.

Giovanni Trapattoni

Table of Contents

Abstract

The controlled on-surface stabilization of functional transition metal centers can be realized by embedding them in a coordination environment of an organic backbone. Then, realizing two-dimensional materials with improved stability and novel properties is possible through the careful design of the organic backbone. An understanding of the changes induced by the transition from isolated transition metal-organic complexes to their extended structures has been defined as the subject of this work. Thereby, transition metal-containing covalent networks and metal-organic frameworks have been realized.

Starting from nickel tetraphenylporphyrin polymers, the emergence of π-delocalization in the molecular backbone as a consequence of polymerization has been confirmed by the appearance of energy-dispersive electronic valence states. This is quite surprising since the polymers have been determined to be amorphous by scanning tunneling microscopy measurements. Simultaneously, a defined functionality of the nickel centers has been observed during spectroscopic characterization. The two-dimensional nickel-containing polymers can be tuned by the reactivity of the surface used for their stabilization. Though indicated by the results obtained via theoretical modeling, the energy-dispersive nature of the nickel $3d$-based valence states has turned out as experimentally not accessible.

To mimic the functional center of nickel tetraphenylporphyrin, the transition from nickel 1,2,4,5-tetracyanobenzene complexes to two-dimensional metal-organic framework has been realized. Thereby, the energy level alignment can be adjusted to enable experimental access to the nickel $3d$-based valence states. The appearance of π-conjugation for the nickel $3d$-based valence states upon formation of the polymeric structure has been clearly confirmed following the same multi-technique approach applied for the characterization of covalent nickel tetraphenylporphyrin networks.

Kurzzusammenfassung

Die kontrollierte Stabilisierung funktioneller Übergangsmetallzentren auf Oberflächen lässt sich über deren Einbettung in eine Koordinationsumgebung realisieren. Durch die sorgfältige Gestaltung des organischen Grundgerüsts lassen sich zweidimensionale Materialien mit verbesserter Stabilität und neuartigen Eigenschaften herstellen. Das Verständnis der Veränderungen, die durch den Übergang von isolierten Übergangsmetallkomplexen zu deren Polymeren hervorgerufen werden, stellt den Gegenstand dieser Arbeit dar. Dabei wurden kovalente Netzwerke und metallorganische Gerüstverbindungen realisiert.

Bei der Polymerisation von Nickel-Tetraphenylporphyrin-Molekülen konnte das Auftreten von π-Konjugation festgestellt werden. Diese äußert sich über energiedispersive Valenzzustände des organischen Rückgrats, obwohl sich die Polymere in Rastertunnelmikrokopiemessungen als amorph herausgestellt haben. Gleichzeitig wurde bei der spektroskopischen Charakterisierung eine definierte Funktionalität der Nickelzentren beobachtet. Die Eigenschaften der kovalenten nickelhaltigen Polymere lassen sich über die Reaktivität der zu ihrer Stabilisierung verwendeten Oberfläche beeinflussen. Obwohl die Ergebnisse der theoretischen Modellierung darauf hindeuten, hat sich die energiedispersive Natur der Nickel 3*d*-basierten Valenzzustände als experimentell nicht zugänglich erwiesen.

Um das Übergangsmetallzentrum von Nickel-Tetraphenylporphyrin zu imitieren, wurde der Übergang von Nickel-1,2,4,5-Tetracyanobenzol-Komplexen zu zweidimensionalen metallorganischen Gerüstverbindungen realisiert. Dabei kann die Position der Energieniveaus so angepasst werden, dass eine experimentelle Charakterisierung der Nickel 3*d*-basierten Valenzzustände möglich ist. Das Auftreten von π-Konjugation für einzelne Nickel 3*d*-basierte Valenzzustände bei der Bildung der Polymerstruktur wurde eindeutig bestätigt. Dabei wurde der selbe Ansatz wie bei der Charakterisierung von kovalenten Nickel-Tetraphenylporphyrin-Netzwerken gewählt.

Abbreviations and Symbols

2D	Two-dimensional
$\vec{a}$	Basis vector
$\vec{A}$	Vector potential
B	Magnetic field
CN	Cyano
CNL	Charge neutrality level
DFT	Density functional theory
DOS	Density of states
dI/dV	Differential conductance
ESCA	Electron spectroscopy for chemical analysis
EA	Electron affinity
E	Energy
E_B	Binding energy
E_F	Fermi level
E_kin	Kinetic energy
E_vac	Vacuum level
e	Elementary charge
$\vec{g}$	Reciprocal basis vector
$\vec{G}$	Reciprocal lattice vector
HOMO	Highest occupied molecular orbital
h	Planck constant
IDIS	Induced density of interface states
IE	Ionization energy
I	Current
k	Wave vector
LEED	Low-energy electron diffraction
LT	Low-temperature
LUMO	Lowest unoccupied molecular orbital
λ	Wavelength
ML	Monolayer
MO	Molecular orbital
MOF	Metal-organic framework
m_e	Electron mass
m_l	Orbital magnetic quantum number

$\boldsymbol{M}$	Matrix element/Magnetization
$\boldsymbol{\mu}$	Magnetic moment
NEXAFS	Near edge x-ray absorption fine structure
NiTBrPP	Nickel tetra(4-bromophenyl)porphyrin
NiTPP	Nickel tetraphenylporphyrin
$^{\mathbf{NM}}\mathbf{I}$	Nalewajski-Mrozek bond multiplicity index
$\boldsymbol{n}_{\mathbf{h}}$	Number of holes
$\boldsymbol{\nu}$	Light frequency
$\boldsymbol{\omega}$	Transition probability
pDOS	Projected density of states
PDOS	Partial density of states
PEEM	Photoelectron emission microscop(e, y)
POT	Photoemission orbital tomography
$\boldsymbol{p}$	Momentum
$\boldsymbol{P}$	Electric polarization
$\mathbf{\Phi}$	Barrier height
$\mathbf{\Phi}_{\mathbf{i}}$	Work function of i
RKKY	Ruderman–Kittel–Kasuya–Yosida
$\boldsymbol{r}$	Space
STM	Scanning tunneling microscop(e, y)
$\boldsymbol{S}$	Molecular spin
TCNB	1,2,4,5-tetracyanobenzene
TCNQ	7,7,8,8-tetracyanoquinodimethane
TM	Transition metal
$\boldsymbol{t}$	Time
$\boldsymbol{T}$	Temperature
$\boldsymbol{\theta}$	Angle with respect to the surface normal
UHV	Ultra-high vacuum
VB	Valence band
$\boldsymbol{V}$	Voltage
$\boldsymbol{V}_{\mathbf{0}}$	Inner potential
XMCD	X-ray magnetic circular dichroism
XPS	X-ray photoelectron spectroscopy
$\boldsymbol{Z}$	Atomic number

1 Introduction

The bottom-up approach allows obtaining extended nanostructures free from solubility limitations characteristic of traditional synthesis approaches. Thereby, control at the atomic/molecular scale has been realized by confining the self-assembly process of building units to two dimensions at a solid surface, typically under ultra-high vacuum (UHV) conditions.[1,2] Customizing the functional properties of transition metal (TM) centers within miniaturized devices is particularly interesting for catalysis,[3] sensing,[4] and spintronics.[5] Integrating TMs into a specified coordination environment provided by an organic backbone has been established as a strategy for tailoring their oxidation and spin state.[6] Introducing the organic functionality into the system permits regulating the interaction with the substrate used for stabilization, thereby modulating the reactivity of the TM center and controlling magnetic coupling with magnetic supports.[7,8]

TM-containing porphyrin molecules are prominent building blocks in this context, as they combine chemical and thermal stability with structural versatility, offered by programmable substituents.[9,10] The peripheral substitution of porphyrins has been used to design the first monomer units, suitable for covalent on-surface Ullmann polymerization.[11] The technological exploitation of advanced nanoarchitecture concepts relies on more robust nanostructures, composed of covalently linked units.[12] On-surface synthesis is the method of choice in order to achieve π-conjugated conductive covalenty bound nanomeshes with red-shifted absorption characteristics at the interface.[13–15] Covalent TM-containing porphyrin-based catalytic materials, which exhibit improved charge transport and carrier separation properties, have been proven to outperform their single-molecule counterparts in chemical conversion reactions.[16,17] Specifically for the case of two-dimensional (2D) TM-containing porphyrin polymers, it has been demonstrated that they resist exposure to ambient conditions.[18] Insights gained from studies under UHV conditions, therefore, may serve as interesting platform in device design. Previous studies have primarily addressed the properties of these macromolecular compounds by means of local probe methods. Approaches combining local insights with space-averaging techniques have either been limited to TM-free porphyrin materials or have not included the functional properties of the ligated TMs provided by covalent metalloporphyrin networks. This has been the motivation for the studies presented in chapter 4, where covalent nickel tetraphenyl porphyrin (NiTPP) networks are compared to their single-molecule counterparts, further elucidating how the reactivity of the supporting substrate can be rationalized in tuning their functional properties. Particular focus has been put onto the emergence of π-delocalization as a consequence of polymerization, which is surprisingly evident despite deviations from perfect order inherent to the applied coupling scheme.

2D metal-organic frameworks (MOFs) represent another category of atomically thin materials, wherein organic ligands interconnect TM centers to form the extended structures, allowing to mimick the coordination pocket characteristic of NiTPP. Given the reversibility of metal-ligand interactions the self-assembly process yields well-ordered systems, which combine the structural tunability of molecular systems with the crystalline structure characteristic of solids.[19,20] 2D-MOFs have nevertheless been demonstrated to withstand realistic application as catalytic materials, even after UHV synthesis.[21] Furthermore, the synthesis of single-layer 2D-MOFs under ambient conditions has been recently demonstrated.[22] High-precision UHV synthesis and characterization can, thus, be considered representative for 2D-MOFs of practical relevance. In this context, a thorough understanding of the interaction between the TM's $3d$ states and the π states of the ligand is critical, defining the electronic delocalization effects within the materials, and, thus, their functionality.[23–25] Specifically, π-conjugated MOFs offer exciting properties as high electric conductivity,[26] or superconductivity,[27] to ferromagnetism.[28] 2D-MOF topological insulators have also been predicted.[29–33] Studies concerning the band structures of on-surface stabilized MOFs are just emerging.[24,25,34–38] Understanding how band dispersion emerges in 2D-MOFs upon coupling of building blocks is crucial for advancing materials design, enabling targeted manipulation of electronic properties for tailored applications. Mimicking the coordination sphere, characteristic of TM-containing porphyrins, the studies presented in chapter 5 have been performed for this reason. Combining Ni and 1,2,4,5-tetracyanobenzene (TCNB) allows a hierarchical self-assembly protocol from isolated metal-organic complex to the extended 2D-MOF, for which π-delocalization emerges and persists upon tuning the periodic Ni-TCNB framework at more reactive surfaces.

This work is organized as follows: In chapter 2, the theoretical background of the (metal-)organic metal interface and the experimental characterization methods will be introduced, followed by the experimental details in chapter 3. The main findings on NiTPP-based covalent networks and metal-organic structures based on Ni and TCNB will be presented in chapter 4 and chapter 5. This dissertation is partially based on three manuscripts and my contributions to the respective works will be specified in the beginning of chapter 4 and chapter 5.[39–41]

2 Theoretical Background

This chapter introduces the general properties of adsorbed (metal-)organic nanostructures stabilized on the surfaces of metal single crystals, prior to presenting the fundamentals on the experimental methods used for their characterization.

2.1 The (Metal-)Organic/Metal Interface

Miniaturizing functional devices relies on understanding of the (metal-)organic/metal interface, defining the characteristic energy E level alignment and transport properties. In the Schottky-Mott regime, the formation of a contact between the (metal-)organic layer and the metal support results in vacuum level E_{vac} pinning. There is a weak interaction between the constituents of the interface, but the (metal-)organic nanostructure is influenced by the surface dipole, which is a consequence of the spill out of charge due to the broken translation symmetry. This results in a reordering of the (metal-)organic energy levels at the interface E_{vac} with respect to the E_{vac} at infinite distance.[42] In this regime free of charge redistribution, the work function of the metal Φ_{metal}, the electron affinity (EA) and ionization energy (IE) define the binding energy (E_{B}) of the frontier molecular orbitals (MOs). The E_{B} of the lowest unoccupied and highest occupied MO (LUMO, HOMO) are then following the relations:

$$E_{\mathrm{B}}^{\mathrm{LUMO}} = \Phi_{\mathrm{metal}} - \mathrm{EA}; \tag{2.1}$$

$$E_{\mathrm{B}}^{\mathrm{HOMO}} = \mathrm{IE} - \Phi_{\mathrm{metal}}. \tag{2.2}$$

The energy level alignment for the vacuum level pinning regime is displayed in figure 2.1a. Usually, the charge spilled out at the surface of the supporting metal is influenced by the stabilized (metal-)organic layer. This situation is referred to as the pushback effect, resulting in a work function of the interface $\Phi_{\mathrm{interface}}$, reduced with respect to Φ_{metal} due to an interface dipole. $\Phi_{\mathrm{interface}}$ is further determined by the interaction between the surface and the (metal-)organic nanostructure, possibly accompanied by a charge transfer at the interface expressed as an occupation of the former LUMO.[43] In this context, the concepts of the induced density of interface states (IDIS) and the charge neutrality level (CNL) have been explored.[44] The interaction between the (metal-)organic nanostructure and substrate leads to a broadening of the levels of the supported layer (IDIS) at the interface. Similar to the Fermi level E_{F} in metals, the CNL describes the effective E_{F} of the IDIS. After stabilization of the (metal-)organic nanostructure accompanied by the pushback effect, the relative energy difference between its CNL and the E_{F} of the surface is compensated by the flow of charge. This is referred to as Fermi level pinning, ultimately defining the interface dipole and $\Phi_{\text{interface}}$ (see figure 2.1, showing the case before alignment of E_F and CNL). Real systems typically are characterized by properties between the two extreme cases of vacuum and Fermi level pinning.[43]

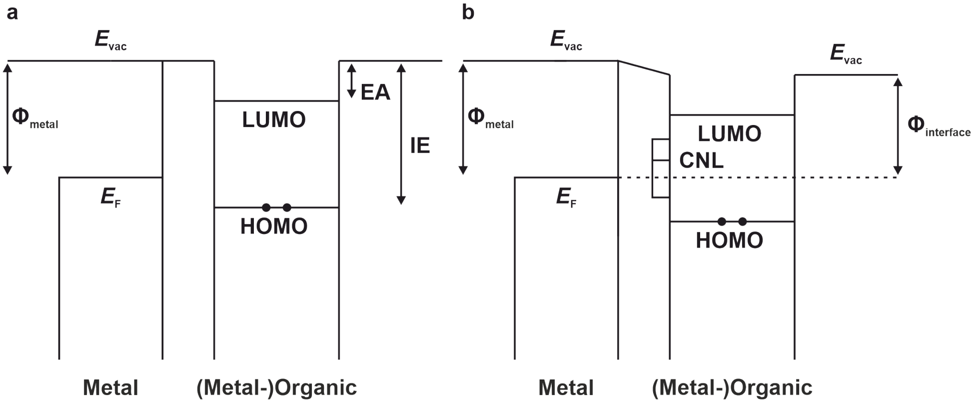

Figure 2.1: Schematic of the **(a)** E_vac and **(b)** E_F pinning at the (metal-)organic/metal interface. Replicated with adaptions from **(a)** [42] and **(b)** [44].

The stabilization of a TM-organic complex on a surface can be interpreted as introducing an axial ligand in the coordination sphere of the TM center. This additional ligand influences the energy level alignment characteristic of non-degenerate $3d$-based molecular states and can even change the oxidation state of TM ions.[45] The molecular spin S generally is determined by the ligand field splitting. The spin-orbit interaction induced magnetic anisotropy can then be treated as a small perturbation to the ligand field, which results in anisotropic g-factors as well as zero-field splittings for $S \geq 1$.[46] The axial influence of the surface is further important in the reactivity characteristic of TM-organic complexes, which is referred to as the surface trans effect.[47]

2.2 X-ray Spectroscopies of Adsorbed (Metal-)Organic Layers

In x-ray absorption and photoelectron spectroscopy, transitions from an initial state to a final state induced by the absorption of light are used to gain insights into the electronic properties of the sample of interest. The final states are either an unoccupied bound valence state or a photoionized system with a photoelectron escaping the sample. In both cases, Fermi's golden rule describes the transition probability ω_if in terms of a perturbation operator H' as:

$$\omega_\text{if} = \frac{2\pi}{\hbar} \cdot | \underbrace{\langle \Psi_\text{f} | H' | \Psi_\text{i} \rangle}_{=M_\text{if}} |^2 \cdot \delta(E_\text{f} - E_\text{i} - h\nu), \tag{2.3}$$

$$H' \propto \vec{A} \cdot \vec{p}. \tag{2.4}$$

Thereby, $\hbar$, $\vec{A}$ and $\vec{p}$ denote the reduced Planck constant, the vector potential of the electric field and the momentum operator. The δ function ensures energy conservation, with the photon energy described by the Planck constant h and the light frequency ν. In the dipole approximation, considering the large wavelength λ of the electromagnetic radiation compared to inter-atomic distances allows to simplify the matrix element M_{if} as:

$$M_{\mathrm{if}} \propto \langle \Psi_{\mathrm{f}} | \vec{P} \cdot \vec{r} | \Psi_{\mathrm{i}} \rangle \,. \tag{2.5}$$

Thereby, $\vec{P}$ and $\vec{r}$ denote the electric polarization vector and the space operator. By evaluating the matrix elements, the dipole selection rules can be formulated.[48,49]

2.2.1 Photoelectron Spectroscopy

Photoelectrons created by exposing a sample to electromagnetic radiation provide information sensitive to the electronic properties and the chemical composition of the specimen under investigation. Siegbahn has pioneered this powerful surface characterization tool and referred to it as electron spectroscopy for chemical analysis (ESCA) and received the 1981 Nobel prize in physics.[50] For historical reasons valence band (VB) photoemission experiments using ultraviolet light and core level x-ray photoelectron spectroscopy (XPS) are still distinguished from each other, even with tunable synchrotron light sources available. This convention is kept in this work to highlight the difference between delocalized frontier electronic states and tightly bound core electrons. By means of a spectrometer, a signal proportional to the number of photoelectrons is collected as a function of their kinetic energy E_{kin} and presented as spectrum after conversion to the binding energy scale. Both sample and spectrometer are grounded, resulting in an alignment of their Fermi levels and allowing to calculate E_{B} through:

$$E_{\mathrm{B}} = h\nu - E_{\mathrm{kin}} - \Phi_{\mathrm{Spectrometer}}. \tag{2.6}$$

Thereby, h and ν denote the Planck constant and the light frequency. Knowing the work function of the spectrometer $\Phi_{\mathrm{Spectrometer}}$, E_{B} values result from the conversion of energy.[48] Photoionization is the first part in the three-step model of photoemission,[51] through which a comprehensive explanation of the features observed within a spectrum can be realized. In a simplified model of the photoionization process, referred to as one-electron approximation, the core hole after photoexcitation does not affect the remaining electron orbitals. In this frozen orbital description the binding energy corresponds to the negative orbital energy (Koopmans' theorem). Particularly for XPS measurements, the defined binding energies of the core level photoelectron lines provide element specific information due to their dependence on the atomic number Z. Initial state effects are frequently used in the frozen orbital description to denote the effect of the chemical environment an atomic species is embedded into. In fact, the binding energy value not only provides element sensitivity but, for instance, chemical shifts observed in photoelectron lines can be used to discriminate between different bonding partners and oxidation states. Initial state effects are superimposed with final state effects, reflecting the response of a many electron system to the formation of a core hole, such as screening of the core hole, asymmetric peak shapes, spin-orbit split photoelectron lines and satellite signals.[48]

The inelastic mean free path of electrons in solid matter is in the range of 5 – 20 Å for $E_{\mathrm{kin}} = 10 - 1000$ eV.[52] Photoelectrons able to leave the sample without energy losses and to contribute to specific information can only originate from the surface and near-surface layers. The provided information is, therefore, sensitive to the (metal-)organic/metal interface of interest. Photoelectrons undergoing inelastic scattering processes while traveling to the surface during the second step of the three-step model of photoemission contribute to an unspecific secondary electron background in the spectrum, increasing step-by-step for each photoelectron line.[53,54]

In the third step of the three-step model, photoelectrons escape from the surface to the vacuum. When investigating the parallel and orthogonal components of the photoelectron wave vector $\vec{k}$ in vacuum (also referred to as momentum), the following relations for the $\vec{k}$-components of the final state apply:

$$k_{||,\mathrm{f}} = k_{||,\mathrm{i}} + G_{||} = \sin(\theta) \cdot \sqrt{\frac{2m_{\mathrm{e}} \cdot E_{\mathrm{kin}}}{\hbar^2}}, \tag{2.7}$$

$$k_{\perp,\mathrm{f}} = \sqrt{\frac{2m_{\mathrm{e}}}{\hbar^2} \cdot [E_{\mathrm{kin}} \cdot \cos^2(\theta) + V_0]}. \tag{2.8}$$

Thereby, $\vec{G}$, m_{e}, $\hbar$ and θ denote a reciprocal lattice vector, the electron mass, the reduced Planck constant and the photoelectron emission angle with respect to the surface normal. Due to the broken translation symmetry at the surface, only the parallel component of $\vec{k}$ is conserved. For band mapping in solids, the inner potential V_0 has to be experimentally determined by varying the photon energy.[48] The $k_{\perp,\mathrm{f}}$ dependence has to be further treated by the one-step model, accounting for the surface potential barrier and the accurate description of the photoemission process as single event.[48,55–57] For organic molecules adsorbed on surfaces, a one-step approximation to describe constant E_{B} photoelectron $k_{||}$-distribution maps (momentum maps) based on a plane wave final state, known as photoemission orbital tomography (POT, see figure 2.2), has been proven as valuable combined experimental and theoretical approach for describing the frontier MOs of adsorbed organic molecules.[58] The photocurrent I is then proportional to the square modulus of the Fourier transform $\mathcal{F}$ of the initial state:

$$I(k_{\mathrm{x}}, k_{\mathrm{y}}) \propto |\vec{A} \cdot \vec{k}|^2 \cdot |\mathcal{F}\{\Psi_{\mathrm{i}}(k_{\mathrm{x}}, k_{\mathrm{y}})\}|^2. \tag{2.9}$$

The plane wave approximation in POT has been anticipated to validly describe momentum maps related to π-symmetric MOs of large and planar molecules, which are constituted by light atoms and arranged in ordered fashion on the supporting surface, if the angle between $\vec{A}$ and $\vec{k}$ is small. In practice, MOs are calculated for the system under investigation, followed by relating the Fourier transform of the MOs to the experimental conditions. This is done by defining a radius $k = \sqrt{(2m_{\mathrm{e}}/\hbar^2) \cdot E_{\mathrm{kin}}}$, which represents an Ewald-like sphere whose intersection points with the Fourier transform define the contributions to I, and accounting for the experimental geometry by the polarization factor $\vec{A} \cdot \vec{k}$.[59]

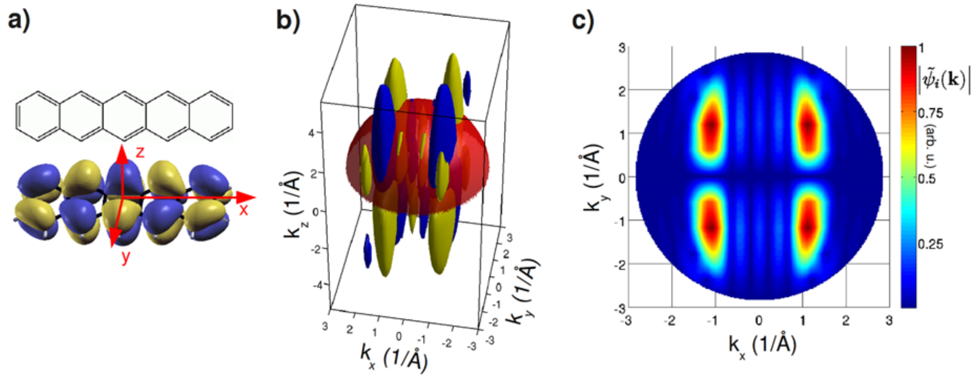

Figure 2.2: Demonstration of the POT approach from **(a)** the calculated HOMO of pentacene as initial state to the **(b)** hemispherical cut through the Fourier transform of the HOMO of pentacene, describing the **(c)** $k_{||}$-distribution characteristic of the realized experimental conditions. Note that $\mathcal{F}\{\Psi_{\mathrm{i}}(k_{\mathrm{x}}, k_{\mathrm{y}})\}$ is denoted as $\tilde{\Psi}_{\mathrm{i}}(k_{\mathrm{x}}, k_{\mathrm{y}})$. Taken from [60]. Reproduced with permission from Springer Nature.

2.2.2 Near Edge X-ray Absorption Fine Structure

In near edge x-ray absorption fine structure (NEXAFS) spectroscopy, the transitions of interest occur from core electrons to unoccupied states below the ionization threshold. NEXAFS has been developed in the 1980s as an important tool to study the orientation of on-surface stabilized (metal-)organic nanostructures. It is common to use the shell notation to classify the edges under investigation. Scanning the photon energy across the $1s$, $2p_{3/2}$ and $2p_{1/2}$ core level ionization threshold corresponds to the K-, L_3 and L_2-edge, respectively.[61] In practice, measuring a signal proportional to the emission of secondary electrons, created by filling the core hole by higher shell electrons, allows conducting surface-sensitive measurements.[62] When reaching an absorption edge, the photoelectric absorption coefficient, which generally decreases with increasing photon energies, is rapidly enhanced. There is a fine structure of resonances below the ionization threshold that corresponds to transitions into unoccupied valence states.[63] These resonances directly reflect the chemical bonding and are characterized by a pronounced charge anisotropy, resulting from σ- and π-bonding in organic molecules, as well as from the ligand field into which the $3d$-orbitals in a TM-organic complex unit are embedded.[49] The $1s$ to $2p$ (involved in σ- and π-bonding) resonances, probed across the K-edges to study organic molecules, are element specific and highly localized, as the valence state densities are accessed closely to the core of the excited electron. Therefore, the NEXAFS spectra can, to a certain extent, be understood as superposition of building blocks that constitute an organic molecule.[63,64] Due to the spherical nature of the core levels, the absorption cross section depends only on the charge distribution of the final valence states.[49] When using linearly-polarized light, the resonances observed across the K-edges are maximized in intensity, if the electric field vector of the linearly-polarized light is pointing along the charge distribution of the probed valence state.[63] For on-surface stabilized and oriented organic units this is particularly interesting, since the search light effects gives rise to pronounced linear dichroism, naturally occurring due to the different symmetries of the frontier MOs, upon changing from s- to p-polarized light, ideally with the photon impinging at grazing incidence. Evaluating the polarization and angular dependence of specific resonance intensities, then allows one to determine molecular tilts.[65,66] Similarly, the resonances in the $L_{3,2}$ spectra of on-surface stabilized TM-organic complexes are suppressed, if the electric field of linearly-polarized light is oriented along the nodal line of unoccupied $3d$-based valence states. Examples for linear dichroism observed in the NEXAFS spectra recorded across the K-edge and $L_{3,2}$-edge are displayed in figure 2.3.

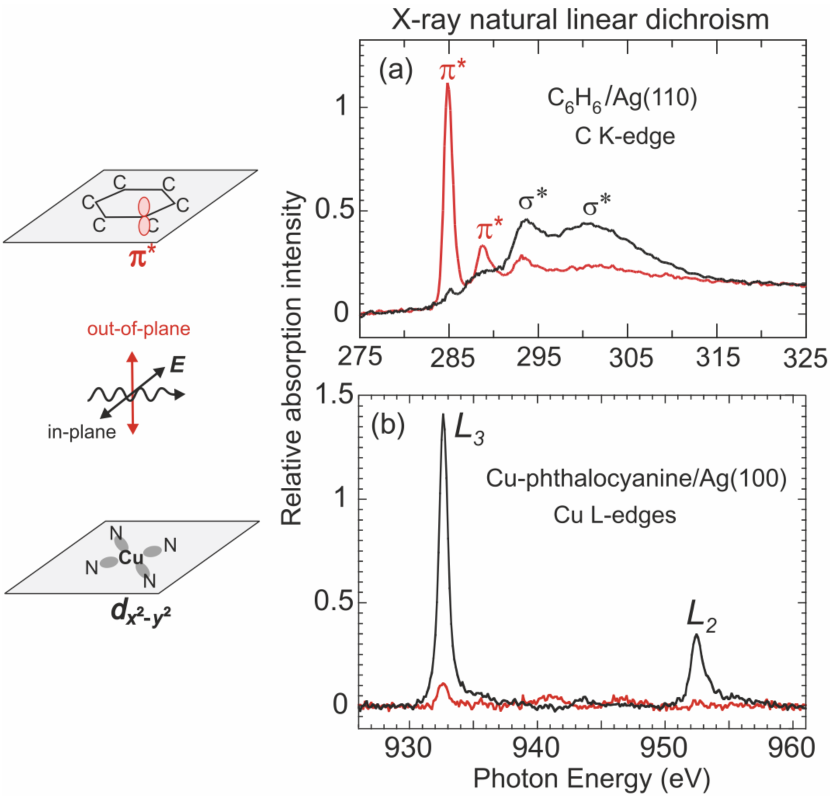

Figure 2.3: Examples for the linear dichroism that naturally occurs due to the search light effect in NEXAFS across the **(a)** K-edge for adsorbed benzene and across the **(b)** $L_{3,2}$-edge for on-surface stabilized Cu-organic complexes. Taken from [49]. Reproduced with permission from Springer Nature.

2.2.3 X-ray Magnetic Circular Dichroism

X-ray magnetic circular dichroism (XMCD), discovered by Schütz et al. in 1987,[67] has emerged as a prominent method to examine the magnetic properties of on-surface stabilized TM-organic complexes. Applying a two-step picture allows for a comprehensive understanding of the origin of the dichroic effect. Using circularly-polarized light to probe the transitions across the $L_{3,2}$-edge induces transitions of core electrons following the selection rule for the orbital magnetic quantum number $\Delta m_\mathrm{l} = 1$ (-1) for light of positive (negative) helicity. Due to spin-orbit coupling of the $2p_{3/2}$ and $2p_{1/2}$ levels a opposite spin polarization in the photoexcited core electrons can be realized for one circular polarization. The spin polarization is inverted from the L_3- to the L_2-edge, while an orbital polarization of the same magnitude is observed as well. Changing from one circular polarization to the other allows inverting the effect. The unoccupied $3d$-based levels of magnetically ordered systems with an imbalance in the density of spin up and down electrons, which for paramagnetic TM-organic complexes is achieved by cooling down the sample to low temperatures T and positioning them into an external magnetic field B, then act as detector. Consequently, a dichroism in the absorption of left and right circularly-polarized light can be observed. The XMCD signal is defined as difference of the spectra acquired with the two different polarizations, conventionally defined to get a negative signal at the L_3-edge.[49] Spin (μ_S) and orbital magnetic moments (μ_L), projected along the photon propagation axis, can be deduced in Bohr magneton units μ_B by a sum rule analysis,[68,69] through:

$$\mu_L(\theta) = -2n_\mathrm{h} \cdot \frac{q(\theta)}{r(\theta)} \cdot \mu_\mathrm{B}, \tag{2.10}$$

$$\mu_S^\mathrm{eff}(\theta) = \mu_S - 7\mu_\mathrm{T}(\theta) = -3n_\mathrm{h} \cdot \frac{[3p(\theta) - 2q(\theta)]}{r(\theta)} \cdot \mu_\mathrm{B}. \tag{2.11}$$

Thereby, n_h represents the number of holes in the $3d$-based states. $q(p)$ and r denote angle-dependent (θ with respect to the surface normal) integrals of the XMCD signal across the $L_{3,2}(L_3-$edge) and the isotropic absorption intensity. The latter can be obtained by measuring the absorption spectrum with linearly-polarized along all cartesian axes defined by the photon propagation axis. In practice, this is not possible and r has to be approximated or derived from geometric considerations.[70] It has to be noted that only an effective spin magnetic moment can be obtained due to the intra-atomic magnetic dipole moment μ_T, reflecting the anisotropy in the charge distribution the spin is coupled to.[71]

2.3 Low-Energy Electron Diffraction

Low-energy electron diffraction (LEED) is based on the wavelike behavior of electrons in the energy range of 50-500 eV, which have a wavelength λ that is in line with inter-atomic distances. The mean free path of electrons in this energy window is in the 5-10 Å range. This makes the diffraction pattern observed for low-energy electrons being backscattered by a crystalline specimen very surface-sensitive. In practice, a millimeter-sized electron beam, tunable in energy, is directed onto the sample, and the elastically scattered electrons are displayed on a phosphorescent screen. All backscattered electrons pass a system of biased grids, used to filter out inelastically scattered electrons, prior to the acceleration of the elastically scattered electrons onto the phosphor screen.[72,73] Within a simple geometric description of LEED, the basis of a surface is reduced to a lattice point. The basis vectors $\vec{a}_1$, $\vec{a}_2$ can be transformed into reciprocal basis vectors $\vec{g}_1$, $\vec{g}_2$ through:

$$\vec{a}_\mathrm{i} \cdot \vec{g}_\mathrm{j} = 2\pi \cdot \delta_\mathrm{i,j} \ (\mathrm{i,j} \ = \ 1,2). \tag{2.12}$$

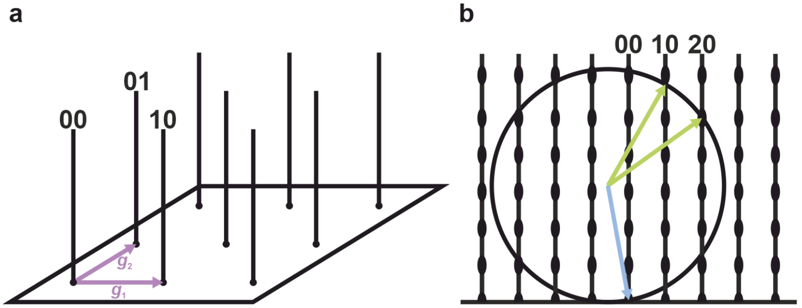

Figure 2.4: **(a)** The Fourier transform of an ideal two-dimensional surface lattice is obtained by LEED, where the unrestricted third Laue condition undergoes transformation into lattice rods. **(b)** Ewald construction for LEED as described in the main text. Replicated with adaptions from [72].

These lattice points are the scattering centers and the elastic processes are described by a scattering vector Δk, defined as difference of the wave vectors of diffracted k' and incident k beam. The conditions for constructive interference are described by the two-dimensional Laue equations. These equations define the relationship between Δk and the surface periodicity as:

$$\vec{a}_1 \cdot \Delta\vec{k} = 2\pi \cdot \mathrm{m}, \tag{2.13}$$

$$\vec{a}_2 \cdot \Delta\vec{k} = 2\pi \cdot \mathrm{l}. \tag{2.14}$$

m and l are integers and, thus, this implies that $\Delta\vec{k}$ corresponds to a reciprocal lattice vector $\vec{G}$. The diffraction pattern observed in LEED is the Fourier transform of the surface lattice. For all idealized two-dimensional surfaces any orthogonal component of Δk is allowed, as long as its parallel component is in accordance with the two-dimensional Laue conditions. This is depicted in figure 2.4a, where the lattice rods, representing the unconstrained third Laue condition orthogonal to the surface, are indicated. However, even low-energy electrons have a finite penetration depth and, therefore, the third Laue condition has to be taken into consideration, too. As a consequence, a diffraction spot intensity modulation along the lattice rods emerges. This is included in figure 2.4b, which depicts the Ewald sphere characteristic for elastic LEED processes where the parallel components of $\Delta\vec{k}$ are multiples of $\vec{g}_1$. The incident beam direction (light blue) points towards the reciprocal lattice origin, and, the Ewald sphere, with a radius of $2\pi\lambda^{-1}$, is constructed. Elastic scattering and $\Delta\vec{k} = \vec{G}$ require the scattered beam directions (light green) to coincide with the intersection points of the lattice rods with the Ewald sphere. Due to the intensity modulation along the lattice rods the (10) spot intensity would be lower than the (20) spot intensity for the case shown in figure 2.4b. The incident beam energy defining $\vec{k}$, therefore, allows control over the radius of the Ewald sphere. Consequently, diffraction spots can be moved towards or away from the (00) spot. The small penetration depth of the low-energy electrons is of particular interest for (metal-)organic layers on surfaces. A superposition of all rotational domains and the substrate features allows valuable insights for characterization of unit cell parameters and orientations. There are also dynamic scattering theories, which allow for more sophisticated structural insights atop the simple geometric description of LEED, only based on lattice points and diffraction spot positions unaltered by multiple scattering.[54]

2.4 Scanning Tunneling Microscopy and Spectroscopy

In scanning tunneling microscopy (STM), a voltage V is applied between a conductive sample and a conductive as well as atomically sharp tip, positioned a few Å atop the specimen, resulting in a current I that is utilized for surface imaging.[74] Binnig and Rohrer have invented this real space imaging microscopy based on electron tunneling in 1982,[75] recognized with the Nobel prize in physics 1986. In practice, the tip is scanned across the specimen, either at constant height or while maintaining a constant I through feedback electronics. In a simplified one-dimensional model of a tunneling junction, an electron with a energy E can pass a vacuum barrier of distance d with a height Φ exceeding its E. This classically forbidden tunneling process from one electrode to another occurs through an exponential decay of the electron wave function. I is then proportional to the absolute square of the amplitude of the wavefunction. It is constructed by combining the solutions of the Schrödinger equation for each part of the tunneling junction to match at the boundaries between them. The probability of an electron tunneling through the vacuum barrier is then described by the transmission coefficient T

$$T \propto \exp\left(-2d \cdot \sqrt{\frac{2m \cdot \Phi}{\hbar^2}}\right). \tag{2.15}$$

Therein, the electron mass and reduced Planck constant are denoted as m_e and $\hbar$. From this simplified model, the exponential decay of I with increasing d between tip and sample is already evident. Tunneling occurs within a bias window between the tip and the sample, which is defined as eV (e: elementary charge), describing the difference between the E_F of sample and tip. In the model of Bardeen,[76] I is related to all possible elastic transitions occurring in the bias window from the occupied states of the negative to unoccupied states of the positive electrode. The incremental contribution of each energy-conserving transition to I can be related to the combined density of states (DOS) of tip and sample, leading to:

$$dI \propto \mathrm{DOS}_\mathrm{sample}(E) \cdot \mathrm{DOS}_\mathrm{tip}(E) \cdot dE. \tag{2.16}$$

Considering Φ in equation 2.15 can be calculated using the work functions of sample (Φ_sample) and tip (Φ_sample) as

$$\Phi = \frac{\Phi_\mathrm{sample} + \Phi_\mathrm{tip}}{2} + \frac{eV}{2} - E, \tag{2.17}$$

results in the highest probability of tunneling for the states at E_F of the negative electrode, indicated by the arrows in the sketch of a tunnel junction displayed in figure 2.5.[74] To neglect the energy-dependence of I, Tersoff and Hamann have developed a model for small V.[77] Thereby, the tip is approximated as an s-wave function, resulting in a tunneling current sensitive to the local DOS of the sample at the Fermi level and at the center of the tip, explaining the atomic resolution often observed in STM.[74] This is particularly interesting for local scanning tunneling spectroscopy (STS), where the differential conductance can be related to the DOS of the sample at an energy defined as eV relative to the Fermi level as:

$$\frac{dI}{dV} \propto \mathrm{DOS}_{\mathrm{sample}}(eV). \tag{2.18}$$

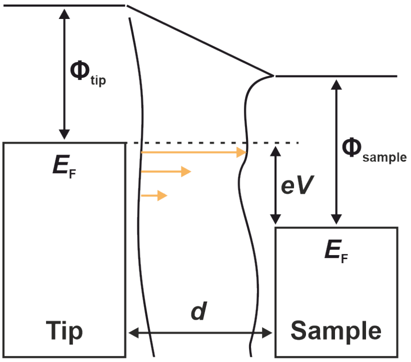

Figure 2.5: Schematic of a tunneling junction where electrons tunnel from tip to sample. Tunneling occurs within a bias window and the transitions from electrons at E_{F} of the negative electrode (tip) have the highest probability and are further scaled by the combined DOS of tip and sample. Replicated with adaptions from [74].

3 Experimental Details

The place of work during my Ph.D. has been at the NanoESCA beamline of the Elettra synchrotron in Trieste, Italy, operated by the PGI-6 of the Jülich Research Center. The preparation chamber attached to the main setup has been used to conduct all preliminary studies, prior to conducting VB spectroscopy measurements and complementing the obtained results by additional characterization methods. This chapter introduces the experimental details for all experiments realized.

3.1 Sample Preparation

All surfaces of the single crystals (MaTecK), used as supporting substrates for the molecular layers described in this work, have been cleaned by repeated cycles of Ar^+ or Ne^+ sputtering (2 keV or 1.5 keV) and subsequent annealing to 773 K. The presented results have been obtained at different measurement chambers, that have all been operated under UHV conditions, with preparation chambers attached to the main setups. In all cases, the base pressures have at least been in the 10^{-10} mbar range.

The calibration of the molecular coverages varied at the different preparation setups. If not mentioned otherwise, monolayer (ML) coverages have been realized. They will be also denoted as "saturated" layer throughout this thesis. Calibration for NiTBrPP and NiTPP overlayers have been performed based on LEED at the NanoESCA and X-Treme beamlines. Diffraction patterns can be observed, when the films are deposited on the Au(111) surface. Sharp diffraction spots arise upon subsequent increase of the amount of deposited molecules and are further blurred after the ML is reached. The obtained rates have been assumed to be equal for Ag(111) and Cu(111). At the ALOISA beamline a quartz microbalance has been used. Large-scale STM images have been used to judge the coverages of NiTBrPP in the experiments, designed for the local characterization. In contrast, TCNB molecules have not formed second layers on any of the surfaces they have been deposited onto. The saturation conditions have consequently been defined from the STM images and TCNB features in the spectra, which are not increasing further after reaching the ML coverage. All details on the used molecules and evaporations conditions are summarized in table 3.1.

Table 3.1: Overview of the details about the molecules used in this work together with the temperatures T at which they have been evaporated.

Molecule	**Supplier**	**Purity [%]**	**T [K]**
NiTBrPP	Frontier Scientific	97	660
NiTPP	Sigma-Aldrich	≥ 95	570
TCNB	Sigma-Aldrich	97	373

Evaporation of Ni onto pristine TCNB layers has been realized using electron beam heating while the metal evaporation flux (5-10 nA range) has been varied in the different preparation chambers attached to the measurement setups, described in chapter 3.2. As the sample to evaporator distance has been different for the respective preparation chambers, the fluxes varied. They will be given in absolute deposition times t for each dataset, in order to allow a comprehensible understanding.

3.2 Experimental Setups and Data Treatment

3.2.1 NanoESCA Beamline

The valence band (VB) data presented in this work have been acquired at the NanoESCA beamline of the Elettra synchrotron in Trieste, Italy. The photoelectron emission microscope installed there (k-PEEM, see [78]) has been designed for collecting the entire photoelectron hemisphere above the sample surface with k- and E-resolution. Varying the kinetic energy (E_{kin}) of the emitted photoelectrons allows collecting a data stack constituted by constant binding energy photoelectron $k_{||}$-distribution maps (momentum maps). The VB spectra presented in this work represent the integrated intensity of each constant E_{B} momentum map. Band maps have been obtained by vertically cutting through the data stacks, along defined paths in k-space. The sample has been cooled down to 90 K before data acquisition, which has been performed while continuously rastering the sample by the motorized sample positioning system to avoid damage and desorption by the synchrotron beam. At this setup the beam angle of incidence has been 25° with respect to the surface plane. The E_{B} calibration has been performed based on fitting of the E_{F}. For all data collected at $h\nu = 30$ eV the total energy resolution and k-resolution have been 100 meV and $|0.05|$ Å^{-1}.

3.2.2 ALOISA Beamline

The NEXAFS and XPS spectra presented in this work have been acquired at the ALOISA beamline of the Elettra synchrotron in Trieste, Italy.[79] A detailed description of the normalization and energy calibration protocol for the NEXAFS spectra collected across the C and N K-edge is described elsewhere.[66] A background has been subtracted from the Ni L_3-edge spectra and the energy calibration has been performed by measuring core levels characteristic of the substrate used to stabilize the (metal-)organic layers of interest. All NEXAFS spectra have been collected in the partial electron yield mode by a channeltron equipped with a repelling grid polarized at a negative bias (-250 V , -370 V and -820 V for the C and N K-edge as well as the Ni L_3-edge, respectively). The sample has been kept at an 84° grazing photon incidence with respect to the surface normal and the manipulator has been mounted coaxially to the photon beam. This allows us to change the surface orientation with respect to the linearly-polarized light from Transverse Electric (s-polarization) to Transverse Magnetic (close to p-polarization) by rotation around the photon beam axis. XPS measurements have been conducted in a normal emission geometry using p-polarized light at several photon energies with the light impinging on the sample at a grazing incidence (86° with respect to surface normal). In order to get an appreciable signal, and to account for the beamline resolution at the various core levels of interest, the pass energy of the

Table 3.2: Overview of the energy resolutions at the different photon energies used for XPS experiments.

$h\nu$ [eV]	Resolution [meV]
515	160
980	420
1050	450

analyzer has been varied for different photon energies. This results in the different total energy resolutions summarized in table 3.2. For XPS binding energy (E_B) calibration we have used selected core level spectra of the supporting substrates for the (metal-)organic nanostructures of interest. The calibration procedure has been based on the results reported from a single group on all relevant metals to exclude relative errors.

Table 3.3: Substrate photoelectron lines used for the E_B calibration of the XPS datasets obtained for different supporting substrates based on [80, 81].

Photoelectron line	E_B [eV]
Au $4f_{7/2}$	84.0
Ag $3d_{5/2}$	368.3
Cu $3p_{3/2}$	75.1

3.2.3 X-Treme Beamline

XMCD measurements have been conducted at the X-Treme beamline of the Swiss Light Source at the Paul Scherrer Institute in Villigen, Switzerland, with the sample cooled down to $\approx$ 3 K.[82] A permanent magnetic field of maximum $B = 6.8$ T along the photon incidence axis has been used in order to reach conditions close to saturation. Different incidence angles have been realized by rotating the sample. The photon energy calibration for the absorption spectra recorded across the Ni $L_{3,2}$-edge has been performed based on a comparative analysis with the data obtained using linearly-polarized light at the ALOISA beamline. Data acquisition has been performed in the total electron yield mode with the drain current measured at the sample and an energy resolution of around 100 meV available. The normalization procedure is described elsewhere.[70,83,84] For obtaining magnetization curves characteristic of the respective molecular layers, the magnetic field B has been varied from 6.8 T to -6.8 T and vice versa while collecting the signal at the pre-edge and on the maximum of dichroic signal using photons of both helicities. In order to account for drifting of the baseline the relative ratio of the two points at every B value has been considered for each helicity. Then the XMCD signal has been calculated and normalized. As no remanent magnetization has been observed the two different scans with opposite magnetic field variation have been averaged.

3.2.4 Low-Energy Electron Diffraction Setups

SPECS LEED setups have been used whenever available in the preparation chambers attached to the main setups. When examining the relative changes characteristic of the transformations within (metal-)organic layers, the sample-to-electron source distance and the incident beam energy have been kept constant. This ensures that changes in LEED patterns are only attributed to structural changes. The LEEDpat4[a] software has been used for simulating LEED patterns.

3.2.5 Scanning Tunneling Microscopy Setups

The low-temperature (LT-)STM/STS data presented in chapter 4 have been obtained at the CNR-IOM - Istituto Officina dei Materiali, National Research Council of Italy in Trieste. The sample has been cooled down to 77 K before characterization in the LT-STM (Scienta Omicron GmbH). The bias voltage (V) is given as sample bias with respect to the electrochemically etched tungsten tip. For spectroscopy measurements lock-in detection of I has been used.

The LT-STM/STS experiments presented in chapter 5 have been conducted using a commercial LT-STM (Scienta Omicron GmbH) at a temperature of $\approx$ 9 K. The bias voltage (V) is given as sample bias with respect to the electrochemically etched tungsten tip. A small amount of CO has been dosed onto the cold surface ($T < 10$ K) for tip functionalization. dI/dV spectroscopy and bond-resolved STM (BRSTM, see [85]) have been performed using lock-in detection of I. Based on the variations from different line profiles used for structure determination, as well as comparison with literature on the TCNB/Au(111) interface,[86] we estimate an error of 7% and 5° for the obtained lattice vectors and angles presented in chapter 5. The Ni-TCNB complex and Ni-TCNB MOF (see later) have been the predominant phases present for total Ni deposition times of 30 s and 50 s.

---

[a] `https://www.fhi.mpg.de/958975/LEEDpat4`; Last access: Oct, 2023.

4 Covalent Nickel Tetraphenylporphyrin Networks on Coinage Metals

This chapter is partially based on two first author works. The first one is published as: **Conservation of Nickel Ion Single-Active Site Character in a Bottom-Up Constructed π-Conjugated Molecular Network** by Baranowski, D.; Cojocariu, I.; Sala, A.; Africh, C.; Comelli, G.; Schio, L.; Tormen, M.; Floreano, L.; Feyer, V.; Schneider, C. M. in *Angew. Chem. Int. Ed.* **2022**, *61*, e202210326.[39] I have performed the valence band spectroscopy measurements together with Cojocariu, I. and Feyer, V.. XPS/NEXAFS data have been collected together with Cojocariu, I. and Feyer, V. under guidance of Schio, L.; Tormen, M. and Floreano, L.. I have analyzed the data and received feedback from all people involved in the valence band spectroscopy and XPS/NEXAFS experiments. STM/STS characterization and analysis has been performed by Sala, A.; Africh, C. and Comelli, G.. I have written the first draft, and all co-authors have contributed to improvements before submission. The project has continuously been supervised by Feyer, V. and Schneider, C. M..

The second one is published as: **Tuning Transition Metal-Containing Molecular Magnets by On-Surface Polymerization** by Baranowski, D.; Cojocariu, I.; Schio, L.; Gutiérrez Bolaños, C.; Floreano, L.; Dreiser, J.; Carlotto, S.; Casarin, M.; Feyer, V., Schneider, C. M. in *Adv. Mater. Interfaces* **2024**, 2400123.[40] I have performed the XPS/NEXAFS measurements together with Cojocariu, I. and Feyer, V. under guidance of Schio, L.; Gutiérrez Bolaños C. and Floreano L.. XMCD data have been collected together with Cojocariu, I. and Feyer, V. under guidance of Dreiser, J.. I have analyzed the data and received feedback from all people involved the XPS/NEXAFS and XMCD experiments. The calculations have been performed by Carlotto, S. and Casarin, M.. I have written the first draft, and all co-authors have contributed to improvements before submission. The project has continuously been supervised by Feyer, V. and Schneider, C. M..

This chapter is about the properties of functional nickel centers stabilized within the moiety of NiTPP units that have been covalently linked by on-surface polymerization. The Ullmann coupling approach based on NiTBrPP has been realized on surfaces characterized by different reactivity.[11] The properties of the obtained covalent molecular networks have turned out to be tunable when increasing the charge transfer from the supporting substrate. Even though the obtained NiTPP networks are not ordered, amorphous and characterized by defects, the molecular backbone is π-conjugated, as expressed by the appearance of a dispersive parabolic band. At the same time, the Ni units within the porphyrin center retain their single-active site character, allowing for activating molecular magnetism by charge transfer at the interface on Cu(111).

4.1 On-Surface Ullmann Coupling

The covalent intermolecular C-C coupling, based on activation of halogen-bound carbon as introduced for aryl halides by Ullmann in solution,[87,88] has been transferred to the field of on-surface synthesis.[89–92] In a pioneering work by Grill et al., the structural diversity of porphyrins has been utilized to confirm carbon-halogen bonds as predefined connection points between monomers.[11] Since then, surface-assisted Ullmann coupling has emerged as the primary method for obtaining carbon-based polymers, preferentially carried out on coinage metals under UHV conditions. The Ullmann reaction, catalyzed by the supporting surface, involves homolytic carbon-halogen bond cleavage in the molecular precursor, followed by covalent linking of surface-stabilized radicals.[93] For the same facets of coinage metal surfaces, the necessary dehalogenation temperature increases from Cu to Ag and then to Au.[94–97] Upon polymerization structural defects appear and, in particular for porphyrins, cyclodehydrogenation side reactions occur.[18] A structural model of the NiTBrPP precursor used for Ullmann coupling in this work is presented in figure 4.1. The C-Br bonds, which are highlighted by the purple dashed line, can be cleaved by catalytically active surfaces and are predefined points for the creation of new intermolecular C-C bonds. Porphyrins with phenyl substituents are flexible upon stabilization on surfaces, which can result in tilted and twisted phenyl configurations as indicated by the blue arrows in figure 4.1.[98,99] Intramolecular C-C coupling, resulting from cyclodehydrogenation involving flexible phenyl substituents, is further relevant when annealing porphyrin layers to elevated temperatures necessary for Ullmann polymerization.[18] An example of a possible C-C linking between the porphyrin macrocycle and a phenyl group upon cyclodehydrogenation is indicated by the orange arrow in figure 4.1. We have used different polymerization temperatures in this work, where Br species stabilized on the supporting surface are removed when it is possible without damaging the molecular NiTPP-based networks (Au(111) and Ag(111)).[97] On Cu(111), Ullmann polymerization has been realized at 473 K, excluding decomposition of the covalent nanomesh and allowing for cyclodehydrogenation reactions.[100,101] On Au(111), 673 K has been chosen as polymerization temperature with efficient cyclodehydrogenation side reactions,[102,103] while on Ag(111) 573 K has been necessary.[104,105]

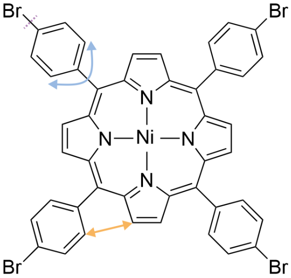

Figure 4.1: Sketch of the NiTBrPP precursor used for Ullmann coupling on various coinage metals. Reproduced from [40].

4.2 Covalent Nickel Tetraphenylporphyrin Network on Au(111)

The first step towards the preparation of a covalent NiTPP nanomesh has been the evaporation of a saturated NiTBrPP layer on the Au(111) at room temperature. By using the *k*-PEEM, the characteristic photoelectron distribution pattern has been recorded. The band map obtained along $\overline{\mathrm{M}}$-$\overline{\Gamma}$-$\overline{\mathrm{M}}$ of the supporting surface, up to a binding energy of 2.0 eV, is displayed in figure 4.2. The Au(111) surface Brillouin zone is indicated in the top left. There are two features evident in addition to the *sp*-bands of the substrate. The black stars in figure 4.2 highlight them. The features appear the same along equivalent directions and arise at binding energies around 1.1 eV and 1.4 eV, respectively. We attribute these peaks to the HOMO and HOMO-1 of anchored NiTBrPP. The molecular signals arising in the valence band spectrum are localized in *k*-space, which is an evidence for a preferential on-surface orientation of the molecular layer.[58] There is no signal from molecular levels close to the Fermi level, which indicates a weak molecule-substrate interaction.[106,107] This is a highly desirable property of a prototype system, whose intrinsic properties upon polymerization can then be further elucidated, without being drastically influenced by the supporting substrate. MOs unoccupied in the gas phase would be partially filled, if there might be a strong charge transfer at the interface.

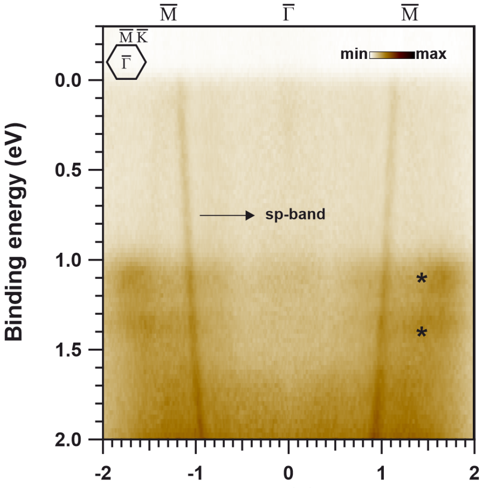

Figure 4.2: Band map obtained for the pristine NiTBrPP layer on Au(111) along $\overline{\mathrm{M}}$-$\overline{\Gamma}$-$\overline{\mathrm{M}}$ of the supporting surface. Adapted from [39].

Intact NiTBrPP units have then been annealed stepwise to induce C-Br bond cleavage, and realize Ullmann coupling of the activated precursor molecules. A suitable temperature range for this polymerization reaction has been identified based on XPS. Br 3*d* photoelectron spectra obtained for the parent NiTBrPP/Au(111) layer together with those after heating to 473 K and 673 K, are summarized in figure 4.3. The as-deposited molecular layer exhibits a doublet with the Br $3d_{5/2}$ main line at a binding energy of around 69.9 eV, which is characteristic for carbon-bound

Br species. The signal corresponding to the brominated porphyrin precursor is reduced upon annealing to 473 K. Thereby, an additional doublet arises at lower binding energies of around 67.8 eV. This can be attributed to Br species adsorbed on the Au(111) substrate after activation of the brominated porphyrin units.[18,108,109] Annealing to 673 K, finally, resulted in all Br species to desorb from the substrate. Direct annealing to this temperature has subsequently been chosen to produce a covalent porphyrin network starting from a saturated NiTBrPP layer on Au(111), making it worth mentioning the observed high thermal stability of the obtained NiTPP-based network.

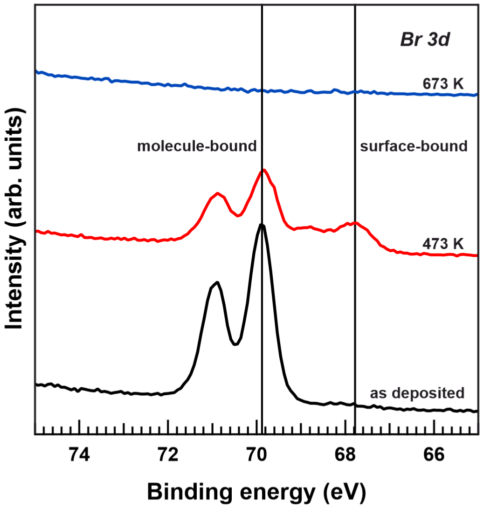

Figure 4.3: Evolution of the Br 3*d* core level spectra upon stepwise annealing of as-deposited NiTBrPP on Au(111). All spectra have been collected at $h\nu = 515$ eV (p-polarization) in normal emission. Reproduced from [39].

STM studies have been conducted to characterize the chemical changes in the adsorbed molecular film. The topographic images in figure 4.4a, cropped from large-scale images presented in figure 4.5, include a sketch of the molecular geometry. When it comes to pristine NiTBrPP on Au(111), the present contrast allows concluding that the porphyrin macrocycle is characterized by two symmetric bright lobes, oriented orthogonally to the surface normal.[110] The phenyl substituents of neighboring molecules, which are rotated off-plane with respect to the macrocycle, are identified to be aligned parallel with respect to each other, which, again, confirms the weak molecule-substrate interaction.[111] From the presented region of a covalent NiTPP-based nanomesh, created by annealing, it can be concluded that the phenyl substituents are flattened upon the formation of a π-extended macromolecule via intermolecular coupling.[18] Based on the corresponding large-scale topographic STM images presented in figure 4.5 it can be concluded that the covalently interconnected molecular units within the NiTPP-based network are no longer characterized by any sort of preferential on-surface orientation, in contrast to the pristine NiTBrPP layer on Au(111). For the covalent structure, moreover, randomly distributed defects with various shapes are evident, where phenyl groups failed to react with neighboring ones. The nanomesh is highly interconnected, since these imperfections almost exclusively appear when one of the four phenyl substituents remains unsaturated, which approximately applies to one out of ten molecules. While analyzing the monomeric units in the network, deviations from a perfect four-fold symmetry that make the porphyrin nanomesh amorphous become evident. The appearance of the molecular constituents allows us to conclude that these irregularities originate from cyclodeydrogenation side reactions, which additionally increase the degree of conjugation in the molecular network. Indeed, four tetraphenylporphyrin derivative products have been reported upon annealing pristine molecules on Au(111),[102,103] and these species are randomly incorporated into the covalent porphyrin network reported here, as confirmed by STM. The supporting Au(111) surface appears partially uncovered in comparison to the pristine NiTBrPP layer, which can be attributed to the desorption of some molecular precursor upon thermal activation, and in-plane shrinking of the molecular network. This is in perfect agreement with the corresponding XPS data, as further elaborated in the following. The partial dehydrogenation of the monomeric units restricts the growth direction when the covalent nanostructure is formed, rendering a random on-surface orientation of the porphyrin units within the NiTPP-based network. Consequently, defects appear when reaction partners are missing due to desorption.

STS has then been applied in order to locally characterize the differences between the molecular units, embedded in the covalent nanomesh, and their single-molecule counterparts. The dI/dV spectra of pristine NiTBrPP and the NiTPP-based network on Au(111) are compared in figure 4.4b. From the dI/dV texture characteristic of the NiTBrPP layer it is evident, that the brominated molecular precursor is characterized by a molecular gap. The HOMO and HOMO-1 positions found via valence band spectroscopy (figure 4.2) as well as the feature we attribute to the LUMO of NiTBrPP are indicated. In contrast, the spectrum of the final NiTPP network is no longer characterized by molecular levels of defined energy, but rather by a DOS distributed over the entire bias range. The debrominated and interconnected porphyrin units after thermal activation are chemically related to NiTPP and dehydrogenated NiTPP. However, the absence of a clear molecular signature in STS cannot be explained by the distinct dehydrogenation pathways, that occurred at this sample position. Indeed, the frontier states of various cyclized porphyrins shift in energy with respect to their initial values, but remain defined.[103] It appears that the changes observed for the STS of the covalent network are related to the formation of intermolecular bonds. dI/dV mapping across the occupied states of NiTPP-based network on Au(111) has allowed us to image the spatial profile after Ullmann coupling. An overview of the maps obtained at different voltages is given in figure 4.6. There is no more evidence of the occupied molecular state, that is the bright symmetric lobes localized at the macrocycle and used to identify the configuration of the pristine NiTBrPP layer in figure 4.4a. Instead, we notice that the spatially-defined states, mainly probed here in the bias range between -0.6 eV and -1.3 eV, are localized on the Ni centers. Both the shape and the energy range strongly resemble the energy position of the central ion d-states of NiTPP units, anchored to the weakly interacting oxygen-passivated Cu(100) surface.[45] It turns out that after polymerization no spatially-confined molecular states can be discriminated within the extended π-conjugated nanomesh and only the functional Ni centers display localized

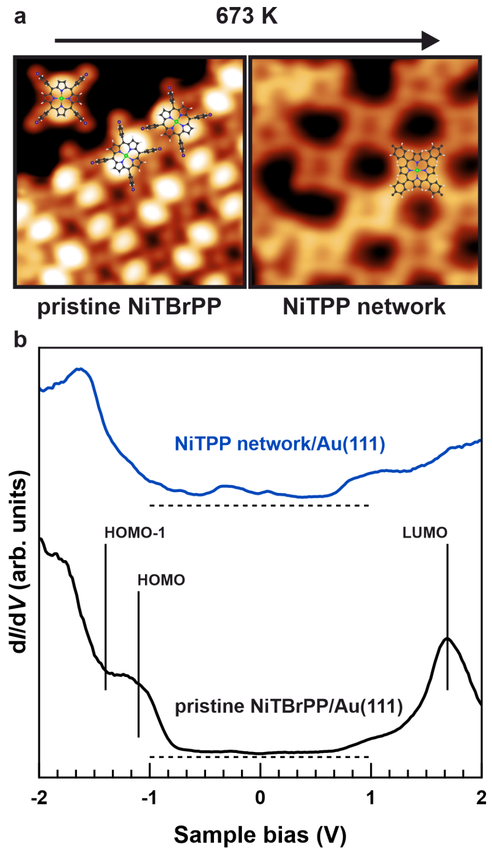

Figure 4.4: **(a)** STM image insets ($5.2 \cdot 5.2$ nm^2) of the as-deposited NiTBrPP layer ($V = -1.8$ V, $I = 0.5$ nA) and the NiTPP network ($V = -0.4$ V, $I = 0.5$ nA) on Au(111). **(b)** dI/dV spectra obtained for as-deposited NiTBrPP and NiTPP network on Au(111). The zero-levels are indicated by the dashed lines. The feedback has been opened at $V = -2.0$ V and $I = 0.5$ nA for all spectra. A voltage modulation of 20 mV at 1090 Hz has been used for collecting all spectra. Adapted from [39].

states.

Covalently linking NiTPP units leads to drastic changes in the valence band spectrum, as evident from figure 4.7. The discrete molecular levels, characteristic of NiTBrPP, disappear upon annealing the molecular precursor. Instead, a continuum of states, that is largely spread in energy, arises from few tenths of eV below the Fermi level. Broadening of molecular levels has been observed for oligomerized metal-free porphyrin units,[112] suggesting that the continuum observed here is related to the formation of an extended covalent nanostructure. A comparison of the band maps along $\overline{\mathrm{M}}$-$\overline{\Gamma}$-$\overline{\mathrm{M}}$ of the substrate, characteristic of clean Au(111) and after the creation of NiTPP-based covalent network, is presented in figure 4.8. The formation of a dispersive band of parabolic shape is evident. Strong evidence of this molecule-related states is absent, when using s-polarized instead of p-polarized light, indicating the occurrence of π-delocalization upon the

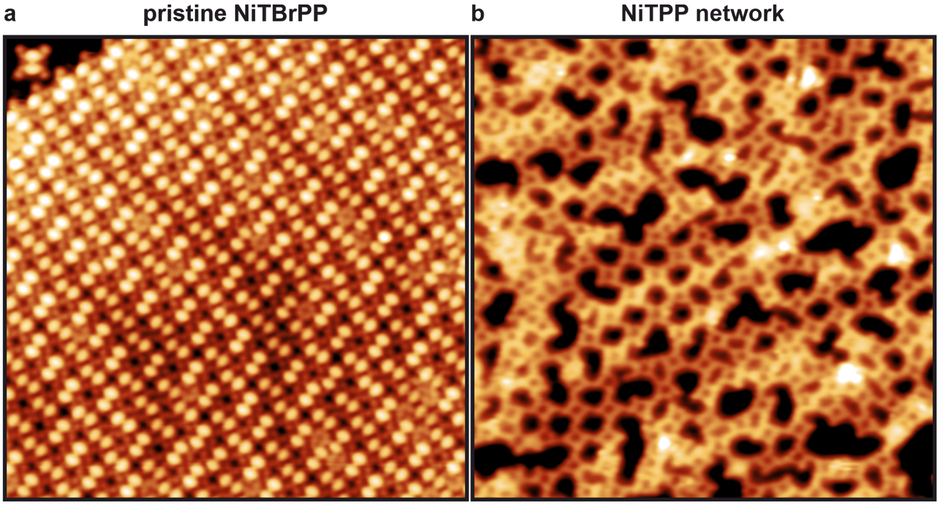

Figure 4.5: STM images ($21.7 \cdot 21.7$ nm^2) of **(a)** as-deposited NiTBrPP and **(b)** NiTPP network on Au(111). Adapted from [39].

polymerization of porphyrin units. All directions in k-space yield the same dispersion relation for the molecular network when using p-polarized light. The band structure is equally broadened along any direction and within the full energy range. This is demonstrated for $k_{||}$-maps acquired at a constant binding energy around 1.0 eV, which are presented in figure 4.9. The covalent porphyrin nanomesh produces a ring structure in k-space, which is closing for increasing binding energies. Similar findings have been observed for multiple rotational graphene domains.[113] We note that a broadening of the bands of graphene has further been observed when introducing nitrogen heteroatoms into graphene and simultaneously creating topological defects.[114] It is very peculiar, that the present graphene-related NiTPP-based polymer structure, though amorphous and defect-rich, is also characterized by a broad, and yet, continuous spectrum of states. This supports the picture of a uniform and efficient charge transport across the metal-like molecular layer, the stability of which is increased as a consequence of creating a π-extended aromatic system. This further allows concluding that the previously discussed dI/dV texture of NiTPP-based covalent network reflects the local DOS of the π-conjugated nanomesh. We also emphasize that, so far, dispersive electronic features connected to bottom-up constructed nanostructures have rarely been observed, limited to smaller monomeric units without any transition metal ions embedded.[115–121] There is no signature of a band based on Ni $3d$-states and the conditions for an experimental confirmation of these bands will be addressed in chapter 5.

This finding raises the question of how the individual porphyrin components are influenced by the creation of the porphyrin network. For this reason, NEXAFS measurements have been conducted for both the pristine NiTBrPP layer on Au(111) and after its conversion to the NiTPP-based network. The NEXAFS spectra recorded across the C K-edge are displayed in figure 4.10a. Specific transition into unoccupied π^*-symmetric MOs, mostly localized on either the macro-

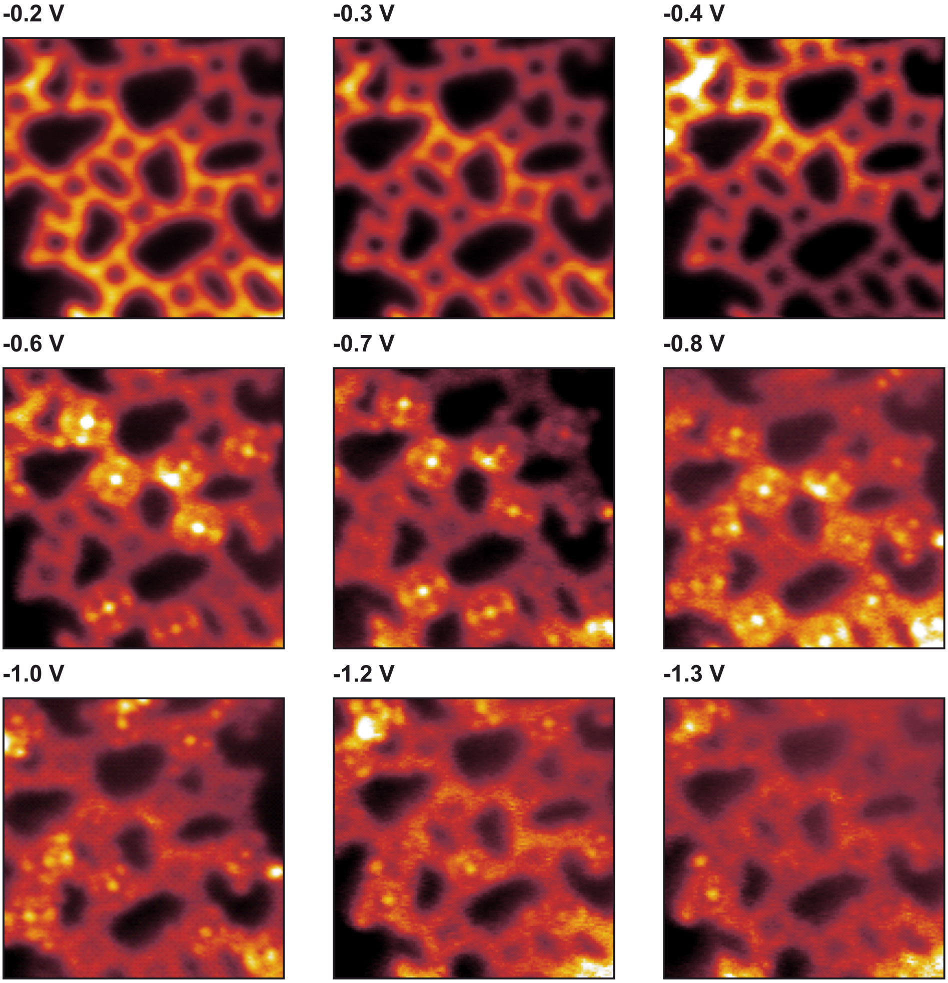

Figure 4.6: Constant-height dI/dV mapping series ($3.2 \cdot 3.2$ nm^2) across the occupied states of NiTPP-based covalent network. The respective bias is indicated as a caption at the top left. The feedback has been opened at $V = -1.0$ V and $I = 0.5$ nA for all maps. A voltage modulation of 20 mV at 1090 Hz has been used for collecting all maps. Reproduced from [39].

cycle or the phenyl substituents, can be distinguished from each other.[64] From the polarization dependence of the intensity, characteristic of NiTBrPP macrocycle (index m, 283.9 eV and 284.2 eV) and phenyl (index p, 285.2 eV) resonances, the molecular geometric configuration has been evaluated.[18,65,122–125] The photon energy values at which these resonance are observed define the references lines in figure 4.10a. For the pristine NiTBrPP layer on Au(111), the aforementioned characteristic π^*-macrocycle resonances are almost absent for s-polarized light, which confirms a nearly flat absorption of the macrocycle on the surface. On the contrary, the π^*-phenyl resonances are evident for both light polarizations. These findings directly correspond to the STM results, where a significant tilt of the phenyl groups with respect to the macrocycle plane has

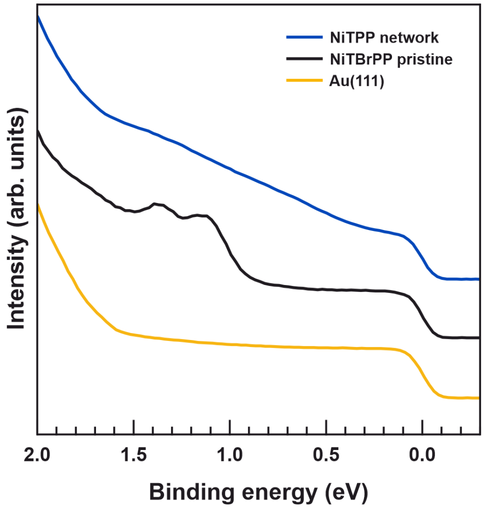

Figure 4.7: Valence band spectra of clean Au(111), as-deposited NiTBrPP and NiTPP-based network on Au(111). The spectra have been recorded at $h\nu = 30$ eV (p-polarization) and normalized to the signal at the Fermi edge. Reproduced from [39].

been observed. For the NEXAFS spectra obtained across the C K-edge after the formation of the NiTPP-based network all π^*-resonances nearly vanish in s-polarization. This leads us to conclude that all phenyl rings are forced into a flat configuration, as already observed by STM. At the same time, the shape and relative intensity of the π^*-resonances observed in p-polarization significantly differ from those measured for the pristine NiTBrPP layer on Au(111). Instead of sharp molecular absorption peaks for NiTBrPP, a more continuous absorption signal is observed for the extended covalent NiTPP-based network. Both for porphyrin cyclodehydrogenation and oligomerization of porphyrin units similar findings have been obtained.[104,112,126] The newly formed C-C bonds make a straightforward identification of effects related to the occurrence of π-delocalization hard to disentangle. The C 1s photoelectron spectra of the parent NiTBrPP layer and NiTPP-based network on Au(111) are further compared in figure 4.10b. The multicomponent signal characteristic of NiTBrPP is transformed upon Ullmann coupling of the activated precursor molecules. In particular, the C-Br contribution at the highest binding energy (indicated by the arrow at ≈ 285.2 eV) vanishes and the main carbon peak displays an overall shift to lower binding energies (≈ 0.2 eV), together with a decrease of the energy spread among different carbon atoms.[127] This fully supports the picture of a more uniform carbon environment within an extended covalent nanostructure, characterized by π-conjugation.

The consequences of intermolecular coupling, particularly with regard to more pronounced π-delocalization effects, become more evident from the NEXAFS spectra obtained across the N K-edge. A comparison of the spectra obtained for pristine NiTBrPP and NiTPP-based network on Au(111) is presented in figure 4.11a. The higher energy π^*-resonances, related to pure macrocycle MOs, are the ones mostly affected by the polymerization reaction.[122,123] These resonances display

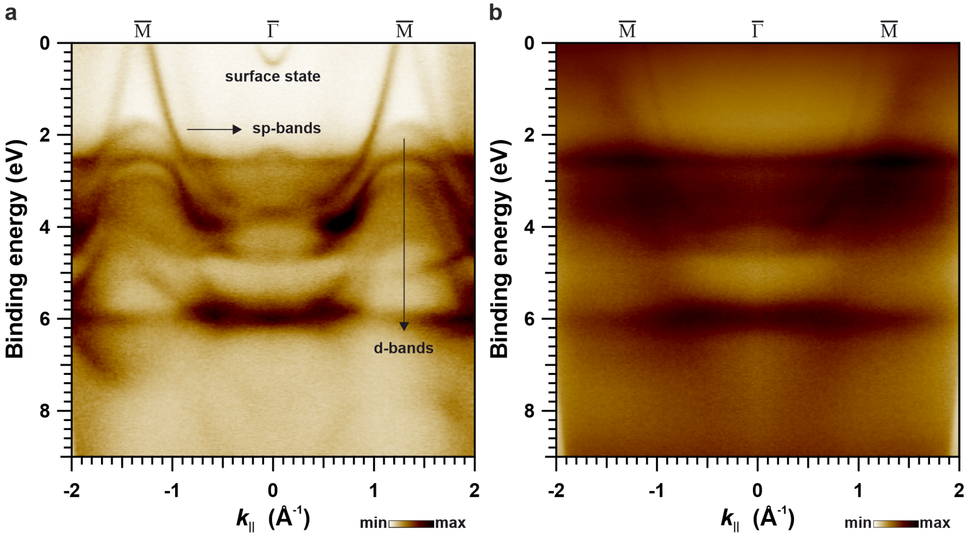

Figure 4.8: Photoelectron $k_{||}$-distribution along $\overline{\mathrm{M}}$-$\overline{\Gamma}$-$\overline{\mathrm{M}}$ of the substrate recorded at $h\nu = 30$ eV (p-polarization) for **(a)** clean Au(111) and **(b)** NiTPP-based network on Au(111). Adapted from [39].

an overall broadening upon the creation of the covalent NiTPP-based network, which suggests an increase of the orbital delocalization (faster decay of the excited state) due to the formation of a π-extended structure. As such, we relate this effect as characteristic of the changes within the molecular backbone upon polymerization, as cyclodehydrogenation of porphyrin molecules is not accompanied by a significant broadening of these π^*-resonances.[126] Information on the Ni centers stabilized within the porphyrin N-moiety is of major interest in order to evaluate to what extent their main single-molecule functionalities are retained when embedded in more stable π-delocalized covalent nanomeshes. The low energy resonances apparent in the N K-edge spectra at $\approx$ 399 eV, which are shown in figure 4.11a, result from the mixing of Ni $3d$ with ligand $2p$ levels as emphasized by the chosen index *Ni*. They further allow more sophisticated insights into the Ni centers stabilized within the polymerized porphyrin structure. A σ^*-resonance is associated with the N-coordination (ligand $2p_{\mathrm{x,y}}$ and Ni $3d_{\mathrm{x}^2-\mathrm{y}^2}$), while the Ni $3d_{\mathrm{xz,yz}}$ to ligand $2p_{\mathrm{z}}$ backbonding corresponds to the first π^*-resonance.[107,122,123] Although these features are similar in energy, the already discussed flat macrocycle configuration enables us to easily recognize them in the NEXAFS spectra acquired with different polarizations. The σ^*-resonance, well-evident in the spectrum recorded using s-polarized light, is known to only show up in the case of a weak molecule-substrate interaction.[107] Indeed, no drastic change in the energy position of this σ^*-resonance is observed upon creation of the covalent porphyrin macromolecule, while the π^*-resonance corresponding to the Ni-to-ligand-backbonding is only slightly shifted by ≈ 0.2 eV towards lower photon energies. This indicates a very similar coordination environment of the Ni centers embedded in the covalent nanomesh with respect to the NiTBrPP precursor. This is supported by the N $1s$ photoelectron spectra before and after polymerization, which are displayed in figure 4.11b. Covalent linking of activated NiTBrPP units does not alter either the spectral

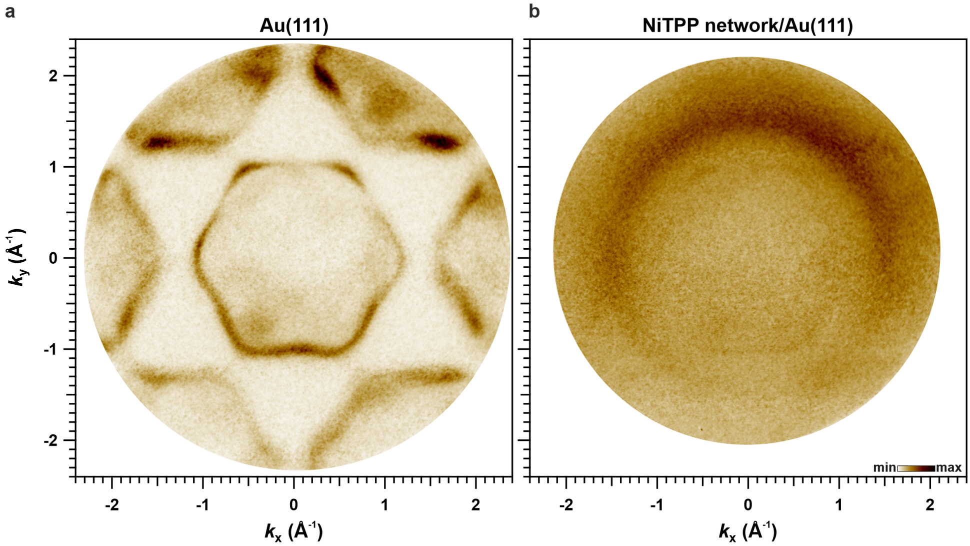

Figure 4.9: Constant binding energy (= 1.0 eV) photoelectron $k_{||}$-distribution maps recorded at $h\nu$ = 30 eV (p-polarization) for **(a)** clean Au(111) and **(b)** NiTPP-based network on Au(111). Adapted from [39].

shape or linewidth. The overall reduced intensity can be attributed to the partial desorption of molecular precursor units. Yet, the signals are shifted by $\approx$ 0.2 eV towards higher binding energies (opposite to the case of the C 1s signal) after the formation of the covalent NiTPP-based nanomesh. The flattening of all molecular constituents (i.e. the pyrrolic macrocycle and the phenyl groups) is expected to influence the distance of the functional porphyrin center to the supporting surface, which can explain these shifts as a result of changed core hole screening. This has been reported for various on-surface reactions.[127,128]

The formation of a polymeric π-conjugated nanostructure, thus, involves also the Ni-coordinating porphyrin N-moiety without major impacts on the coordination characteristics. This is strongly confirmed by the corresponding NEXAFS spectra recorded across the Ni L_3-edge, which are displayed in figure 4.12a. Upon the formation of the NiTPP-based network, the Ni main absorption line is slightly shifted towards higher photon energies, which also reflects the increased Ni-to-N-backbonding. Since no further changes in both the spectral shape and satellite structure characteristic of the Ni(II) low-spin state are observed, we can assume the Ni center single-active site character to be preserved.[45,129] The Ni ion centers embedded in the polymeric molecular backbone are barely influenced by the extended π-bonding within the molecular backbone as desired for a multifunctional device with active centers, whose performance benefits from the larger stability of the polymerized backbone. It should be emphasized that the imperfections in the covalent nanomesh reported here do not lead to any visible broadening of the Ni-related states indicating a well-defined functionality that is uniform across the interface.

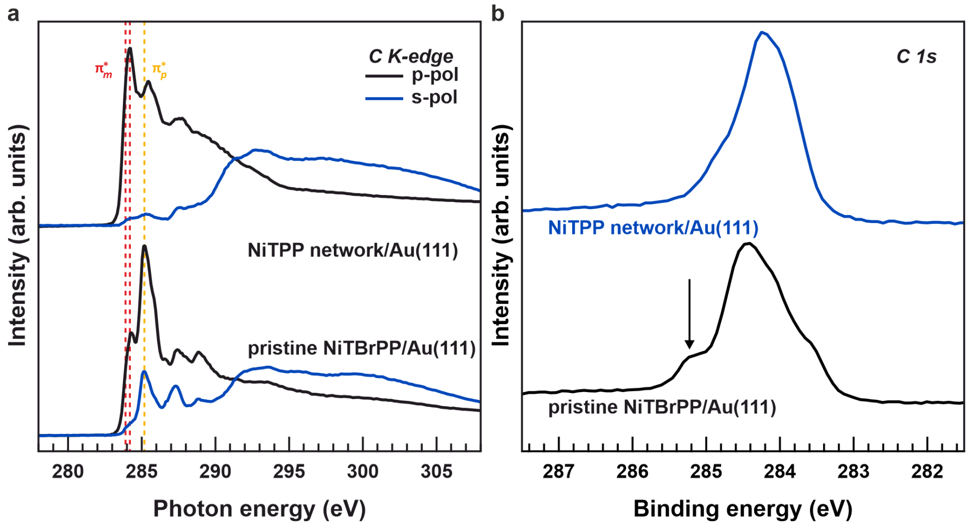

Figure 4.10: (a) NEXAFS spectra obtained across the C K-edge and **(b)** C 1s core level spectra recorded at $h\nu = 515$ eV (p-polarization) in normal emission for pristine NiTBrPP and NiTPP-based network on Au(111). Adapted from [39].

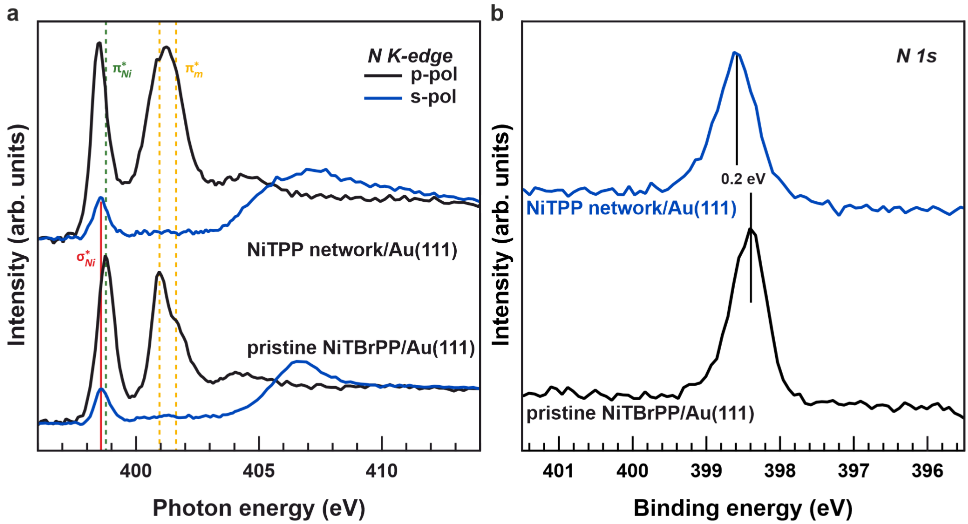

Figure 4.11: (a) NEXAFS spectra obtained across the N K-edge and **(b)** N 1s core level spectra recorded at $h\nu = 515$ eV (p-polarization) in normal emission for pristine NiTBrPP and NiTPP-based network on Au(111). Adapted from [39].

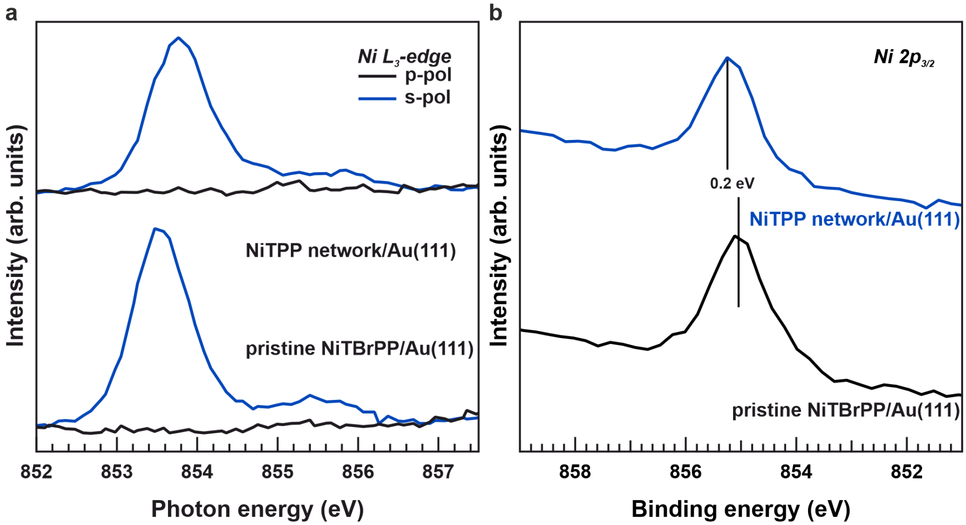

Figure 4.12: (a) NEXAFS spectra obtained across the Ni L_3-edge and **(b)** Ni $2p_{3/2}$ core level spectra recorded at $h\nu = 1050$ eV (p-polarization) in normal emission for pristine NiTBrPP and NiTPP-based network on Au(111). Adapted from [39].

4.3 Covalent Nickel Tetraphenylporphyrin Network on Ag(111)

We have also explored the more reactive Ag(111) substrate as a catalyst to create a covalent NiTPP-based network. We have performed the polymerization reaction by direct annealing to 573 K, starting from a saturated layer of NiTBrPP on Ag(111). The band maps along $\overline{\mathrm{M}}$-$\overline{\Gamma}$-$\overline{\mathrm{M}}$ of the substrate characteristic of both bare Ag(111) and NiTPP network on Ag(111) are compared in figure 4.13. The parabola of states also appears to be exhibited by the covalent nanomesh created on Ag(111). The parabola obtained on the Ag(111) substrate is also highlighted in blue and compared (green) to the bottom part of the parabola obtained on Au(111) in figure 4.13b. It can be concluded that the more pronounced charge transfer at the Ag(111) interface results in a shift of the parabola of ≈ 0.6 eV towards higher binding energies while the shape remains equal. Similar findings have been obtained when creating graphene on more reactive surfaces.[113]

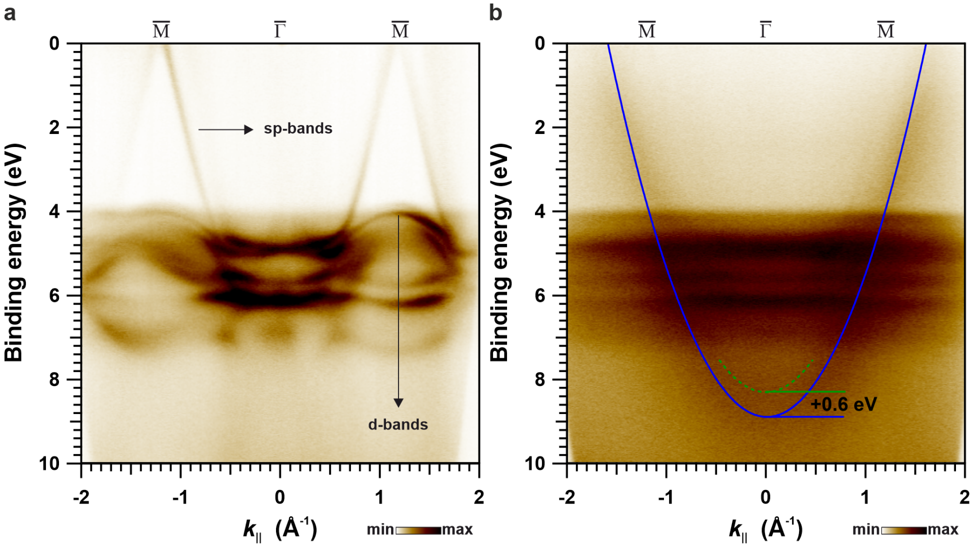

Figure 4.13: Band maps along $\overline{\mathrm{M}}$-$\overline{\Gamma}$-$\overline{\mathrm{M}}$ of the substrate recorded at $h\nu = 30$ eV (p-polarization) for **(a)** clean Ag(111) and **(b)** NiTPP-based network on Ag(111). Adapted from [39].

The NEXAFS spectra obtained for pristine NiTBrPP layer and NiTPP network on Ag(111) are summarized in figure 4.14. Similar to the case of Au(111), the C K-edge spectra reflect the change upon polymerization where the phenyl substituents are forced into a flat configuration. The differences in the N K-edge spectrum of the parent NiTBrPP layer and covalent nanomesh on Au(111) are also apparent in the case of Ag(111). The energy position of the low energy π^*-resonance is shifted with respect to the one of the σ^*-resonance, while the high energy π^*-resonances are broadened. After the formation of the covalent NiTPP network all transitions are shifted towards lower photon energies and the relative intensity of the low energy resonances is reduced. This phenomenon is well-described and indicates an increase in the charge transfer from the substrate that can be related to the formation of the planar covalent nanomesh that is more influenced

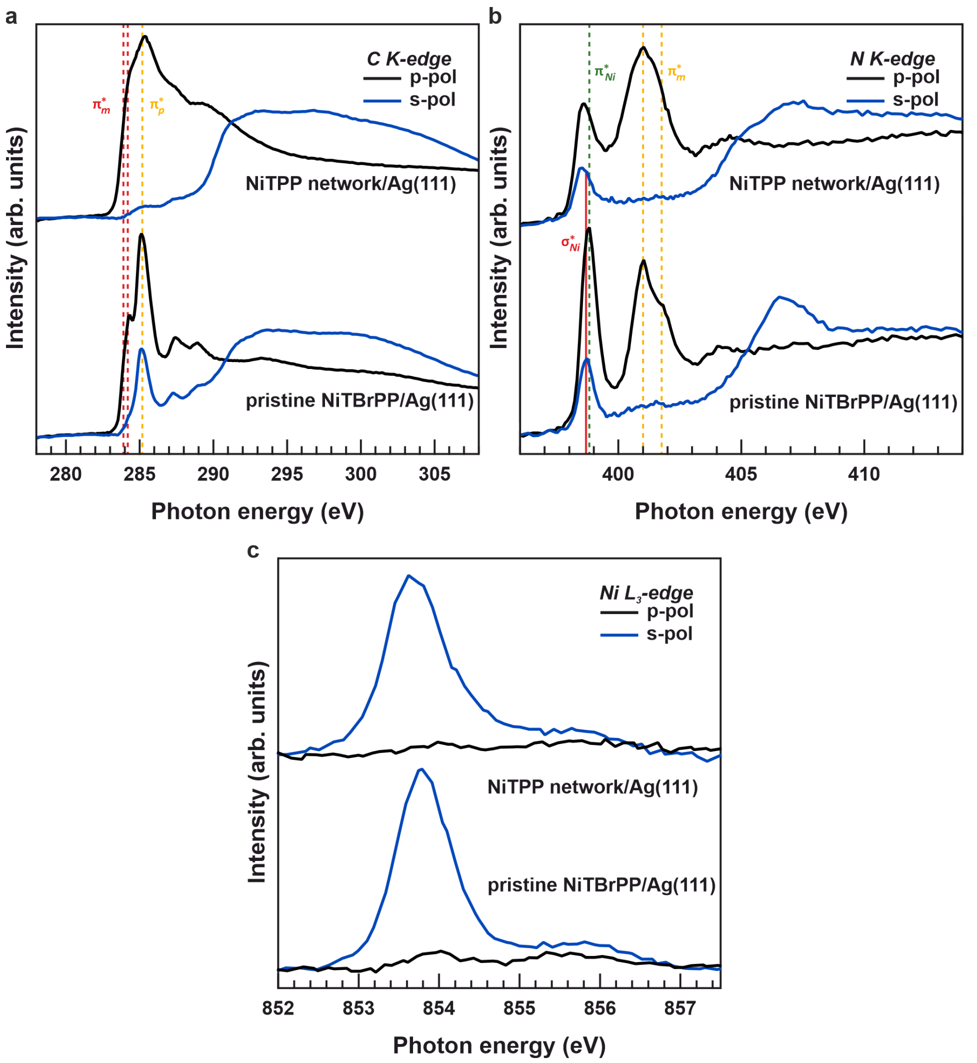

Figure 4.14: NEXAFS spectra recorded across **(a)** the C and **(b)** the N *K*-edge as well as **(c)** the Ni L_3-edge for the pristine NiTBrPP layer and NiTPP-based network on Ag(111). Adapted from [39].

on the more reactive Ag(111) substrate.[107,130] We note that changes sensitive to the Ni to N backbonding cannot be disentangled from the fact that upon increasing the interaction with the substrate also the relative alignment of the NEXAFS resonances might be influenced too.[107] Most importantly, the coordination characteristics of the N-moiety can be summarized to be unaltered. This is further confirmed by the Ni L_3-edge spectra. The shift of ≈ 0.1 eV towards lower photon energies upon NiTPP network formation can be attributed to the increased charge transfer from the substrate that compensates the opposite shift related to the increased Ni to N-backbonding, observed on Au(111). Again, no changes in the spectral shape and satellite structure are evident. This allows concluding that the single-active site character conservation can be extended to more reactive interfaces, which undermines the multifunctionality of the covalent nanomesh. The molecular backbone and functional transition metal center are tuned by the charge transfer at the interface but remain distinct constituents. Therefore, activating molecular magnetism by charge transfer at the interface as observed for single-molecule units appears interesting for understanding differences in the magnetic properties induced by polymerization.[45,131]

4.4 Covalent Nickel Tetraphenylporphyrin Network on Cu(111)

Different initial NiTBrPP coverages below the ML regime have been used as a starting point for the surface-assisted Ullmann coupling on the Cu(111) surface. The Cu 3*p* and Br 3*d* photoelectron lines of the respective pristine NiTBrPP layers at different coverages are depicted in figure 4.15. All spectra have been normalized to the intensity of the Cu 3*p* signal. In both cases the Br 3*d* signal indicates the exclusive presence of a single species with the main line at a binding energy of around 68.6 eV. Since the observed binding energy corresponds to Br chemisorbed to Cu after C-Br bond cleavage,[96,132,133] it can be concluded that NiTBrPP molecules are readily activated when deposited on the surface kept at room temperature. The respective precursor layers, which consist of Ni porphyrin radicals, have then been annealed to 473 K to induce covalent linking of the activated molecular units, while avoiding the decomposition of the molecular layer.[134] The photoelectron spectra acquired after this thermal treatment are also included in figure 4.15. Chemisorbed Br is not removed from the substrate when inducing Ullmann coupling of the molecular units, as is apparent from the Br 3*d* signal that remained constant after annealing for both initial coverages.

The corresponding normalized Ni $2p_{3/2}$ photoelectron spectra for the different initial coverages before and after annealing are further included in figure 4.15. The binding energy characteristic of the Ni centers stabilized within the porphyrin moiety is shifted from 855.6 eV to 853.2 eV after inducing Ullmann coupling. This variation indicates the Ni(II) to Ni(I) reduction upon the polymerization of the molecular units, as further elaborated in the following.[131] Only for an initial coverage of 0.7 ML, or below, the Ni centers are fully converted from their pristine configuration, while a remaining Ni(II) component is appreciable for pristine layers exceeding 0.8 ML. Ullmann coupling on Cu(111) is known to occur through an activated C-Cu-C complex.[135] The reaction confined to an interface free to react requires a catalytic surface that is neither poisoned nor inducing steric hindrance by a too high amount of chemisorbed Br, which is linearly increasing with the coverage of the brominated monomer.[136] We have experimentally observed that this limits the coverage to a maximum of 0.7 ML NiTBrPP for a complete polymerization at the interface. Therefore, we have never exceeded this coverage to avoid the presence of unconverted units.

Cu(111) is a highly reactive surface and it is, thus, surprising that the functional centers of the pristine molecular layer are in the Ni(II) state and are only reduced after inducing Ullmann coupling.[106,131] To better understand this behavior, we have characterized the chemical changes after annealing 0.7 ML of the pristine molecular layer to 473 K by NEXAFS. The respective spectra recorded across both the C and N K-edge are depicted in figure 4.16. NEXAFS is a highly efficient tool to determine the average on-surface orientation of adsorbed molecules. The intensities of the transitions from core levels into antibonding levels probed with the light polarization either parallel (p-polarization) or orthogonal (s-polarization) to the surface normal are different for oriented molecules, which is referred to as linear dichroism.[65] Indeed, the transitions monitored across the C K-edge for porphyrins correspond to 1s transitions into π^*-symmetry MOs and can be separated into macrocycle-based (index m) and phenyl-based MOs (index p).[64,122–125] The C K-edge spectra recorded using p- and s-polarized light display a poor linear dichroism for the as-deposited NiTBrPP on Cu(111), which indicates a significant tilt angle of the phenyl rings with respect to the surface and a partial distortion or rehybridization of the macrocycle. This could be related to the strong interaction of the unsaturated phenyl groups with the surface that is driven by the flexibility of the activated NiTPP radicals. For comparison, the macrocycle of NiTPP deposited on the more reactive Cu(100) surface is mostly planar and parallel to the surface.[45,106,107,131,137] The linear dichroism is drastically enhanced after annealing the molecular layer to 473 K and inducing the intermolecular coupling. From the observed changes in the C K-edge spectrum the formation of a two-dimensional covalent NiTPP-based network is clearly evident. The π^*-resonances are broadened and nearly vanish when using s-polarized light. This is characteristic of the formation of a π-extended covalent nanostructure with flat phenyl substituents, which are closely parallel to the surface plane due to cyclodehydrogenation side reactions (see also chapter 4.2).[18,39]

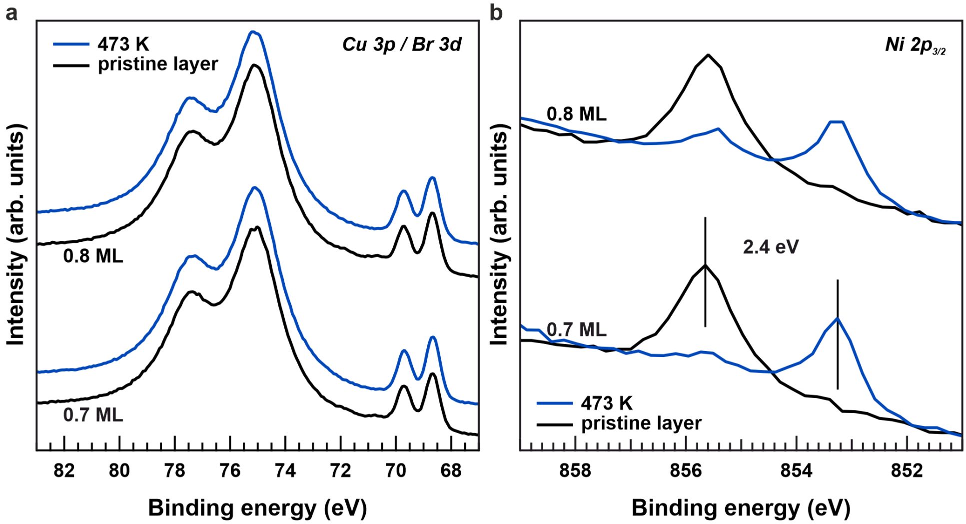

Figure 4.15: **(a)** Cu 3p/Br 3d and **(b)** Ni 2$p_{3/2}$ photoelectron lines collected for different coverages of as-deposited NiTBrPP on Cu(111) and after subsequent annealing to 473 K. The spectra have been recorded at **(a)** $h\nu = 515$ eV and **(b)** $h\nu = 980$ eV (p-polarization) in normal emission. Reproduced from [40].

A better understanding of the interaction of the macrocycle with the surface has been obtained from the N K-edge spectra. The resonances observed in the N K-edge spectra of metalloporphyrins can be classified into pure macrocycle (index m) states and states arising from the mixing of metal $3d$ and N ligand $2p$ states (index Ni).[107,122,123] The low energy region is characterized by a π^*-resonance sensitive to the Ni $3d_{\mathrm{xz,yz}}$ to N ligand $2p_{\mathrm{z}}$ backbonding, which is strongly pronounced for the pristine molecular layer when using p-polarized light. The strong signal in the low energy region for as-deposited NiTBrPP in s-polarization cannot be simply attributed to the characteristic Ni-to-N backbonding resonance since the main position is shifted to slightly lower photon energies. Indeed, a σ^*-resonance, associated with the direct N $2p_{\mathrm{x,y}}$ to Ni $3d_{\mathrm{x}^2-\mathrm{y}^2}$bonding, is known to be strongly pronounced for a weak molecule-substrate interaction when using s-polarized light.[107] Overall, the close energy overlap of the first π^*- and σ^*-resonance at a photon energy of $\approx$ 398.7 eV prevents a clear estimate of the linear dichroism. The resonance at a higher photon energy of $\approx$ 400.9 eV corresponds to pure π^*-symmetry resonances localized on the pyrroles and the perfect linear dichroism (no intensity in s-polarization) indicates a closely planar macrocycle, parallel to the surface. Hence, the residual intensity in s-polarization observed at the C K-edge for the macrocycle might be attributed to the rehybridization of the corresponding MO rather than to a geometric/conformational effect. The Ni(II) to Ni(I) reduction upon formation of the covalent NiTPP-based network after annealing to 473 K is due to an increase in the molecule-substrate interaction, as the phenyl constituents are also forced into a flat configuration. Indeed, this is reflected even in the N K-edge spectra. The resonances corresponding to the Ni-N interaction are quenched upon polymerization as a consequence of the more pronounced charge transfer at the interface.[107] At the same time, all resonances are shifted towards lower photon energies.[130] We further remark on the broadening of the pure macrocycle π^*-resonance, which reflects the formation of a covalent nanomesh with an extended degree of π-conjugation (see also chapter 4.2).[18,39]

NiTPP units within polymerized nanomeshes are known to be dehydrogenated on Au(111).[18,39] The situation on Cu(111) is presumably very similar as these dehydrogenation reactions have also been observed for various porphyrins on this substrate.[100,101] It has been shown that different porphyrin dehydrogenation pathways result in similar spectroscopic and magnetic properties.[39,138] The usage of ensemble techniques to probe the properties of molecules appears reasonable here to gather information about the magnetic properties of the functional Ni centers, embedded into the molecular network. In order to characterize the magnetic properties of the Ni centers within the molecular network, we have conducted XMCD experiments. For one-dimensional porphyrin chains, it has been shown that the magnetic properties of the functional transition metal centers are identical to their single-molecule counterparts.[138] To understand the effect that the embedding of Ni centers into a two-dimensional π-extended structure has on the magnetic properties, a comparison with a proper single-molecule reference appears necessary. Since the as-deposited NiTBrPP units are characterized by the Ni(II) oxidation state, we stabilized NiTPP units that have been cyclodehydrogenated and, thus, flattened (dh-NiTPP) on Cu(111). The deposition of NiTPP at low deposition rates on the hot Cu(111) surface held at 500 K allows us to obtain high coverages of fully dehydrogenated flat molecules as a single-molecule reference. It has been

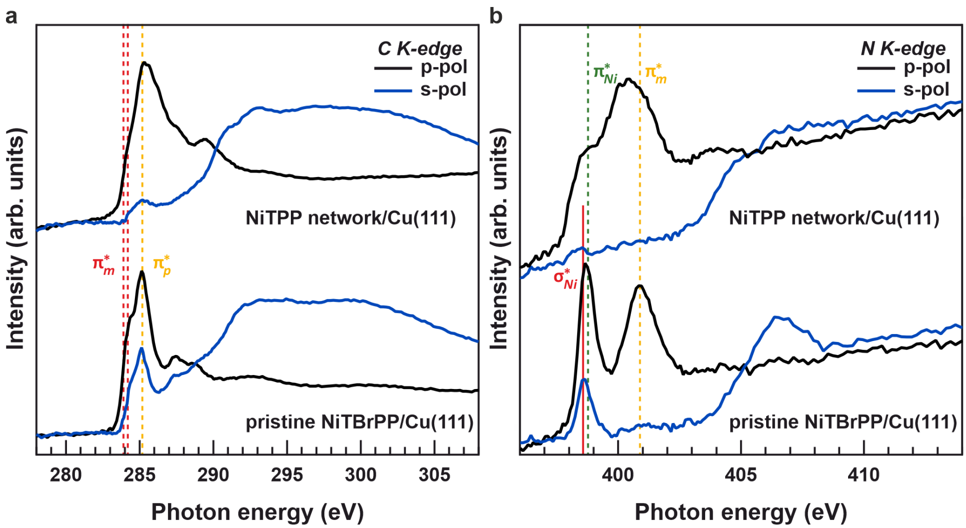

Figure 4.16: NEXAFS spectra recorded across both the **(a)** C and **(b)** N *K*-edge for 0.7 ML pristine NiTBrPP and the NiTPP-based network, obtained by annealing to 473 K, on Cu(111). Reproduced from [40].

reported for NiTPP on Cu(100) that the strong molecule-substrate interaction results in high thermal stability of the molecular layer pinned to the surface.[137] Therefore, a procedure allowing for the direct thermal activation of the molecules before they form a stable self-assembled layer has been realized to fully dehydrogenate the molecular layer. We have estimated an amount of 0.7 ML NiTPP necessary to obtain the dh-NiTPP ML. The rescaling of the coverage accounts for the fact that NiTPP forms closely-packed arrays as the rotational flexibility of the phenyl groups of NiTPP allows their stacking.[139] In contrast, flattened dh-NiTPP molecules might not assemble as closely packed due to the additional bonds created between the macrocycle and phenyl groups.

For this monomer reference layer, the Ni ion is also reduced to the Ni(I) oxidation state. The XMCD signals obtained by subtraction of the absorption spectrum collected with the light of positive helicity (σ^+) from the one collected with the light of negative helicity (σ^-) at the Ni $L_{3,2}$-edge for the dh-NiTPP layer and NiTPP network, obtained by annealing 0.5 ML of NiTBrPP to 473 K, are depicted in figure 4.17. A magnetic field $B = 6.8$ T has been used to reach conditions close to saturation. For this definition the dichroic signal at the L_3-edge is negative. Measurement geometries at photon incidence angles of $\theta = 0°$ (normal, left) and $\theta = 70°$ (grazing, right) with respect to the surface normal have been realized by rotating the sample, to keep the photon propagation direction along the applied magnetic field. The spectra characteristic of the NiTPP network have been multiplied to obtain the same XMCD magnitude at the L_2-edge, to account for the lower signals due to the lower coverage necessary for the preparation. It has to be noted that the signals obtained at normal incidence are characterized by a generally higher intensity, as is evident from the overview of their integrals presented in figure 4.18. Data obtained in grazing incidence is shown in similar magnitude here to enhance the clarity of the observed effects. The collected XMCD signals are similar when it comes to the energy position where the maximum effect (≈ 852.7 eV) is observed. Indeed, the spectral shape is very similar to the ones observed for paramagnetic transition metal ion $3d^9$ configurations.[45,70,140] This is fitting well with a Ni(II) to Ni(I) reduction at the reactive Cu(111) interface, when compared to the molecular gas phase properties. Though they are also similar in shape, the XMCD signals in figure 4.17 for both geometries indicate differences in the orbital momentum configurations characteristic of the Ni(I) centers of the dh-NiTPP single-molecule reference and NiTPP-based covalent network. To further elaborate on this, a sum rule analysis has been performed assuming one hole for the singly unoccupied Ni $3d_{\mathrm{x}^2-\mathrm{y}^2}$-based MO.[68,69]

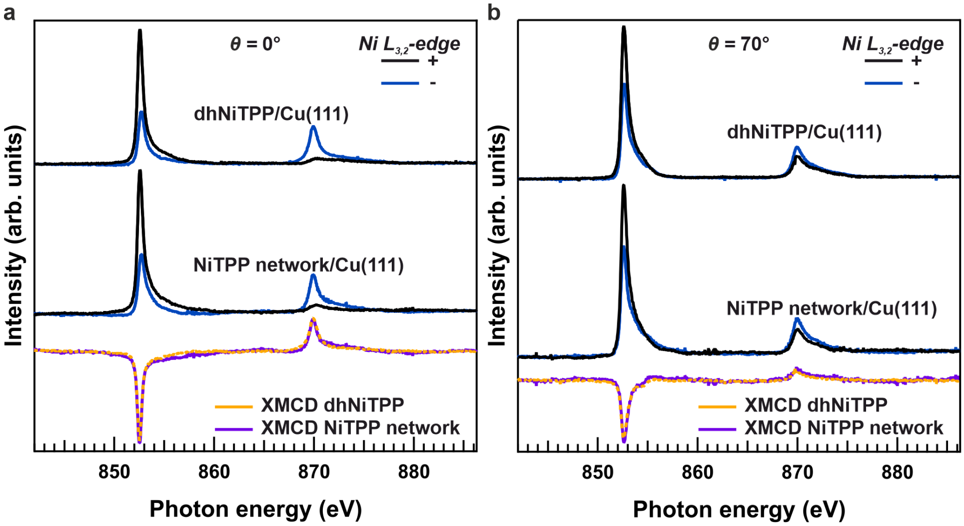

Figure 4.17: XMCD signals obtained across the Ni $L_{3,2}$-edge ($B = 6.8$ T along the photon incidence axis) for both dh-NiTPP and NiTPP network on Cu(111) for an incidence angle of: **(a)** $\theta = 0°$ and **(b)** $\theta = 70°$. All spectra of NiTPP network have been multiplied to get the same intensity magnitude at the Ni L_2-edge as for the dh-NiTPP layer. Reproduced from [40].

Table 4.1: Magnetic moments obtained by sum rule analysis from different measurement geometries at $B = 6.8$ T for both dh-NiTPP and NiTPP network on Cu(111).

System		$\boldsymbol{\theta = 0°}$	$\boldsymbol{\theta = 70°}$
dh-NiTPP	μ_S^{eff} [μ_{B}]	1.36 ± 0.36	0.50 ± 0.13
	μ_L [μ_{B}]	0.10 ± 0.03	0.12 ± 0.03
NiTPP network	μ_S^{eff} [μ_{B}]	1.40 ± 0.37	0.45 ± 0.11
	μ_L [μ_{B}]	0.24 ± 0.05	0.05 ± 0.02

The deduced orbital and effective spin magnetic moments (μ_L and μ_S^{eff}) in the respective geometries for the different systems are summarized in Table 1. The background-subtracted $\sigma^+ + \sigma^-$ absorption spectra displayed in figure 4.18 have been integrated and used to calculate the isotropic absorption intensity. We have assumed the isotropic absorption intensity as $1.5 \cdot (\sigma^+ + \sigma^-)$. Indeed, this approximation is not valid for highly anisotropic environments as elaborated by Stepanow

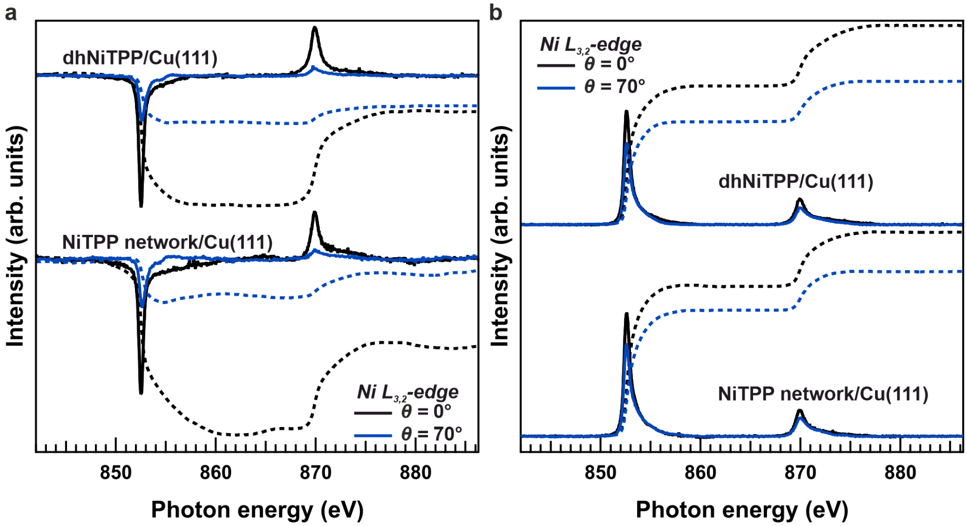

Figure 4.18: Integrals (dashed lines) of the **(a)** XMCD signals and **(b)** helicity-averaged Ni $L_{3,2}$ absorption spectra characteristic of both dh-NiTPP and the NiTPP network on Cu(111). The spectra have been obtained at $B = 6.8$ T for $\theta = 0°$ and $\theta = 70°$, respectively. All spectra of the NiTPP network have been multiplied to get the same intensity magnitude at the L_2-edge as for the dh-NiTPP layer. Reproduced from [40].

and coworkers.[70] We are aware of the correction they have introduced to account for an unpaired electron in the $3d_{\mathrm{x}^2-\mathrm{y}^2}$-based MO, as expected for a Ni(I) configuration as well. They have observed a $(\cos^2(\theta)+1)/2$ dependence of the $\sigma^+ + \sigma^-$ spectral intensity and accounted for this when calculating the isotropic absorption intensity. The respective angular dependence of the absorption intensity, however, is not reproduced for the systems studied here. Indeed, the interaction with the Cu(111) surface is very strong here as it even results in the Ni(II) to Ni(I) reduction. Therefore, we attribute the deviation to the strong molecule-substrate interaction. The linear dichroism apparent in the Ni absorption spectra of Ni ions characterized by only unoccupied $3d_{\mathrm{x}^2-\mathrm{y}^2}$-based MOs is reduced when increasing the Ni substrate interaction.[45,131] This justifies the deviation from the angular dependence of the integrals based on a consideration of the $3d_{\mathrm{x}^2-\mathrm{y}^2}$-based MO orientation with respect to the electric field of the incident photon. The absolute values of the sum rule results have to be considered with care accordingly. Our systematic comparison of the two systems, however, allows for a determination of the proper relative trend due to the similarities in the angular behavior of the integrated absorption intensity. For both dh-NiTPP molecules and the NiTPP-based network the $\sigma^+ + \sigma^-$ spectral intensity is similarly reduced by $\approx 30\%$, as evident from the spectra depicted in figure 4.18. Therefore, errors coming from assumptions on the isotropic absorption intensity lead to wrong absolute results when doing the sum rule analysis. Yet, the relative trend can be considered well-displayed due to the similarities in the angular trend for the absorption intensities of both systems. Note that the errors given for the calculated moments have been further obtained by varying the subtracted background and the integral ranges in the sum rule analysis, by a few eV, to account for spectral noise. Furthermore, it has to be emphasized that the Ni centers characteristic of the dh-NiTPP single-molecule reference and NiTPP-based covalent network on Cu(111) could vary slightly in their oxidation state, as the coinciding XMCD maxima positions might not necessarily imply an identical electronic configuration. Again, the angular dependence of the $\sigma^+ + \sigma^-$ spectral intensity that is practically identical has to be highlighted. Therefore, slight variations in the oxidation state would not affect the relative trend, but just the absolute values of the calculated magnetic moments.

When comparing the two systems, it is evident that the formation of the π-extended NiTPP network results in an enhancement of the out-of-plane orbital magnetic moment, while the in-plane orbital magnetic moment is quenched with respect to the single-molecule reference. The spin magnetic moment behaves similarly for both systems. An angle-dependent deviation from the spin magnetic moment expected for a Ni $3d^9$ configuration with one unpaired electron can be attributed to the intra-atomic magnetic dipole moment.[141] However, the anisotropy of the spin magnetic moment is very similar for both the NiTPP network and dh-NiTPP.[142] This, again, confirms the conclusion based on the XMCD maxima position that the strong charge transfer at the interface leads to similar Ni(I) species in both cases and that relative trends based on our comparative approach are well-displayed.

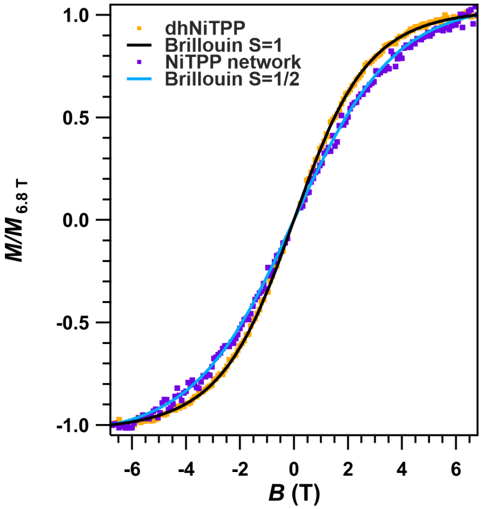

Figure 4.19: Magnetization curves acquired for both dh-NiTPP and NiTPP network on Cu(111) at $\theta = 0°$. Adapted from [40].

In contrast to what would be expected for similar magnetic Ni centers, the magnetization curves of both systems significantly differ, as is evident from figure 4.19. We observed no differences between the magnetization curves at normal and grazing incidence for both systems. Therefore, the magnetization curves of both dh-NiTPP and the NiTPP network on Cu(111) have been used to fit the molecular spin S by using Brillouin functions that account for a spin-only paramagnetic response at $T = 2.5$ K. The magnetization M has been normalized to 1 at $B = 6.8$ T for all curves. For the NiTPP-based network the $S = 1/2$ Brillouin function reproduces the magnetic response, which agrees well with the XMCD findings. In contrast, dh-NiTPP on Cu(111) apparently exhibits a $S = 1$ behavior. We note that the sum rule error does not justify this discrepancy. More importantly, $S = 1$ would correspond to a $3d^8$ Ni center in a high-spin configuration, for which a different shape of the absorption spectra compared to the experimental one is expected, as a consequence of an additional $3d$-hole.[45,143,144] Therefore, we expect a similar Ni $3d^9$ configuration for both the NiTPP network, which exhibits the expected $S = 1/2$ behavior, and the dh-NiTPP, whose magnetic response appears to be ferromagnetically enhanced. We note that Ruderman–Kittel–Kasuya–Yosida (RKKY) exchange interaction mediated by substrate electrons has been observed for similar molecular layers.[145] For ZnTPP units modified via cyclodehydrogenation, a preferential on-surface orientation has been found.[105] This leads to preferential intermolecular arrangements, even though there is no long-range order in the molecular layer. A rough estimate of the published data allows to identify a quite narrow window of 1.5-1.7 nm as the distance between the Zn centers, which we assume as representative for the dh-NiTPP units on Cu(111). The same statement applies to the polymerized NiTPP network, for which a similar distance window between the transition metal centers can be estimated (see also chapter 4.2).[39] Hence, even with the assumption of well-defined RKKY interactions in unordered molecular layers, different magnetic responses of the two systems as a consequence of pronounced variations in the Ni center distances are unlikely. Furthermore, the Ni center distance is in the range where the RKKY exchange interaction is expected to be rather weak on Cu(111).[146–148]

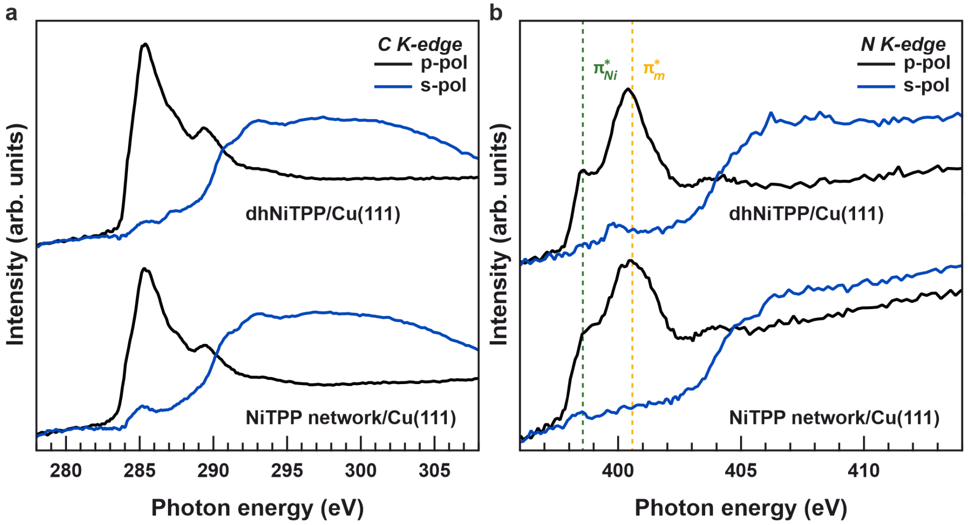

Figure 4.20: NEXAFS spectra recorded across both the **(a)** C and **(b)** N K-edge for NiTPP-based network and dh-NiTPP on Cu(111). Reproduced from [40].

A close inspection of the NEXAFS spectra recorded across the C and N K-edge of both systems, which are displayed in figure 4.20, indicates that the interaction of the macrocycle of dh-NiTPP with the supporting substrate is stronger than in the case of the NiTPP network. Thereby, the spectra of the NiTPP network, obtained by annealing 0.7 ML of NiTBrPP, are displayed and compared to the ML reference film of dh-NiTPP. The C K-edge spectra of both systems recorded with s-polarized light display very low intensity at the LUMO resonances as compared to the p-polarization spectra. This implies that the thermally activated cyclodehydrogenation of the phenyl substituents (flattening) is effective when depositing NiTPP directly onto the hot Cu(111) surface.[104,137] Since both the NiTPP network and the dh-NiTPP layer yield a similar NEXAFS linear dichroism, we conclude that their constituents display a similar geometric orientation. Indeed, the π^*-symmetric resonances probed by p-polarized light are broadened slightly when comparing the NiTPP network and the dh-NiTPP. This is evident more clearly in the N K-edge spectra, where the pure macrocycle states, denoted by the index m, are broadened significantly for the polymerized structure. Their maximum position is at a photon energy of $\approx$ 400.6 eV for the NiTPP network on Cu(111) and a shift of $\approx$ 0.2 eV towards lower photon energies is observed for the dh-NiTPP layer. We attribute this to a stronger molecule-substrate interaction characteristic of dh-NiTPP on Cu(111).[130] This stronger interaction, which we attribute to a shorter molecule-substrate distance characteristic of the dh-NiTPP layer when compared to the polymerized NiTPP-based structure, may explain a significant difference in the amount of charge transferred to the molecular macrocycle. For the dh-NiTPP layer on Cu(111), this may result in a ferromagnetic interplay between the Ni $3d$-based MOs and macrocycle-based MOs.[149]

Indeed, from our theoretical model, based on the molecular cluster approach already validated to transition metal (Fe, Co and Ni)TPP,[143,150–153] we find that the Ni-Cu distance can be varied in a certain range for which the Ni(II) to Ni(I) reduction is observed. The details on the calculations that have been performed are elaborated in chapter A.1. As our gas phase calculations have revealed that the spiral dehydrogenated form is the most stable one,[126] we have limited our attention to this NiTPP derivative in order to understand the implications of on-surface polymerization. Upon Ullmann polymerization at the interface, the structures are formed in the kinetic limit so that there is a random relation between the supporting substrate when it comes to the adsorption site and azimuthal orientation (see also chapter 4.2).[18,39] It has been shown for similar Ullmann coupling phenomena on the Au(111) and Ag(111) surfaces that the Ni centers stabilized in the polymeric nanomeshes are still characterized by a uniform character.[39] An equivalent small influence of the random distribution of Ni centers on the Cu(111) surface is also supported by the similarity in energy of different NiTPP units on the various adsorption sites on the Cu(111) surface.[139] Our simplified theoretical model of the network formed via Ullmann coupling is based on a tetramer, constituted by covalently connected spiral dh-NiTPP units. The molecular cluster approach is used to simulate the Cu-Ni interaction in order to account for the central Ni ion reduction at the interface with respect to the gas phase Ni(II) configuration as demonstrated in previous studies.[143,150–153] A Ni-Cu distance of 2.1 Å has been obtained from periodic calculations for similar systems where the central Ni centers of porphyrins have been experiencing similar charge transfer and consequently reduced to Ni(I) on Cu(100).[106] In our model we have observed the Ni(II) to Ni(I) reduction already at distances of 2.2 Å. Therefore, we conclude that there exists a distance window for which the Ni(II) to Ni(I) reduction at the interface might appear. This is strongly supported by our experimental data that suggests a difference in the Ni-Cu distance for both systems, for which the Ni oxidation state is quite similar. For obtaining information sensitive to the effects on the Ni 3d-based MOs induced by polymerization, we have assumed the same Ni-Cu distance (2.1 Å) for the supported dh-NiTPP and truncated NiTPP network. Top and side views of the obtained structures for the supported dh-NiTPP and NiTPP-based truncated network are displayed in figure 4.21. For both systems, the molecular constituents remain in a flat configuration after the reduction of the Ni centers due to the interaction with the substrate in accordance with the experimental findings discussed above. A summary of the calculated number of unpaired electrons, the average Ni-N distances as well as the Ni-N/Ni-Cu Nalewajski-Mrozek[154] bond multiplicity indices $^{\mathrm{NM}}\mathrm{I}$ for both supported structures is provided in table 4.2. All parameters suggest that there is a large similarity between the Ni centers characteristic of the single-molecule reference and the polymerized structure. Further information about the properties of the two systems is evident from figure 4.22, which displays the Ni partial density of states (PDOS) for selected Ni 3d-based MOs for both the spin-up (positive) and spin-down (negative) channels. The presented 3d-based MOs are the ones relevant for the orbital magnetic moment of the coordinated Ni centers. The Fermi level is at ≈ -5 eV for both systems. In both cases, the partially unoccupied MOs are the spin-down Ni $3d_{\mathrm{x}^2-\mathrm{y}^2}$-based ones, in agreement with a Ni $3d^9$ configuration suggested by the experimental findings. The energy differences between the Ni $3d_{\mathrm{x}^2-\mathrm{y}^2}$-based and Ni $3d_{\mathrm{xy}}/3d_{\mathrm{yz}}$-based MOs characteristic of dh-NiTPP in the spin-down channel are indicated by blue arrows with the numeric values indicated. These energy differences are further included in the Ni PDOS characteristic of a simplified covalent NiTPP-based network. The right ends of the arrows are shifted to the maximum of the spin-down Ni $3d_{\mathrm{x}^2-\mathrm{y}^2}$-based MO for better comparison, which is stabilized around 0.1 eV when comparing the supported NiTPP polymer with dh-NiTPP. We note that the relative energy-level alignment of the Ni 3d-based MOs is not changed for the two systems, which allows concluding that the effects induced by polymerization are not the origin of change in the orbital magnetic moment anisotropy. We note that MOs of the same symmetry are found for the supported dh-NiTPP and truncated NiTPP network, but delocalization effects are observed after polymerization for the out-of-plane 3d-based MOs as apparent from figure 4.23 and figure 4.24. In contrast to the in-plane 3d-based MOs that are localized at only one single moiety, they spread over the entire monomer and both adjacent and/or opposite moieties are involved in the delocalization. The most relevant variation between dh-NiTPP and NiTPP network is that the out-of-plane MOs of the polymerized structure are characterized by pronounced delocalization effects.

As such, the formation of the more rigid π-extended structure allows to influence the interaction with the substrate and the thereby observed increase in the orbital momentum anisotropy is known to be beneficial to increase of the magnetic anisotropy.[83] It has been shown for d^9 systems where the functional transition metal ion is embedded in a similar environment that the orbital momentum anisotropy can be rationalized in terms of spin-orbit coupling effects.[70] The orbital angular momentum of the crystal field states is restored for the transition metal ion as excited states can admix differently depending on the orientation of the paramagnetic complex in a magnetic field. Indeed, the thereby induced orbital momentum has been shown to increase for decreasing energy differences between the Ni $3d_{x^2-y^2}$-based MO and the Ni $3d_{xy}$-(out-of-plane) or the Ni $3d_{xz,yz}$-based MOs (in-plane).[70] For the two systems presented here the Ni-Cu distance is subject to variation and increased for the more rigid NiTPP network, which corresponds to an effective axial elongation of the square pyramidal ligand field upon polymerization of NiTPP units. The relative energy-level alignment of the 3*d*-based MOs is expected to be altered in accordance with the changes necessary for rendering an enhanced orbital magnetic moment anisotropy of Ni centers characteristic of the NiTPP-based network.[155]

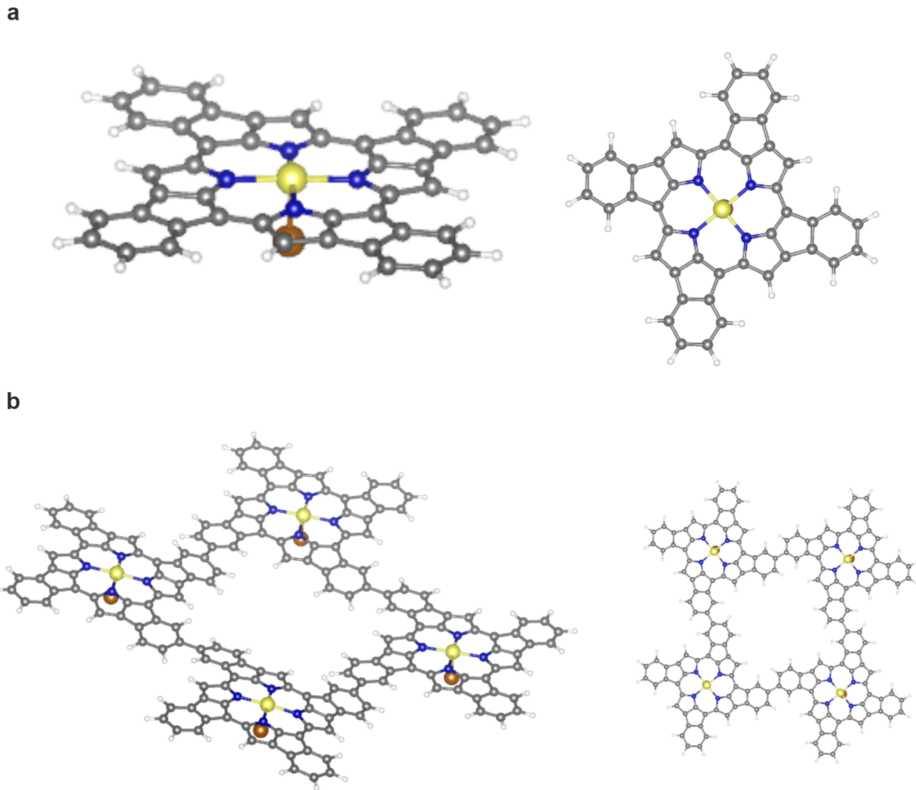

Figure 4.21: Side and top views of the structures obtained within the molecular cluster approach for a stabilized **(a)** dh-NiTPP and a stabilized **(b)** truncated NiTPP network. Adapted from [40].

Table 4.2: Summary of the calculated number of unpaired electrons on the Ni 3*d*-based MOs, the Ni-N bond length and the Nalewajski-Mrozek bond multiplicity indexes ^{NM}I for the supported dh-NiTPP and the truncated NiTPP network.

System	**Unpaired electrons**	**Ni-N [Å]**	$^{NM}I_{Ni\text{-}N}$	$^{NM}I_{Ni\text{-}Cu}$
dh-NiTPP	1.06	2.006	0.309	0.537
NiTPP network	1.06	2.009	0.306	0.522

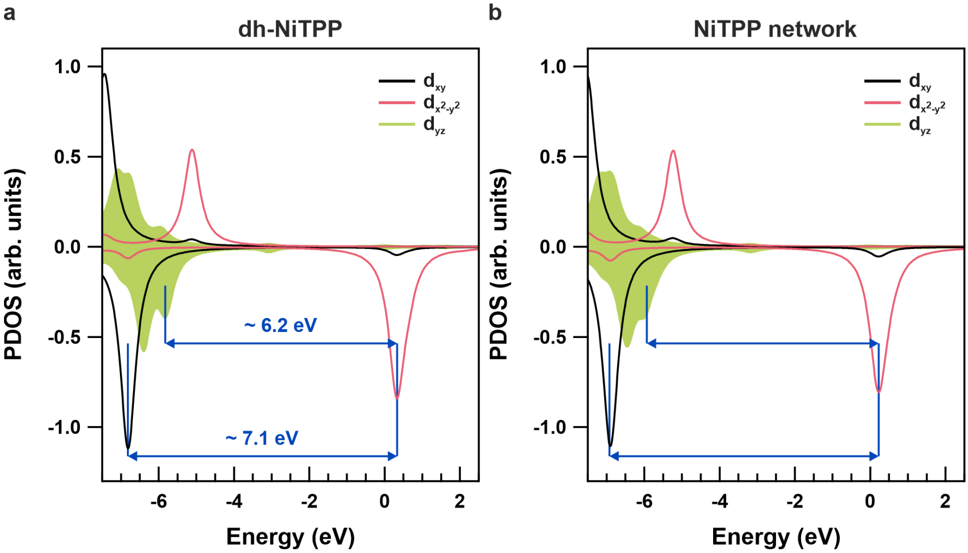

Figure 4.22: Ni 3*d*-based PDOS (250 meV width) calculated for both a stabilized **(a)** dh-NiTPP and a stabilized **(b)** truncated NiTPP network with positive (negative) values corresponding to spin up (down) electrons. The blue arrows indicate the constant energy difference between the frontier Ni 3*d*-based MOs, which are relevant for the orbital magnetic moments as elaborated in the main text. Adapted from [40].

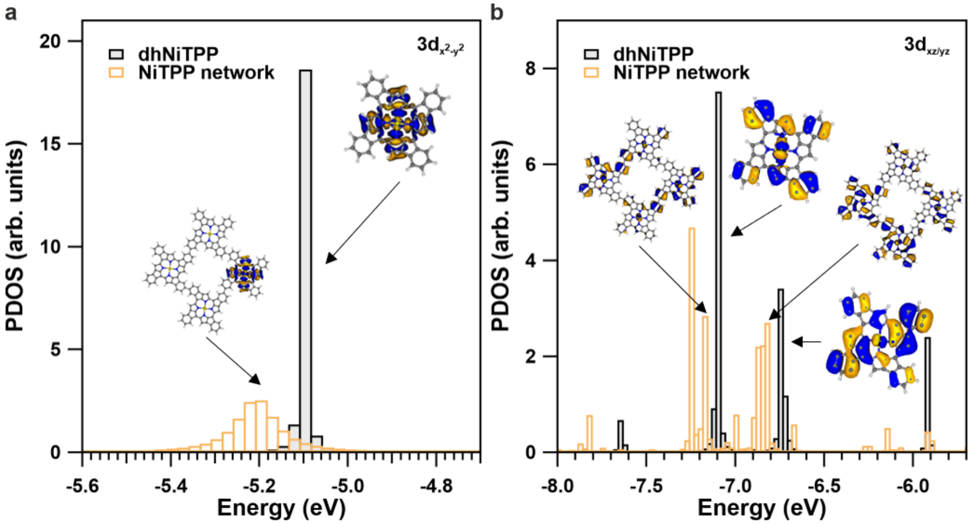

Figure 4.23: Spin-up Ni **(a)** $3d_{x2-y2}$ and **(b)** $3d_{xz/yz}$ PDOS (5 meV width) for selected MOs of a stabilized dh-NiTPP and a stabilized NiTPP network. Contour plots for selected MOs, whose energy positions are indicated by arrows, are also included. Reproduced from [40].

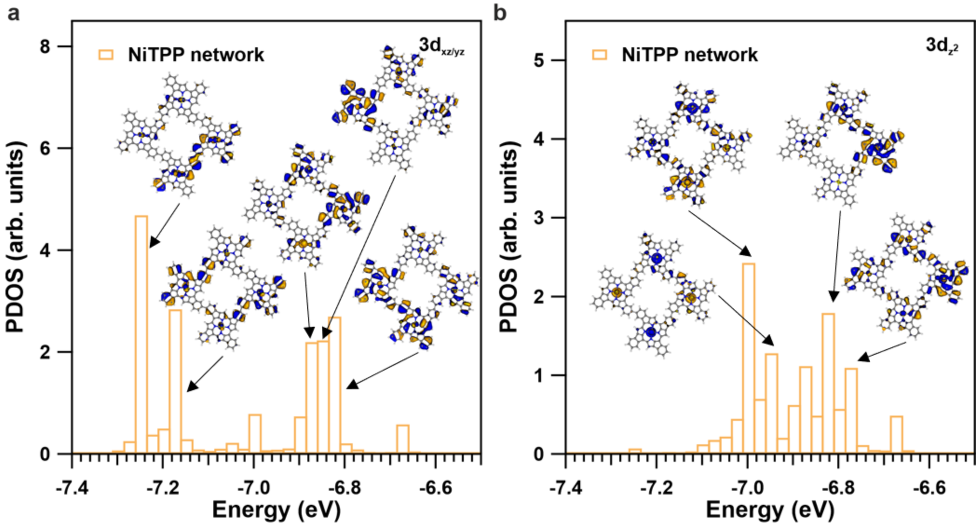

Figure 4.24: Spin-up Ni **(a)** $3d_{xz/yz}$ and **(b)** $3d_{z^2}$ PDOS (5 meV width) for selected MOs of a stabilized NiTPP network. Contour plots for selected MOs, whose energy positions are indicated by arrows, are also included. Reproduced from [40].

5 Nickel-1,2,4,5-Tetracyanobenzene Metal-Organic Frameworks on Coinage Metals

This chapter is partially based on one first author work, submitted to *ACS Nano* as: **Emergence of band structure in a two-dimensional metal-organic framework upon hierarchical self-assembly** by Baranowski, D.; Thaler, M.; Brandstetter, D.; Windischbacher, A.; Cojocariu, I.; Mearini, S.; Chesnyak, V.; Schio, L.; Floreano, L.; Gutiérrez Bolaños C.; Puschnig, P.; Patera, L. L.; Feyer, V.; and Schneider, C. M.. The STM/STS measurements have been performed under lead of Thaler, M. and Patera, L. L., where I have been involved during my period as visiting student at the University of Innsbruck. I have analyzed the data together with Thaler, M. and Patera, L. L., receiving essential contributions from Chesnyak, V.. XPS/NEXAFS data have been collected together with Cojocariu, I. and Feyer, V. under guidance of Schio, L.; Floreano, L. and Gutiérrez Bolaños, C.. I have performed the valence band spectroscopy measurements together with Cojocariu, I.; Mearini, S. and Feyer, V.. I have analyzed the data and received feedback from all people involved in the valence band spectroscopy and XPS/NEXAFS measurements. The calculations have been performed by Brandstetter, D.; Windischbacher, A. and Puschnig, P.. I have written the first draft, with essential contributions from Thaler, M.; Patera, L. L.; Brandstetter, D.; Windischbacher, A. and Puschnig, P., and all co-authors have contributed to improvements before submission. The project has continuously been supervised by Feyer, V. and Schneider, C. M..

This chapter is about the transition from Ni-TCNB complexes to a 2D-MOF, where the Ni centers are interconnected by different cyano (CN) groups of TCNB. Thereby, the functional center characteristic of NiTPP has been mimicked, while the frontier electronic structure of the Ni centers can be tuned with respect to NiTPP, and well-ordered nanostructures can be realized. Consequently, the Ni $3d$-based hybrid states become experimentally accessible in valence band spectroscopy measurements, permitting to understand how π-delocalization emerges within 2D-MOFs. The band character of the Ni $3d$-based states is robust upon increasing the interaction with the supporting surface, demonstrating the possibility to tune 2D-MOFs via charge transfer from the substrate.

5.1 Supramolecular Engineering on Metal Surfaces

The formation of single-layer (metal-)organic structures has been realized by combining metal units with organic ligands and confining the self-assembly process to a solid surface under UHV conditions.[19] Thereby, strongly directional driving forces as hydrogen bonding, metal-ligand and (metal-)organic-surface interactions have been rationalized in the structural design.[20] Given the chemical versatility of relatively simple organic linkers a plethora of coordination motifs based on variable functional groups like CN, hydroxyl, carboxyl, and amino has been realized, resulting in various lattices, from square to kagome symmetries.[156] When designing extended structures, referred to as 2D-MOFs, understanding the emergence of π-delocalization is very important.[24,25] In many cases, the formation of 2D-MOFs occurs gradually from a pristine layer of the organic linker, stabilized at the supporting surface and designed for crosslinking TM centers by coordinate bonds, to TM-organic complexes and then further to the extended structure.[86,157] Probing this transition allows valuable insights for band structure engineering.

5.2 From Metal-Organic Complexes to Metal-Organic Framework on Au(111)

The formation of our metal-organic nanostructures with controlled stoichiometry starts from a ML of TCNB on Au(111) followed by depositing Ni atoms at room temperature. Maintaining the sample at 300 K for one hour results in thermodynamically stable metal-organic phases that have subsequently been transferred into the LT-STM, where the sample has been cooled down to ≈ 9 K.[86] Depending on the deposited Ni amount, two different $\mathrm{Ni(TCNB)_x}$ $(\mathrm{x} = 2, 4)$ phases form: while at low Ni coverages the $\mathrm{Ni(TCNB)_4}$ phase is observed, the $\mathrm{Ni(TCNB)_2}$ phase becomes progressively predominant upon increasing the amount of Ni. This behavior is similar to what has been observed for metal-organic phases consisting of TCNB and Fe, where the structural adaption depends on the Fe/TCNB ratio.[86] In the following we refer to the isolated $\mathrm{Ni(TCNB)_4}$ structure as Ni-Complex while the extended two-dimensional $\mathrm{Ni(TCNB)_2}$ structure is denoted as Ni-MOF. Topographic STM images for all preparation steps are included in figure 5.1. The characteristic Au(111) reconstruction is evident in the STM images of all the overlayers, indicating a weak molecule-substrate interaction.[158,159] In both metal-organic phases, the Ni sites are in a square planar coordination environment, indicating a directional character of the interaction between the CN groups of TCNB and the Ni centers. A first estimate based on the size of gas-phase TCNB yields a Ni-N distance of 2.01 Å and 1.80 Å from the STM images of the Ni-Complex and the Ni-MOF, respectively. We note that within the assumed error range this agrees well with the Ni-N distance observed in Ni-containing porphyrins/phthalocyanines.[160] Indeed, similar structures based on different transition metal centers proved as templates in the thermally activated on-surface synthesis of phthalocyanine compounds.[161–165] The number of TCNB units per nm^2 remains practically constant during the formation of our (metal-)organic structures, and is calculated to be ≈ 2 molecules per nm^2. A 1:1 Ni-TCNB structure with all TCNB CN groups involved in coordination bonds has not been observed yet, even when increasing the Ni amount. Instead, only metal clusters form. For reference, a 1:1 Mn-TCNB metal-organic network reported in the literature has only been achieved upon simultaneous co-deposition of Mn and TCNB onto a pristine surface.[162] In this structure the amount of TCNB per nm^2 is substantially different from the one characteristic of $\mathrm{Mn(TCNB)_2}$. We conclude that the Ni-induced rearrangement of the pristine TCNB/Au(111) interface is similarly limited to the formation of $\mathrm{Ni(TCNB)_2}$ due to the strong intermolecular TCNB interaction. When starting from a saturated TCNB layer, the

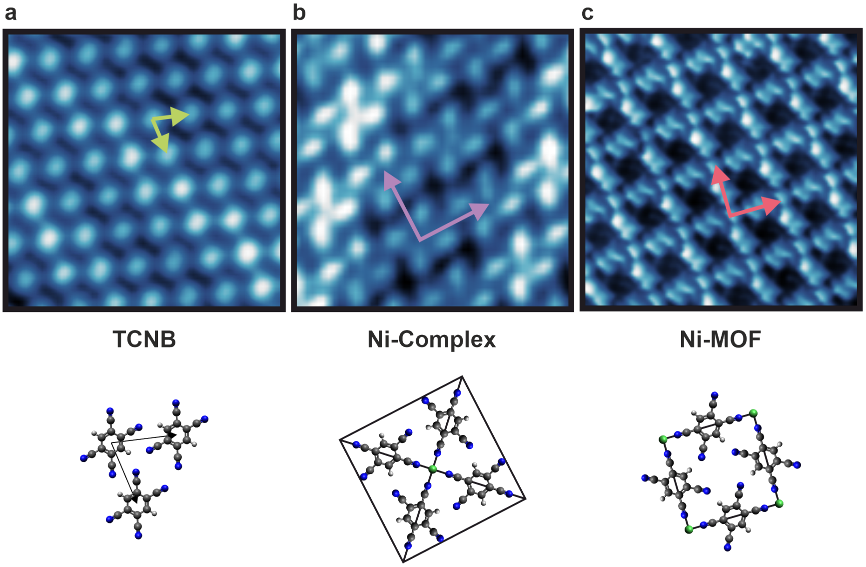

Figure 5.1: Topographic STM images ($6.0 \cdot 6.0$ nm^2) acquired for the phases of interest: **(a)** TCNB; **(b)** Ni-Complex; **(c)** Ni-MOF. The unit cells and the consequent structural models are also included. The unit cell of as-deposited TCNB ($V = 350$ mV, $I = 50$ pA) on Au(111) can be described by two equivalent basis vectors $a_{1,2} = 0.82$ nm with a spanning angle $\alpha = 74°$. Both Ni-Complex ($V = 300$ mV, $I = 30$ pA) and Ni-MOF ($V = 5$ mV, $I = 20$ pA, molecule-functionalized tip) are square structures with $a = 1.70$ nm and $a = 1.16$ nm, respectively. Adapted from [41].

intermolecular TCNB distances define the resulting network. We, thus, propose intermolecular interactions as the dominant drivinig force in the self-assembly process, even upon deposition of Ni. Actually, the arrangement of the TCNB units around Ni in both the Ni-Complex and Ni-MOF introduces a chirality with respect to the equivalent high-symmetry directions of the supporting Au(111) surface.[166] We observe both chiral assemblies, which are obtained by a mirror operation along one of the high-symmetry directions of the substrate. Within different domains, the assemblies around adjacent Ni sites exhibit the same chirality. This agrees with the observation that for directional metal-organic bonds the intermolecular interaction between the organic units is maximized if neighboring chiral units are equally oriented.[167]

We have probed the local electronic structure of the different phases by STS. dI/dV spectra acquired above TCNB units (black) and Ni centers (blue) are displayed in figure 5.2a. The spectrum of TCNB on Au(111) is characterized by one main feature at $V \approx 1900$ mV, which is attributed to the LUMO of TCNB.[86] For the Ni-Complex, electronic states are detected at $V \approx -1050$ mV and $V \approx 1300$ mV, while for the Ni-MOF, they lie at $V \approx -1200$ mV and $V \approx 1680$ mV. Such changes of the electronic states upon coordination with Ni indicates the formation of new electronic levels, resulting from the hybridization of Ni and TCNB states.[168,169] Constant-current dI/dV maps obtained for Ni-MOF indicate a contribution from Ni sites to both the occupied state and the feature at positive bias derived from the former TCNB LUMO.

Thereby, figure 5.2b presents a topographic STM image displayed as reference for the corresponding dI/dV maps (figure 5.2c, d) collected at both the characteristic occupied and unoccupied features.

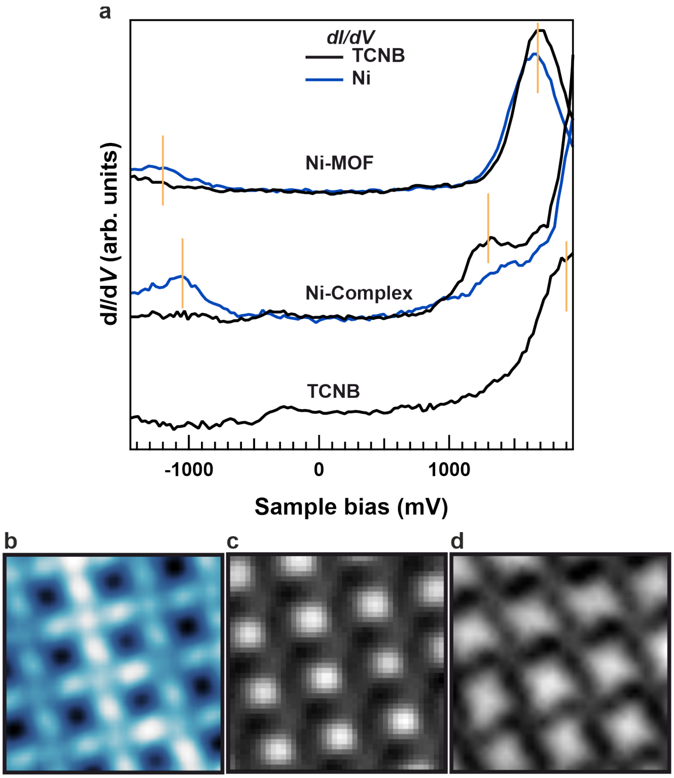

Figure 5.2: **(a)** dI/dV spectra on TCNB, Ni-Complex and Ni-MOF on Au(111). For the metal-organic structures, spectra have been collected both on Ni (blue) and TCNB (black). The feedback has been opened at $V = 400$ mV and $I = 50$ pA for all spectra. **(b)** Topographic STM image ($3.9 \cdot 3.9$ nm^2, $V = -1250$ mV and $I = 50$ pA) of the Ni-MOF phase on Au(111). **(c)** Constant-current dI/dV map recorded with a set point of $V = -1250$ mV and $I = 50$ pA. **(d)** Constant-current dI/dV map recorded with a set point of $V = 1600$ mV and $I = 50$ pA. A voltage modulation of 50 mV at 759 Hz has been used for collecting all spectra and maps. Adapted from [41].

To complement the STM/STS characterization, we have conducted NEXAFS experiments to probe the on-surface orientation of the different functional TCNB constituents.[64] The NEXAFS spectra recorded across the C and N K-edge for TCNB, Ni-Complex and Ni-MOF on Au(111) are shown in figure 5.3a, b. In the C K-edge spectra, the region ≈ 285 eV (orange box) is attributed to π^*-symmetric resonances localized on the benzene ring.[170,171] The respective resonances are largely suppressed in s-polarization and only observed when using p-polarized light, suggesting that the benzene ring adsorbs flat on the surface without significant deformation.[65,172] Similarly, in the N K-edge spectra the π^*-symmetric resonance at a photon energy of ≈ 401 eV, associated with the CN groups of TCNB, is only observed in p-polarization.[173] A flat on-surface orientation of the

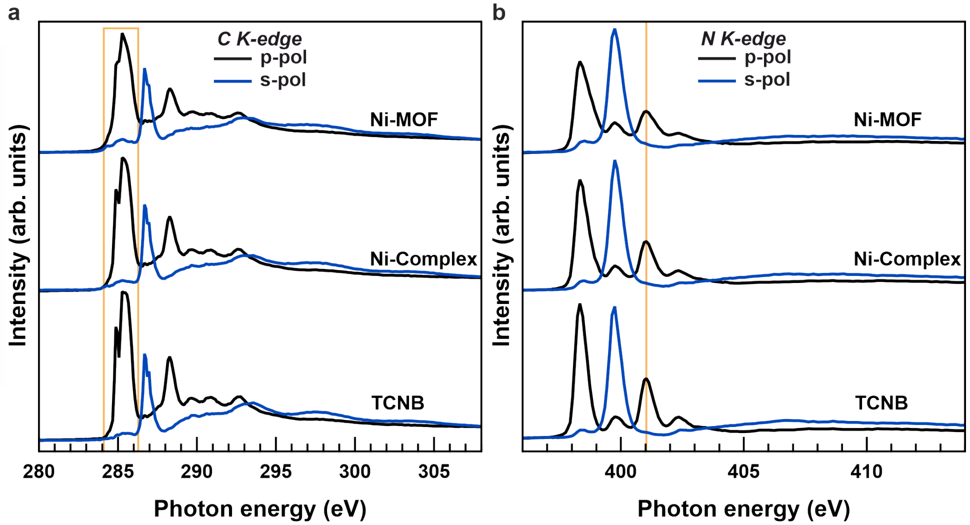

Figure 5.3: NEXAFS spectra acquired across the **(a)** C and **(b)** N *K*-edge for all phases of interest. Adapted from [41].

TCNB CN groups can accordingly be concluded. In all (metal-)organic phases, the orientations of the benzene ring and CN groups are the same. Besides this geometric insight, the NEXAFS spectra reveal details on the electronic structure of the adsorbed TCNB units. Specifically, with an increasing Ni amount, the relative intensities of the π^*-resonances compared σ^*-resonances are reduced. Remember that the TCNB density per nm^2 does not change for all (metal-)organic layers. Accordingly, the constant intensity of the σ^*-resonances clearly indicates that the Ni-induced structural adaptions do not result in an increased charge transfer from the substrate. Instead, the quenching of π^*-resonances suggests a dominant π-symmetric Ni to TCNB bonding.[174] The intensity reduction involves resonances characteristic of both the benzene and CN constituents, implying a mixing of Ni states with the entire molecular TCNB system.

In order to identify the predominant structure when applying space-averaging techniques, we have used a similar approach for our NEXAFS/XPS and valence band spectroscopy datasets. Starting from a saturated TCNB layer, subsequent deposition of Ni has been monitored by combined XPS and NEXAFS. The corresponding N 1*s* photoelectron spectra are displayed in figure 5.4a. The deposition rate of Ni has been held constant, with the total Ni amounts included for each step. When changing the experimental setup, the necessary Ni deposition times are subject to variation for many reasons like the different sample to evaporator distances. Therefore, only the relative amounts need to be considered when comparing results obtained through different characterization methods. Embedding Ni (60 s total deposition) into the pristine TCNB layer results in the broadening of the N 1*s* signal, which continues after doubling the Ni amount (120 s total deposition). Further increasing the total Ni deposition time to 300 s does not result in a different spectral line shape anymore, but only in an overall shift (≈ 0.2 eV) of the entire spectrum towards higher binding energies. In addition, the NEXAFS spectra acquired across the Ni L_3-edge for all the Ni amounts are depicted in figure 5.4b, with a reference for Ni clusters obtained after Ni (120 s) deposition onto bare Au(111) included as well. The spectra corresponding to 60 s and 120 s total Ni deposition times resemble the same spectral line shape and strong linear dichroism, as the transitions only occur when using s-polarized light. In contrast to that, the Ni cluster reference on Au(111) is characterized by transitions that are evident for both polarizations, which agrees well with an increase in the coordination number within the clusters. In comparison to the asymmetric bonding environment of Ni sites surrounded by four CN groups in the metal-organic phases, the bonding in Ni clusters is more spherically symmetric and the observed linear dichroism is consequently suppressed.[175] Once the free coordination groups provided by the molecular layer are saturated the excess of deposited Ni should result in the formation of Ni clusters. Indeed, the spectrum corresponding to a total Ni deposition time of 300 s is characterized by an overall shift of the main resonance, apparent when using s-polarized light. Furthermore, transitions are also evident for p-polarized light. It appears that an excess of Ni is present so that the spectra of CN-coordinated Ni and Ni clusters add up. This is in perfect agreement with the N 1*s* spectra as, after a total Ni deposition of 120 s, the chemical change observed by XPS occurred quantitatively. Further adding Ni (300 s total deposition time) results in the formation of clusters that simply dope the fully converted Ni-MOF phase and explain the shift of the spectrum without any changes in the spectral shape as a consequence of doping.

Our STM-based findings indicate that the transitions from the TCNB to the Ni-Complex and to the Ni-MOF occur gradually. Therefore, we conclude that half of the amount necessary to obtain the fully reacted Ni-MOF phase represents the condition where the Ni-Complex phase predominantly contributes to the observed signal, even when using space-averaging methods. Defining the conditions based on linear dichroism using NEXAFS and the chemical changes observed by XPS allows concluding the main presence of the Ni-Complex and Ni-MOF after the total Ni deposition times of 60 s and 120 s, respectively. We note that the N 1*s* spectra qualitatively display that for pristine TCNB there is only one N species present and constituted by a main line and satellite components causing peak asymmetry. After adding Ni, the broadening of the spectrum indicates the presence of two inequivalent N environments as the N species coordinating to Ni arises at a higher binding energy compared to the one characteristic of the non-interacting N species, characterized by a reduced intensity with respect to the parent TCNB layer. Indeed, the spectra qualitatively exhibit the expected ratios, i.e. 1:3 (Ni-Complex predominant after a total Ni deposition of 60 s) and 1:1 (Ni-MOF present after a total Ni deposition of 120 s). A precise quantification based on peak fitting, however, would be speculative. This is due to the fact that the ratio of satellite to main line components, as well as their relative positions, may vary for the different structural adaptions depending on the Ni amount and CN groups interacting with Ni and not.[176] Furthermore, photoelectron diffraction effects may have an impact on the relative intensities.[177] This is why, for the NEXAFS/XPS data, we have used the calibration approach elaborated above. The NEXAFS spectra recorded across the Ni L_3-edge in figure 5.4b do not suggest any appreciable difference in the Ni coordination environment nor oxidation state for the different Ni(TCNB)$_\mathrm{x}$ phases on Au(111). The main line at a photon energy of ≈ 852.2 eV and

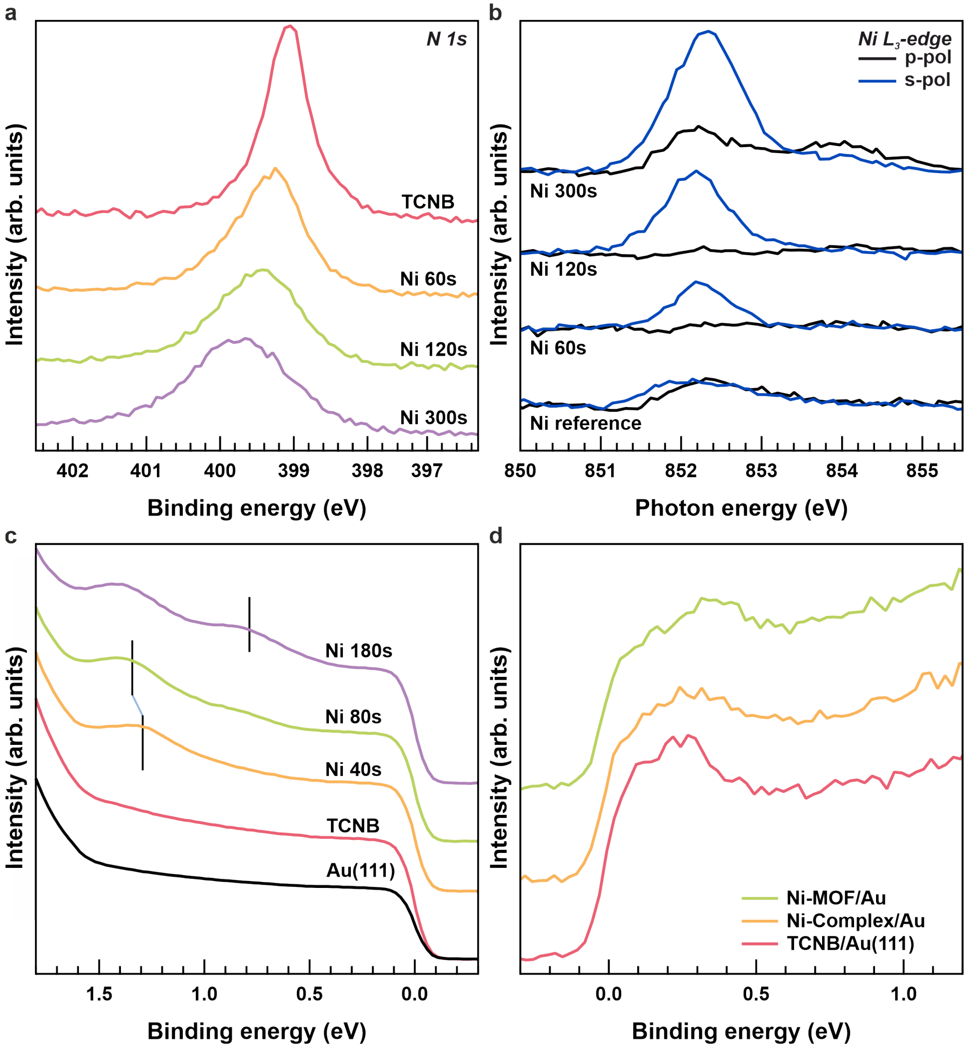

Figure 5.4: **(a)** N 1*s* photoelectron spectra recorded at $h\nu = 515$ eV (p-polarization) in normal emission after subsequently depositing Ni onto the pristine TCNB layer. **(b)** NEXAFS spectra acquired across the Ni L_3-edge for different absolute Ni amounts together with a Ni reference on Au(111). **(c)** Valence band spectra acquired at $h\nu = 30$ eV (p-polarization) for pristine Au(111), a saturated TCNB layer as well as after subsequent deposition of Ni. Note that the Au(111) reference spectrum has been divided by a factor of four to compensate for the strong intensity of the bare substrate. **(d)** Intensity versus binding energy line profiles obtained at $\overline{\Gamma}$ for the different (metal-)organic phases on Au(111). As provided for [41].

the strong linear dichroism are a strong evidence for Ni(I) in a quadratic planar coordination environment in both the Ni-Complex and Ni-MOF on Au(111), as observed for similar systems.[45]

The angle-integrated valence band spectra of bare Au(111), a saturated TCNB layer on Au(111) before and after gradually depositing Ni are presented in figure 5.4c. Again, the total Ni amounts are indicated and it has to be noted that they are different due to the different setups used for characterization. Deposition of Ni (40 s) onto the pristine TCNB/Au(111) interface results in an additional peak that arises at a binding energy of ≈ 1.30 eV. After doubling the Ni amount the peak is shifted around 50 meV towards lower binding energies. Additionally, a small signal at a binding energy of ≈ 0.80 eV becomes evident. This peak grows further upon increasing the total Ni deposition time to 180 s while there are no changes observed in the main peak apparent after a total Ni deposition time of 80 s. We conclude that the extra peak at a binding energy of ≈ 0.80 eV evidences the formation of Ni clusters after completion of the Ni-MOF layer, as this state is not characterized by a defined signature in *k*-space. As such, total Ni deposition times of 40 s and 80 s correspond to the main presence of the Ni-Complex and Ni-MOF, respectively.

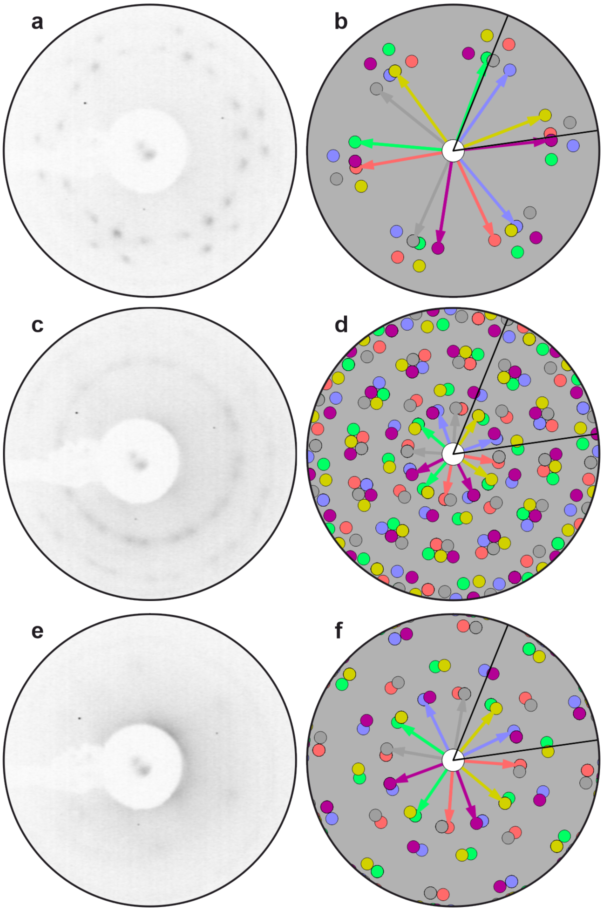

Figure 5.5: LEED patterns recorded at an incident beam energy of 20 eV for the (metal-)organic phases of interest on Au(111): **(a)** TCNB; **(c)** Ni-Complex; **(e)** Ni-MOF. The substrate orientation is indicated by the black lines in the LEED patterns simulated based on the unit cells and orientation found via STM for: **(b)** TCNB; **(d)** Ni-Complex; **(f)** Ni-MOF. As provided for [41].

The control over the (metal-)organic phase probed through space-averaging methods can be further confirmed via LEED experiments, which have been conducted for the specimens prepared for valence band spectroscopy. The LEED patterns observed after the deposition of TCNB on Au(111) and after depositing Ni for 40 s and 80 s are displayed in figure 5.5. The Ni deposition amounts correspond to the predominant occurrence of the Ni-Complex and Ni-MOF, respectively. For all displayed LEED patterns, simulations that account for the unit cell sizes, their orientation with respect to the supporting specimen as well as symmetry-equivalent domains are also included. The main contribution of one phase to the diffraction patterns is clearly evident.

The hierarchical nature of the self-assembly process and the Au(111) herringbone reconstruction, evident in the STM images after stabilizing the (metal-)organic overlayers, has been used for defining the relative orientation between the unit cells of the respective (metal-)organic phase and the substrate. This is depicted in figure 5.6a for the parent TCNB/Au(111) interface. The bright stripes caused by the herringbone reconstruction (orange) are always orthogonal to one of the ideal Au(111) primitive lattice vectors (black) of the unreconstructed supporting surface. The primitive lattice vector direction corresponds to the $\overline{\Gamma}$-$\overline{\mathrm{K}}$ direction of the substrate in k-space along which the incidence plane of the photon is oriented during valence band spectroscopy experiments (see later).[178,179] Consequently, the orientation of all phases of interest for LEED simulations and with respect to the light incidence plane in valence band spectroscopy experiments have been defined. In figure 5.5b, c, the thereby observed TCNB to Ni-Complex and Ni-Complex to Ni-MOF transitions are displayed. Note that the TCNB unit cell orientation found in figure 5.5b is rotated but symmetry-equivalent to the one in figure 5.5a. The same argument applies to the Ni-MOF orientation evident in figure 5.5c when compared to the one presented in figure 5.1c. Eventually, figure 5.5d represents a model of the orientation the metal-organic structures have with respect to the photon incidence plane in valence band spectroscopy experiments. The structural models are enlarged for better visibility. Angles of $\approx 22°$ and $\approx -28°$ for these two Ni-Complex and Ni-MOF domains with respect to the photon incidence plane arise accordingly. A value of 45° has to be subtracted from the orientation of the Ni-Complex unit cell to get the orientation of the coordinated Ni sites in our adapted frame. This yields an angle of $\approx -23°$ for the Ni-Complex in comparison with $\approx -28°$ for the Ni-MOF.

Intrigued by the STM/STS and NEXAFS/XPS findings, we have examined the Ni-TCNB interaction more deeply by analyzing the angle-integrated photoemission intensity in the valence band region from the Fermi level to a binding energy of 1.80 eV. The valence band spectra of Au(111) and the (metal-)organic phases under investigation have been defined previously (see figure 5.4c). Depositing TCNB on Au(111) leads to no apparent molecule-related features in the considered binding energy range. Note, however, that at a binding energy of ≈ 1.50 eV the d-bands of the substrate start to dominate the spectrum and, therefore, do not allow a characterization of any MOs of TCNB beyond that binding energy. Supported by our density functional theory (DFT) calculations below, we expect the photoemission signature related to the TCNB HOMO in this energy region. In contrast, upon the formation of the Ni-Complex, a clear peak at a binding energy of ≈ 1.30 eV appears, which is shifted 50 meV towards higher binding energies after forming the Ni-MOF. These observations support the emergence of a new metal-organic

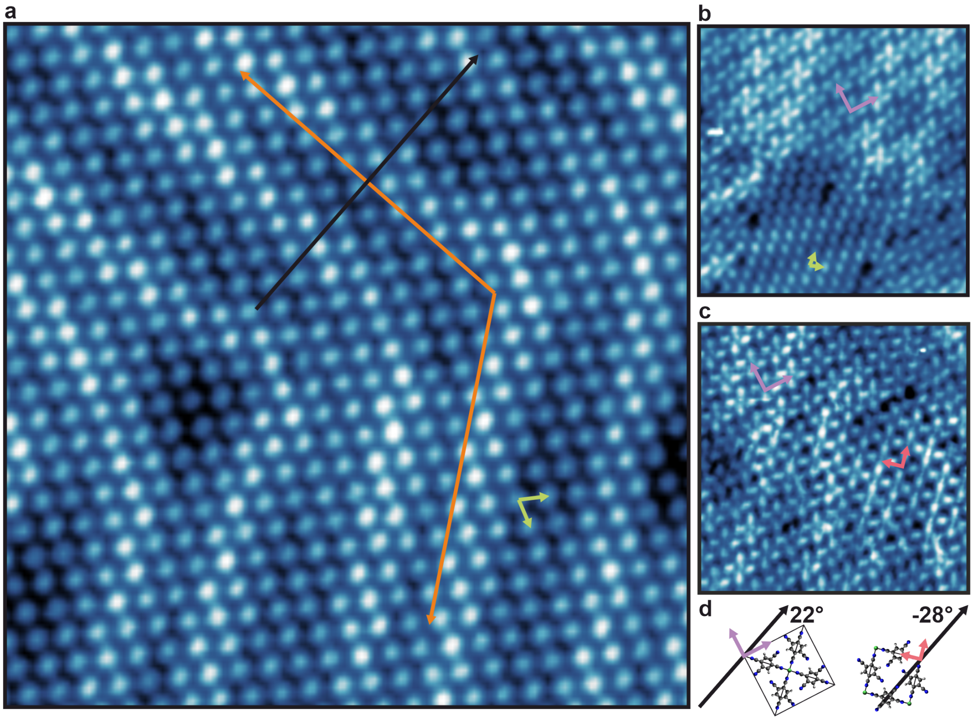

Figure 5.6: **(a)** STM image ($18.2 \cdot 18.2$ nm^2) corresponding to as-deposited TCNB on Au(111) with the herringbone stripes of the supporting reconstructed substrate and the direction along $\overline{\Gamma}$-$\overline{\mathrm{K}}$ of the substrate in k-space indicated in orange and black, respectively. **(b)** STM image ($14.5 \cdot 14.5$ nm^2) of a TCNB to Ni-Complex boundary. **(c)** STM image ($14.5 \cdot 14.5$ nm^2) of a Ni-Complex to Ni-MOF boundary. The tunneling parameters have been: **(a)** $V = 350$ mV, $I = 50$ pA; **(b)** $V = 300$ mV, $I = 30$ pA; **(c)** $V = 300$ V, $I = 20$ pA. **(d)** Orientation of the metal-organic phases under investigation with respect to the $\overline{\Gamma}$-$\overline{\mathrm{K}}$ direction of the substrate in k-space. As provided for [41].

hybrid state upon creating the Ni-organic complex and framework. Furthermore, the change in binding energy evidences a qualitative difference between the isolated Ni-Complex and the extended Ni-MOF. At this point, we turn to our DFT calculations for comprehensive interpretation. The calculation details are summarized in chapter A.2. Based on the experimentally determined structural information from STM and NEXAFS, we have constructed structural models of all phases and employed DFT to compute their energy level alignment. Given the weak interaction with the surface and to put a focus on the new Ni-TCNB hybrid states, in a first step, all layers are treated as freestanding. The density of states projected (pDOS) onto the Ni $3d$ and the TCNB $2p_z$ states for the three systems are shown in figure 5.7a. Comparing the pristine TCNB phase to the Ni-Complex and Ni-MOF, the states with strong Ni $3d$-character are located in the binding energy region between the $2p_z$-based HOMO and LUMO of TCNB. Indeed, besides the expected Ni states, the calculations reveal a considerable contribution of TCNB $2p_z$ states at the same energies, suggesting a hybridization between the metal center and the TCNB ligands. Upon closer inspection (zoomed region in figure 5.7a), we find that the TCNB $2p_z$ states primarily hybridize with the Ni $3d_{\mathrm{xz/yz}}$-levels. Moreover, our theoretical data predicts a notable energy broadening for these states when going from the molecular Ni-Complex to the extended Ni-MOF (see also band structure plots in figure 5.7b, c). This is further illustrated by the partial charge density of both the Ni-Complex and Ni-MOF in the binding energy window of 1.45-1.55 eV and 1.27-1.37 eV, presented in figure 5.7d. Such a broadening is also predicted for former TCNB LUMO/HOMO-based states of $2p_{\mathrm{z}}$-character with Ni $3d_{\mathrm{xz/yz}}$-contributions.

To unambiguously identify the nature of the Ni $3d$-based hybrid states, we employ POT, which links constant binding energy photoelectron $k_{||}$ distribution maps with the Fourier transform of the states they originate from.[58,59] Comparing measured and simulated constant binding energy $k_{||}$-maps, then allows for interpreting valence band data in terms of molecular states. Using our synchrotron-installed k-PEEM, we have measured complete $k_{||}$-maps for $k_{||} < 2.2$ Å^{-1} across the presented binding energy range, leading to a three-dimensional intensity (k_{x}, k_{y}; E_{B}) data cube. The photoelectron $k_{||}$ distributions at the peak maxima in figure 5.4c are displayed for bare Au(111), Ni-Complex and Ni-MOF in figure 5.8 (top). A precise definition of the orientation of the metal-organic structures with respect to the light incidence direction is possible from the features of Au(111) (figure 5.8a), still evident with adsorbed overlayers. The orientation found via STM can be implemented accordingly,[178,179] further accounting for symmetry-equivalent orientations, whose Brillouin zones are highlighted in the simulated emission patterns in the top panel of figure 5.8b, c. Upon forming the Ni(TCNB)$_{\mathrm{x}}$ phases, an additional ring-like feature ($k_{||}$-diameter ≈ 1.5 Å^{-1}) emerges. By comparing with the simulated $k_{||}$-map, we find excellent agreement at a binding energy of 1.45 eV for the Ni-Complex, where the hybridization of Ni $3d_{\mathrm{xz/yz}}$ and ligand $2p_{\mathrm{z}}$ states is strong, providing unambiguous evidence for the coordinative interaction between Ni and TCNB. Considering the experimental binding energy shift between the Ni-Complex and the Ni-MOF, we display the simulated $k_{||}$-map for the Ni-MOF at a binding energy of 1.50 eV. The similar orientation of the coordinated Ni sites found via STM explains (see figure 5.6) the similar shape of the $k_{||}$-maps of the Ni-Complex and the Ni-MOF, likewise indicated by our theoretical data. The Ni-MOF related emission should become sharper as a consequence of the emerging extended π-conjugation. However, an appreciation of this effect solely on the $k_{||}$-maps is difficult. The evident substrate features have been used to obtain $k_{||}$ distributions precisely along the same directions in k-space. In the bottom panel of figure 5.8 band maps, obtained through vertically cutting through our three-dimensional data cube along $\overline{\mathrm{K}}$-$\overline{\Gamma}$-$\overline{\mathrm{M}}$ of the substrate, are displayed for clean Au(111) as well as Ni(TCNB)$_{\mathrm{x}}$/Au and compared to the calculated band maps. Considering the shift between experiment and theory, the electronic level of the isolated Ni-Complex can be clearly spotted (star) while the interconnected Ni-MOF exhibits signatures of a sizeable energy-dispersive electronic band structure (arrow).

These findings are also remarkable from a different perspective. In all previous angle-resolved photoemission works, it has not been possible to detect emission features, which are that strongly related to $3d$-orbitals of the metal center. For most transition metal complexes, the photocurrent related to $3d$-based states either occurs at $k_{||}$ outside the experimental range or is easily mistaken as weakly intense background. Both cases are clear when relating the calculated pDOS in figure 5.7a to the features in our simulated band maps in figure 5.8c for Ni-MOF. There is no signature of the Ni $3d_{\mathrm{x}^2-\mathrm{y}^2/\mathrm{xy}}$-based states expected at binding energy of ≈ 0.95 eV. As evident from figure 5.7a these states mix with the TCNB $2p_{\mathrm{x,y}}$-states and are of σ-character, making them experimentally not accessible.[180] Notably, these localized states are not broadened in their energy width upon the formation of the extended Ni-MOF structure. The Ni $3d_{\mathrm{z}^2}$-based DOS at a binding energy of ≈ 1.35 eV in figure 5.7a is expressed as a flat line in figure 5.8c. There is no experimental observation of these emission features, attributed to the missing contribution of TCNB $2p$ states to these levels. Notably, the unit cell of the Ni-MOF is mainly organic-based so that the intensity of its Ni $3d$-based hybrid states emission features increases with significant ligand $2p$ contribution. Furthermore, the binding energy of the $3d$-based states usually strongly overlaps with the highly intense substrate d-bands as, for instance, found for metalloporphyrins, which are POT prototype compounds.[45] Indeed, the π-symmetric hybridization of Ni $3d_{\mathrm{xz/yz}}$ states and TCNB $2p_{\mathrm{z}}$-based states is the important prerequisite that enables the observation of the electronic features here. In both metal-organic structures our theory suggests occupied states close to the Fermi level. These former TCNB LUMO-based states become occupied at the expense of Ni $3d_{\mathrm{x}^2-\mathrm{y}^2}$-based states, characterized by an unpaired electron. This implies a Ni(I) configuration for both the Ni-Complex and Ni-MOF as strongly supported by the NEXAFS data in figure 5.4b. However, there is no experimental evidence of the occupation of these TCNB LUMO-based states from our valence band data. In general, the interaction with the surface results in an altered energy level alignment and may determine the occupation of the TCNB LUMO-based states here. From the behavior of the Au(111) surface state evident for all (metal-)organic phases of interest (see figure 5.4d) it appears likely that the charge donated from the Ni atoms to the molecular linkers is actually redistributed to the Au(111) surface. Consequently, the Ni(I) oxidation state is observed while the TCNB LUMO-based states become unoccupied. In figure 5.4d, intensity versus binding energy line profiles that cross the bottom of the Shockley surface state at $\overline{\Gamma}$ are displayed for all (metal-)organic phases of interest. Though hard to quantify due to the poor signal-to-noise ratio, a qualitative downshift of the surface state feature is evident. This supports the charge transfer from the metal-organic phases to the supporting Au(111) surface at the expense of the TCNB LUMO-based states, predicted as partially occupied for the calculated freestanding structures.[181] Given the good agreement between experimental features and gas-phase simulations found for the Ni $3d$-based metal-organic hybrid states characteristic of $\mathrm{Ni(TCNB)_x}$ structures on Au(111) and the difficult theoretical description of the Au(111) surface reconstruction, we wanted to investigate the impact of more strongly interacting surfaces. According to literature, the structural motifs of various transition metal TCNB combinations are insensitive to the underlying support.[163,182–184] This allows us to focus on tuning the electronic properties via charge transfer at more reactive surfaces while including the supporting substrate,[45] as elaborated in the following chapter.

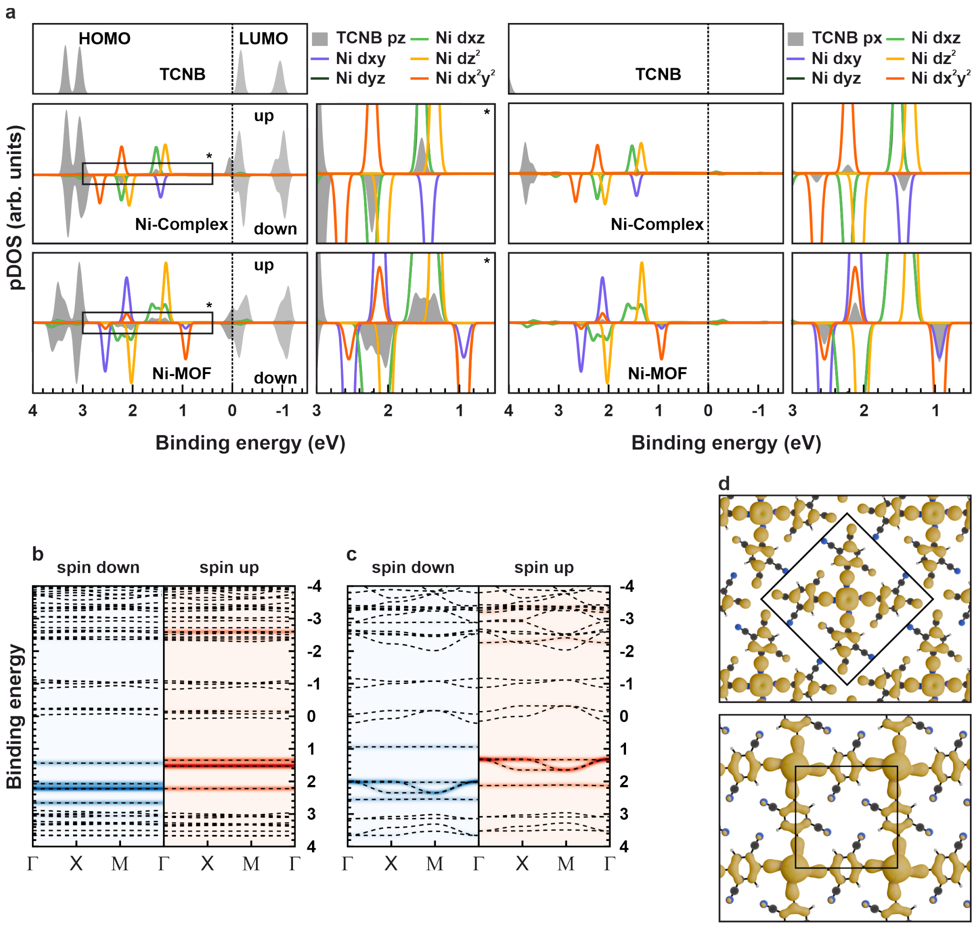

Figure 5.7: **(a)** Calculated DOS projected onto Ni 3*d* and TCNB $2p_z$ states for all freestanding structures under consideration. Note the identical Ni $3d_{xz/yz}$ pDOS. Calculated band structures for freestanding: **(b)** Ni-Complex; **(c)** Ni-MOF. **(d)** Partial charge density (spin-up) in the binding energy window of 1.45-1.55 eV and 1.27-1.37 eV for the Ni-Complex (top) and the Ni-MOF (bottom). Adapted from [41].

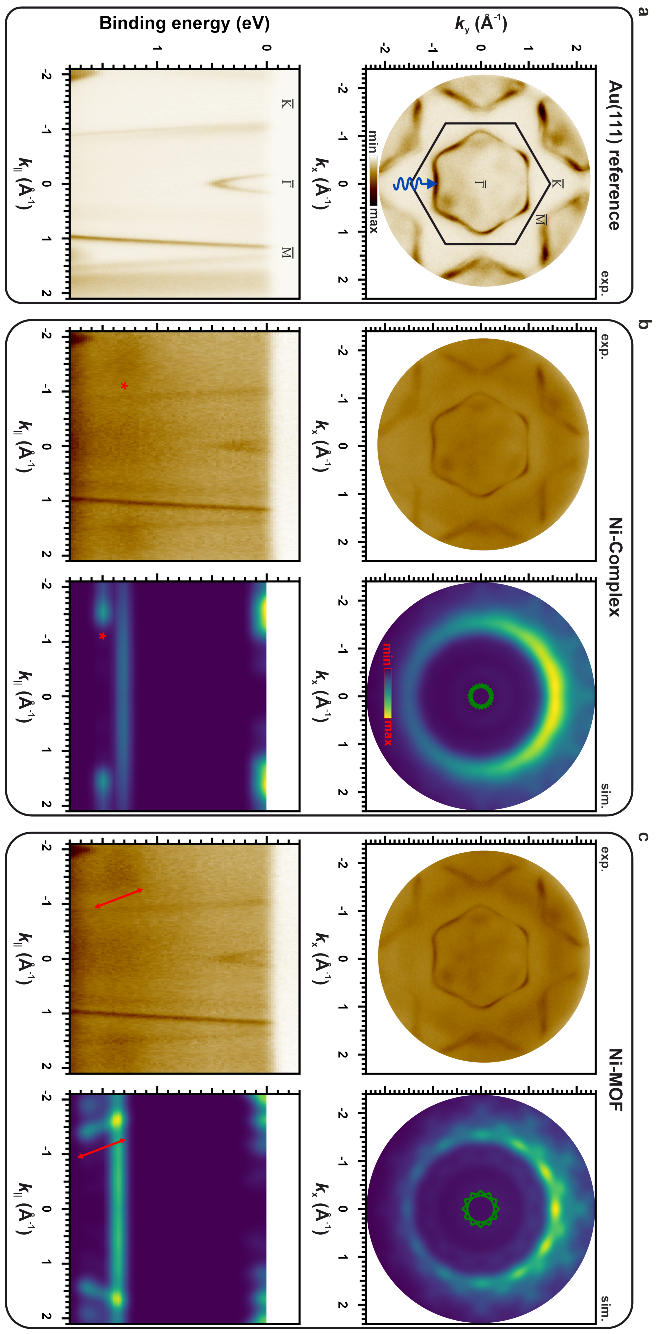

Figure 5.8: Top: Experimental constant binding energy $k_{\|}$-maps obtained for: **(a)** clean Au(111); **(b)** Ni-Complex/Au; **(c)** Ni-MOF/Au. The binding energy has been around: **(a, b)** 1.30 eV; **(c)** 1.35 eV. Simulated constant binding energy $k_{\|}$-maps for freestanding Ni-Complex and Ni-MOF are included in **(b)** and **(c)** for a binding energy of: **(b)** 1.45 eV; **(c)** 1.50 eV. Bottom: Band maps along $\overline{K}$-$\overline{\Gamma}$-$\overline{M}$ of the substrate measured for: **(a)** Au(111); **(b)** Ni-Complex/Au; **(c)** Ni-MOF/Au. Simulated band maps for freestanding Ni-Complex and Ni-MOF are included in **(b)** and **(c)**. All data have been collected at $h\nu = 30$ eV (p-polarization). As provided for [41].

5.3 Direct Metal-Organic Framework Formation on 1,2,4,5-Tetracyanobenzene/Ag(100)

In figure 5.9a, two subsequently acquired STM images characteristic of a saturated layer of as-deposited TCNB on Ag(100) are presented. During STM imaging on the pristine layer the molecular arrangement is observed to be affected. The first images still exhibit a regular pattern of alternating molecular tetramers. Afterwards, the regularity of the tetramer pattern decreases. Nevertheless, the distance between the tetramer centers does not change. It appears that two tetramer configurations can be easily switched by the STM tip at low biases ($V \approx 100$ mV). A different behavior has been reported for 7,7,8,8-tetracyanoquinodimethane (TCNQ) on Ag(100).[185] The side length of the square, which connects adjacent tetramer centers, has been determined from the STM images as ≈ 1.65 nm. When considering the orientation of the square with respect to the primitive Ag(100) lattice vector, which is along the bulk [110] direction, there is good agreement with identical points on the surface for commensurate (3, 5; 5, -3) square sides. This gives a calculated square length of ≈ 1.69 nm based on the ≈ 2.89 Å surface unit cell of Ag(100), in reasonable agreement with the one determined from STM measurments and the experimental error range.[186] Thus, we assume a superstructure commensurate with the supporting Ag(100) substrate where the edges of the square are positioned on top sites of the surface, as further justified in the following. The calculated square is included in the structural model for the pristine TCNB layer presented on the right side of figure 5.9b. The structural model has been stepwise elaborated based on the BRSTM image (figure 5.9b, top left) and the high-resolution topographic STM image (figure 5.9b, bottom left), acquired using a CO-functionalized tip. The position and orientation of benzene rings in the TCNB molecules are resolved (orange hexagon) in the BRSTM image. Thereby, the tetramer configuration remained constant without switching the regular pattern of alternating dark and bright tetramers upon acquisition of the BRSTM image. It is also evident that the adjacent TCNB molecules within one tetramer are orthogonal to each other. This makes them chiral, while the different tetramers possess opposite chirality. The intermolecular distance is constant for all neighboring molecules, including those from opposing tetramers. Squares with a side length of three times the lattice constant of the supporting Ag(100), which are rotated by 45° with respect to the surface unit cell, connect the molecular centers of tetrameric units. In this way, a clock arrangement of the molecular squares is realized, as highlighted in the structural model in figure 5.9b. A similar arrangement is known for Ni atoms that rearrange when a carbide overlayer is formed on the Ni(111) surface, resulting in a maximized interaction between C and Ni.[187] It appears that the TCNB units arrange in a similar fashion here, as all the centers of the squares connecting the molecular centers are located above the same sites on the supporting Ag(100) surface. From combined insights gained by valence band spectroscopy and NEXAFS, which are elaborated in the following, we know that all TCNB molecules adsorb flat on the surface without strong distortion and that there are two different TCNB units. One is experiencing charge transfer from the substrate, and the other not, while the angle of the identical molecular mirror axes with respect to the bulk [100] direction is $|7|°$ and 0°, respectively. Consequently, the different tetramer configurations can be explained by CN groups, which slightly point towards the tetramer center or not, as neighboring molecules within are orthogonal to each other. Assuming

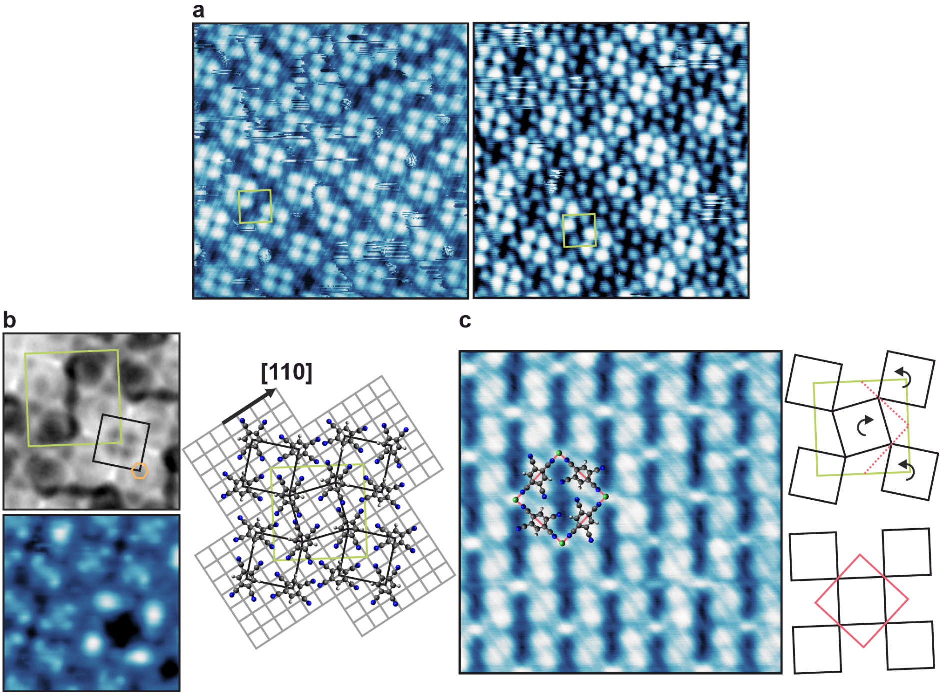

Figure 5.9: (a) Two STM images ($14.6 \cdot 14.6$ nm^2) acquired for the pristine TCNB layer on Ag(100) showing a switching behavior, triggered by electron tunneling. Left: $V = 20$ mV and $I = 50$ pA; right: $V = 100$ mV and $I = 10$ pA. **(b)** Top left: BRSTM image ($3.0 \cdot 3.0$ nm^2, $V = 100$ mV and $I = 10$ pA with a voltage modulation of 20 mV at 759 Hz) of TCNB on Ag(100). Bottom left: high-resolution STM image acquired with a CO-functionalized tip ($3.0 \cdot 3.0$ nm^2, $V = 20$ mV and $I = 50$ pA) of TCNB on Ag(100). Right: a structural model of TCNB on Ag(100). **(c)** Left: high-resolution STM image acquired with a CO-functionalized tip ($5.9 \cdot 5.9$ nm^2, $V = 40$ mV and $I = 50$ pA) of the Ni-MOF on Ag(100). Right: a model showing the metal-organic structure formation. Partially adapted from [41].

the tetramer center to be a top site, a coordinative interaction with reconstructed Ag atoms could explain this peculiar molecular arrangement. There are various reports on CN groups of organic linker groups that distort their supporting substrate through the coordination of surface atoms.[159,188–192] The different appearance of the two tetramers can be further confirmed when looking at the topographic STM image in figure 5.9b, acquired with a CO-functionalized tip. The two tetramer configurations differ in the sense that for one configuration the CN groups point more towards the tetramer center. A closer inspection of the BRSTM image presented in figure 5.9b supports this conclusion. We have implemented this in the structural model where the orthogonal TCNB molecules are aligned with the [100] bulk direction of the supporting surface within the dark tetramers. In the bright tetramers, the TCNB units are $|7|°$ rotated with respect to that. This configuration seems to represent the ideal compromise between the anchoring effect of Ag atoms and the repulsion between the CN groups of molecules in neighboring tetramers. We note that it has been reported that the lone pairs of CN groups do not directly point towards stabilized metal centers bigger than those of the 3*d* series.[167] A different situation is expected with a directional bond character for Ni atoms deposited onto the pristine TCNB layer. The Ni-MOF structure, directly observed after Ni evaporation, is further included on the left side of figure 5.9c. From the STM image, acquired with a CO-functionalized tip, a good agreement is found for the same unit cell as for the Ni-MOF structure formed at the Au(111) surface. The orientation with respect to the Ag(100) surface agrees well with the diagonals of the squares, connecting the tetramer centers within the pristine TCNB/Ag(100) interface. There seems to be a relation between the centers of the square sides of the tetramer lattice of the parent molecular layer and the positions of the Ni centers in the Ni-MOF structure formed. As such, the calculated lattice parameter of ≈ 1.19 nm for the (4, -1; 1, 4) commensurate Ni-MOF is within the estimated error range. With the directional character of the Ni-TCNB bond, the intrusion of Ni atoms as guests into the pristine TCNB layer releases the strain of the clock structure, while the intermolecular distance does not change. This is sketched on the right side of figure 5.9c. The hollow sites that appear for the embedded Ni centers have been implemented in the theoretical description of the Ni-MOF structure (see below).

The different appearance of TCNB molecules in the STM images can be further understood when looking at the XPS data characteristic of the pristine TCNB/Ag(100) interface. In contrast to the case on Au(111), there are two peaks evident in the N 1*s* XPS spectrum presented in figure 5.10a. There is a peak with the main line at a binding energy of ≈ 398.4 eV, as well as one shifted ≈ 1.6 eV towards higher binding energies. A splitting in the N 1*s* spectrum similar to the one observed here has been reported for simultaneously present charged and uncharged TCNQ molecules.[193] This strongly supports that the observed STM contrast is due to assemblies of practically equivalently oriented molecules, experiencing charge transfer from the supporting substrate or not. From the alternating tetramer pattern, a 1:1 ratio in the N 1*s* peak ratio of the two TCNB species is expected. This is qualitatively evident in the XPS spectrum, considering the fact that photoelectron diffraction effects, again, may have an impact on the peak ratio.[177]

The shape of the N 1*s* spectrum changes drastically upon deposition of Ni onto the TCNB/Ag(100) interface, resulting in the formation of the Ni-MOF. There are two evident regions that agree with a main line component and a satellite tail at higher binding energies. In comparison to the as-deposited structure the main line feature is broadened. As for the case on Au(111), this agrees with two distinct N environments, attributed to CN groups stabilizing Ni centers via coordinate bonds and CN groups which are not coordinating. We note that the satellite structure may be subject to variation when changing the supporting surface.[194,195] Therefore, additionally to photoelectron diffraction effects the spectrum may be influenced by this effect, rationalizing the differences to the N 1*s* spectrum characteristic of the Ni-MOF on Au(111) in figure 5.4a. For the realized preparation conditions, the NEXAFS spectra collected across the Ni L_3-edge are characterized by strong linear dichroism, as evident from figure 5.10b. There is an absorption line at a photon energy of ≈ 852.2 eV that is only observed when using s-polarized light. Equal to the metal-organic structures on Au(111) (figure 5.4b), this is a strong evidence for the Ni(I) oxidation state.[45,131] Our theoretical findings are in accordance with that, indicating no impact on the Ni

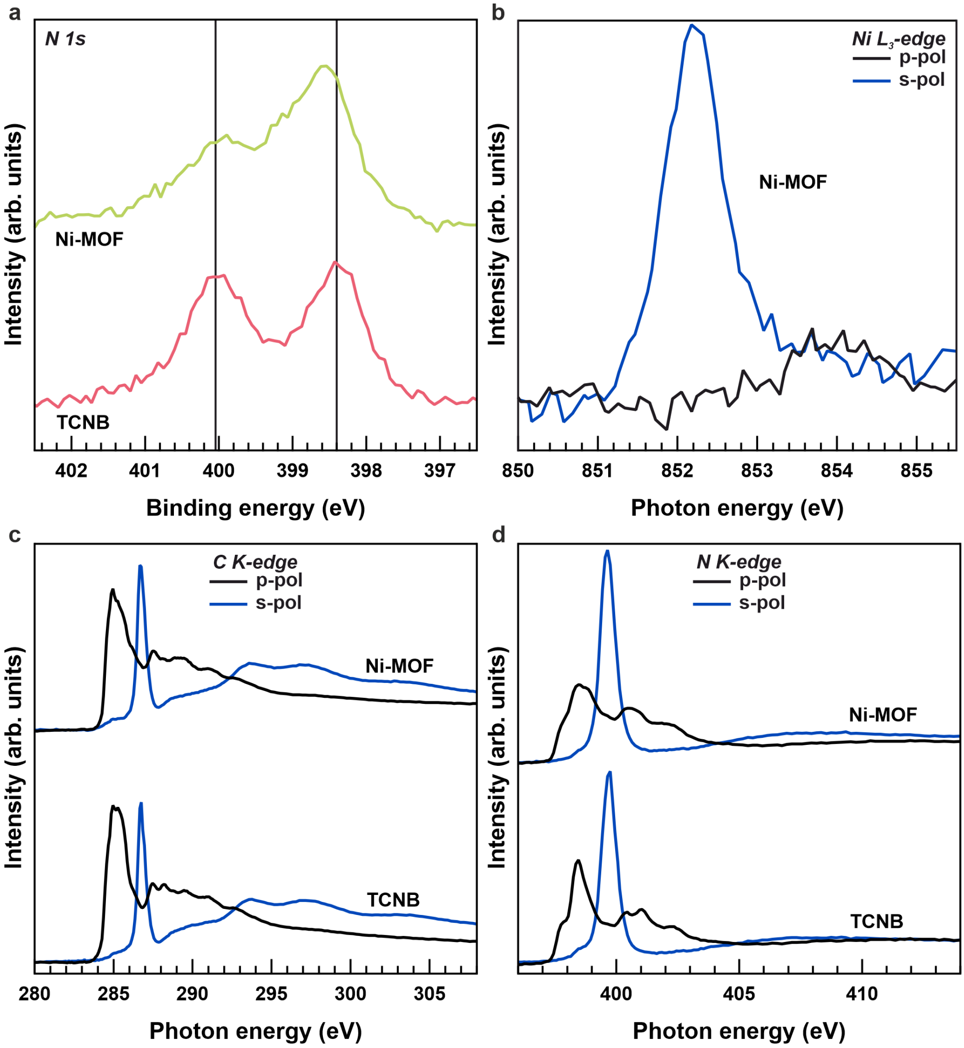

Figure 5.10: **(a)** N 1*s* photoelectron spectra recorded for pristine TCNB and Ni-MOF on Ag(100). The spectra have been collected at $h\nu = 515$ eV (p-polarization). **(b)** NEXAFS spectra obtained across the Ni L_3-edge after Ni-MOF formation. NEXAFS spectra obtained across the **(c)** C and **(d)** N *K*-edge for pristine TCNB and Ni-MOF on Ag(100). Partially adapted from [41].

oxidation state when considering the freestanding Ni-MOF structure and the one stabilized on Ag(100). There is an additional small and weakly dichroic contribution at a photon energy of ≈ 854.0 eV. We attribute this component to additional Ni clusters, forming as a consequence of the slight excess of the Ni amount necessary for the quantitative Ni-MOF formation.

The NEXAFS spectra comparing the pristine TCNB layer and the Ni-MOF on Ag(100) obtained across the C and N *K*-edge are presented in figure 5.10c, d. We note that the structural changes induced by the deposition of Ni onto the TCNB/Ag(100) interface are quite considerable. Firstly, two different TCNB species are converted into a single one. Secondly, this single TCNB species stabilized within the Ni-MOF layer is influenced by the interaction with Ni. It is not possible to disentangle both effects. However, the important information is that both the spectra of the parent TCNB and the Ni-MOF layer are characterized by resonances, exclusively present for only one of the linear polarizations used. It is therefore possible to conclude that neither the differently charged TCNB units in the templating interface are tilted or distorted nor the TCNB units linking the Ni sites in the Ni-MOF.[65] The flat on-surface orientation of the TCNB molecules is conserved throughout the structural adaption upon deposition of Ni onto the templating TCNB/Ag(100) interface.

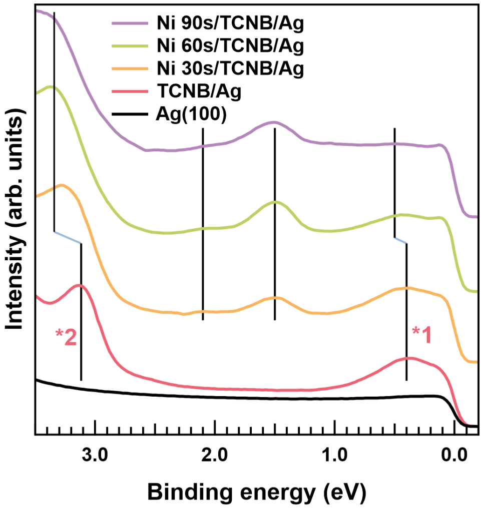

Figure 5.11: Valence band spectra recorded at $h\nu = 30$ eV (p-polarization) for clean Ag(100), a saturated TCNB layer, as well as after subsequent deposition of Ni with the total Ni deposition times indicated. Note that the Ag(100) reference spectrum has been divided by a factor of four to compensate for the strong intensity of the bare substrate. Adapted from [41].

A series of valence band spectra obtained for clean Ag(100), a saturated layer of TCNB on Ag(100) and after subsequent deposition of Ni onto the organic layer is presented in figure 5.11. Note that the spectrum of the clean Ag(100) surface has been divided by a factor of four for better visibility. The pristine TCNB/Ag(100) interface exhibits two peaks at binding energies of around 0.40 eV and 3.10 eV. Within the POT approach, the constant binding energy momentum maps obtained from adsorbed organic molecules can be related to the Fourier transform of their gas-phase MOs (figure 5.12).[58,59] TCNB units rotated 90° with respect to each other are included in the theoretical momentum maps on the square substrate due to their symmetry-equivalence. STM data indicate that these symmetry-equivalent molecular orientations within the two tetramers differ from each other by a slight rotation of the TCNB molecules with respect to the bulk [100] direction. Azimuthal angle differences with respect to the experimental photon incidence plane along the bulk [100] direction can be simulated and distinguished experimentally, if the

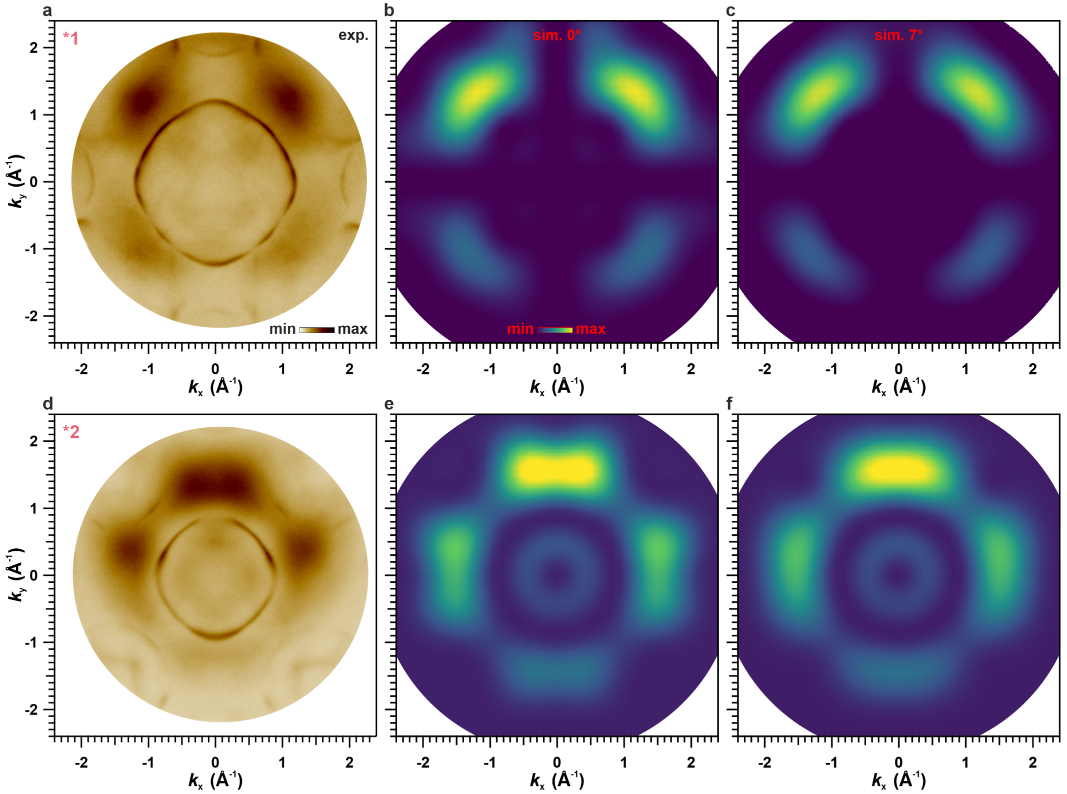

Figure 5.12: **(a)** Experimental momentum map obtained for TCNB/Ag(100) at a binding energy of around 0.40 eV. Simulations of the photoelectron $k_{||}$-distributions based on the gas-phase LUMO of TCNB used within the POT approach are also displayed for TCNB orientations with respect to the photon plane of incidence of: **(b)** 0°; **(c)** $|7|°$. **(d)** Experimental momentum map obtained for TCNB/Ag(100) at a binding energy of around 3.10 eV. Simulations of the photoelectron $k_{||}$-distributions based on the gas-phase HOMO of TCNB used within the POT approach are also displayed for TCNB orientations with respect to the photon plane of incidence of: **(e)** 0°; **(f)** $|7|°$. All data have been collected at $h\nu = 30$ eV (p-polarization).

photoemission patterns of the MOs of the adsorbed TCNB molecules in different tetramers do not overlap. As such, it appears that the momentum map at a binding energy of ≈ 0.40 eV is best simulated by the gas-phase TCNB LUMO. This indicates that there is charge transfer to the molecule from the supporting substrate. The momentum map at a binding energy of ≈ 3.10 eV is best simulated by the gas-phase TCNB HOMO. However, the simulated momentum maps agree best with the experimental ones for azimuthal orientations with respect to the light plane of incidence of 0° (HOMO) and |7|° (LUMO), respectively. This further confirms that there are two TCNB configurations that differ by the azimuthal angle with respect to the supporting Ag(100) surface, differently interacting with the supporting surface. The one rotated by |7|° with respect to the bulk [100] direction is experiencing charge transfer as expressed as LUMO emission, while the one not rotated is uncharged. Differently interacting molecular units that coexist within molecular overlayers on metallic substrates have already been identified based on the POT approach.[196] Thereby, the variation of the relative MO energy level alignment for distinctly charged molecules has already been addressed. This does not allow to characterize MOs via POT at higher binding energies as the HOMO of the uncharged TCNB units, due to the strong contribution of the arising Ag substrate *d*-bands overlapping with these features.

The valence band spectra upon subsequent deposition of Ni onto the pristine TCNB layer on Ag(100) in figure 5.11 allow for similar conclusions as observed on Au(111). After a Ni deposition time of 30 s two additional peaks at binding energies of ≈ 1.50 eV and ≈ 2.10 eV start to appear. At the same time the HOMO and LUMO features evident in the spectrum of the parent TCNB/Ag(100) interface start to shift towards higher binding energies. When doubling the Ni amount (60 s total deposition time) the signal of the new states increases and the shift of the HOMO and LUMO proceeds further. After a Ni deposition time of 90 s the intensity of the new state does not increase further. Neither the shift of the HOMO and LUMO features continues. Instead, there is an additional signal appearing between the LUMO feature and the new state at a binding energy of ≈ 1.50 eV. This additional signal has no notable texture in *k*-space and indicates the formation of Ni clusters due to the quantitative Ni-MOF formation after a total Ni deposition time of 60 s.

Further evidence on the direct formation of the Ni-MOF upon deposition of Ni onto the pristine TCNB layer on Ag(100) has been obtained by LEED. In figure 5.13 the experimental LEED patterns of the tetramer structure and Ni-MOF are well reproduced by the theoretical ones, constructed based on the overlayer matrices described above. Again, the substrate direction (black line) and symmetry-equivalent domains (colored lines) are included.

The observed similarity of the Ni-MOF structures on Au(111) and Ag(100) is supported by similar findings indicating that the structural motifs of various transition metal TCNB combinations are insensitive to the underlying support.[86,161,163,183,184] Therefore, we have the opportunity to explore the impact of a more strongly interacting surface and to focus on tuning the electronic properties of 2D-MOFs via charge transfer from the more reactive Ag(100) substrate.[45] A comparison of structural model overlayered to an STM image to the calculated structure (see chapter A.2) is presented in figure 5.14. When considering the impact of the Ag surface on the electronic structure

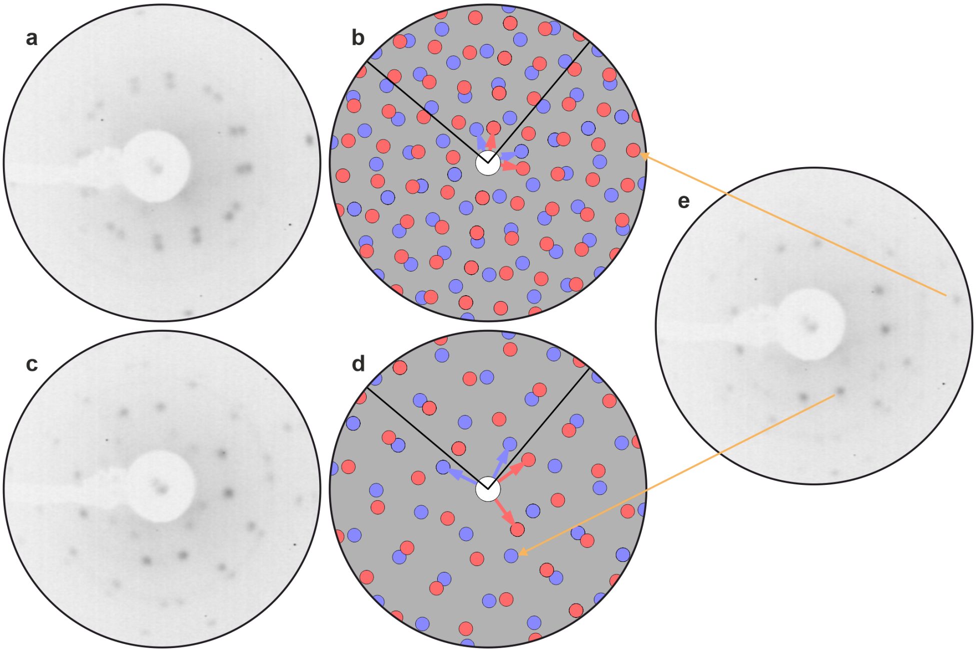

Figure 5.13: LEED patterns recorded at an incident beam energy of 20 eV for: **(a)** TCNB and **(c)** Ni-MOF on Ag(100). **(b)**; **(d)** LEED patterns simulated from the commensurate overlayers characteristic of: TCNB; Ni-MOF. The substrate orientation is indicated by the black lines. **(e)** Demonstration of the direct TCNB to Ni-MOF transition for a not fully converted TCNB/Ag(100) interface with the orange arrows indicating the coexistence of TCNB and Ni-MOF patches. As provided for [41].

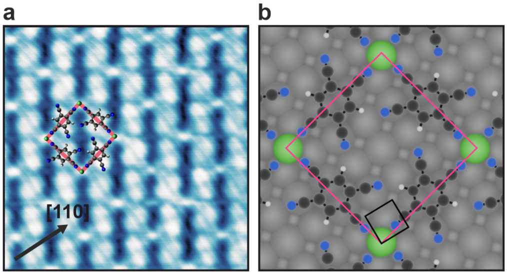

Figure 5.14: **(a)** High-resolution STM image ($5.9 \cdot 5.9$ nm^2, $V = 40$ mV and $I = 50$ pA) of the Ni-MOF on Ag(100), acquired with a CO-functionalized tip. **(b)** Relaxed structure of the Ni-MOF/Ag(100) interface. Adapted from [41].

of the Ni-MOF via modelling the full interface including the substrate, we find only negligible differences in the molecular arrangement compared to the freestanding Ni-MOF. Given the similar structures, an energy-dispersive behavior of the electronic levels for Ni-MOF/Ag(100) is expected, as indicated by the calculated DOS and band structure of the interface projected onto the TCNB $2p_z$ and Ni $3d$-states (figure 5.15a). In comparison to the pDOS of the freestanding Ni-MOF (figure 5.7a), the energy level alignment of the Ni $3d$-states is indeed only slightly affected by the Ag substrate. Our theory predicts the Ni(I) oxidation state as is confirmed experimentally (figure 5.10b). The stronger interaction with Ag, however, leads to overall larger band dispersions of the Ni-MOF states, as can be seen from the band structure plot in figure 5.15a (dashed lines), where the Ni 3*d* (green) and the TCNB $2p_\mathrm{z}$ (purple) orbital character is indicated. To highlight the similarity to the freestanding Ni-MOF, we illustrate the partial charge density in the binding energy window of 1.95-2.05 eV in figure 5.15b. We clearly observe the same hybridization between Ni $3d_\mathrm{xz/yz}$ and TCNB $2p_\mathrm{z}$ states. Interestingly, our simulations suggest the experimental appearance of the TCNB LUMO-based band due to charge transfer from the Ag surface, proving that the metal-organic nanostructures can be tuned via charge transfer at the interface while simultaneously retaining their π-conjugating properties. To test the theoretical predictions, we have measured the valence band spectra of Ag(100) and Ni-MOF/Ag(100) (figure 5.15c). Compared to the uncovered Ag surface (black line), four prominent features arise and are indicated by vertical bars at binding energies of $\approx$ 0.50 eV, 1.50 eV, 2.10 eV and 3.30 eV. Their experimental binding energies are in good agreement with the states of the Ni-MOF, shown in the pDOS in figure 5.15b. Thus, we assign the features in the valence band spectrum to a TCNB LUMO-based band contributing to intensity maxima at the Fermi level and at a binding energy of $\approx$ 0.50 eV, Ni 3*d*-based states (1.50 eV, 2.10 eV) and a TCNB HOMO-based band (3.30 eV). The fact that more Ni-MOF related emissions can be identified on Ag compared to Au is simply a result of the deeper lying onset of the Ag *d*-bands ($\approx$ 3.00 eV versus 1.50 eV for Au).

Focusing on the Ni 3*d*-based hybrid states, we show experimental $k_{||}$-maps (binding energy of $\approx$ 1.40 eV) for Ag(100) and Ni-MOF/Ag(100) in the top panels of figure 5.16a, b. The Ag(100) reference image also includes the surface Brillouin zone of the substrate and the experimental geometry. As can be seen from the comparison of figure 5.16a with b, the emissions within the Ag(100) Brillouin zone are solely due to the substrate. Analogous to the measurements on Au(111), we observe the feature of the hybrid state at $k_{||}$-values $\approx$ 1.5 Å, however, with a richer substructure owing to fewer rotational domains on the Ag(100). These emission features of the hybrid state are excellently reproduced in our simulated momentum map, depicted in figure 5.16b for a binding energy of 1.55 eV. Note that the intensities arising from Ag *sp*-bands inside the Brillouin zone are not correctly accounted for in our five layer slab calculations and are therefore greyed out in the corresponding simulated momentum map. In order to analyze the band dispersion of the Ni 3*d*-based hybrid states, we compare band maps for Ag(100) and Ni-MOF/Ag(100) in the bottom panel of figure 5.16a, b. Focusing on the binding energy region around 1.40 eV, the band dispersion of the hybrid states becomes evident, both, in the experimental as well as in the simulated band maps, thereby unambiguously proving the 2D extended nature of the metal organic network. It is also worth noting that, compared to the band maps of the Ni-MOF on Au(111) (figure 5.8c), the band characteristic on Ag(100) is more clearly visible, presumably again due to the fewer rotational domains. Furthermore, the binding energy regions around the TCNB HOMO and LUMO-based bands are also well reproduced. The differences in the LUMO-based features between the single-molecule TCNB layer and the extended Ni-MOF are evident from the band maps along $\overline{\mathrm{M}}$-$\overline{\Gamma}$-$\overline{\mathrm{X}}$ of the substrate for Ag(100), TCNB/Ag(100) and after formation of the Ni-MOF, which are

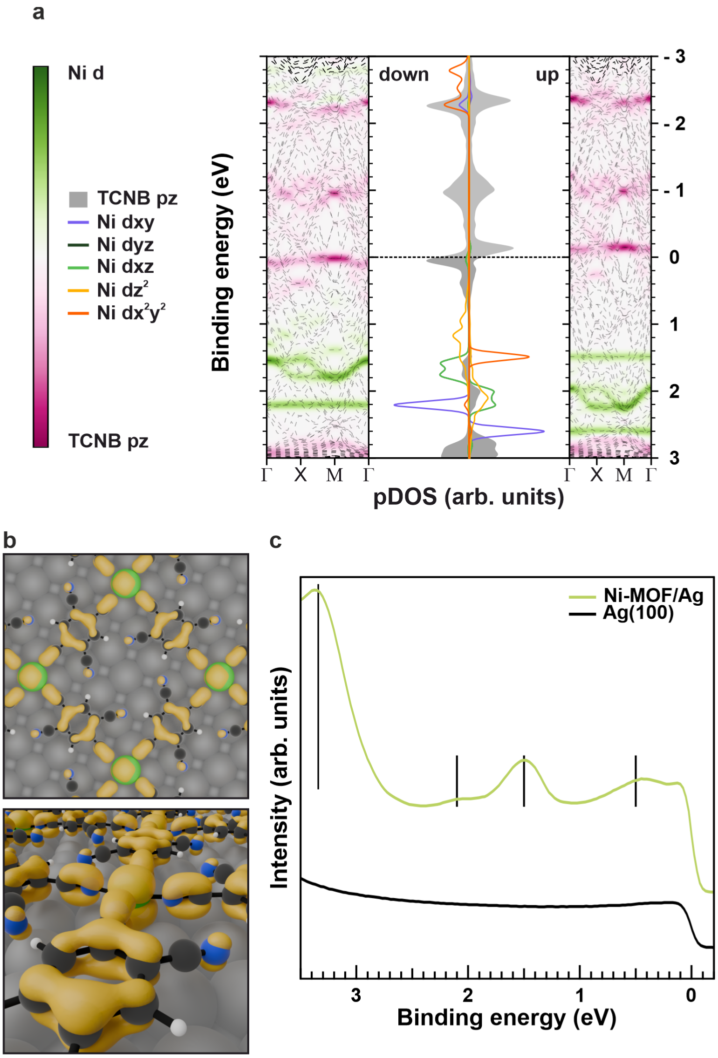

Figure 5.15: **(a)** Calculated DOS and band structure projected onto Ni 3d and TCNB 2p_z states for Ni-MOF/Ag(100). Note the identical Ni 3$d_{xz/yz}$ pDOS. **(b)** Top and side views of the partial charge density (spin-up) in the binding energy window of 1.95-2.05 eV for Ni-MOF/Ag(100). **(c)** Valence band spectra of Ag(100) and Ni-MOF/Ag(100). Note that the Ag(100) reference spectrum has been divided by a factor of four to compensate for the strong intensity of the bare substrate. All data have been obtained at $h\nu = 30$ eV (p-polarization). Adapted from [41].

compared in figure 5.17. When depositing TCNB on Ag(100), the molecule-related signal is best observed by the LUMO feature at a binding energy of ≈ 0.40 eV, corresponding to the TCNB species experiencing charge transfer at the interface. As known for strong hybridization with the supporting surface, the momentum maps can be reasonably described by momentum maps simulated from gas-phase orbitals, but the states exhibit an energy-dispersive texture in

k-space.[197] After Ni deposition the effect of creating an π-extended 2D structure, expressed by a broadening in energy as well as a sharpening of the former TCNB LUMO-related states, can still be appreciated. In the binding energy region of the TCNB HOMO-based band the substrate d-bands start to dominate the spectrum, limiting the obtainable information.

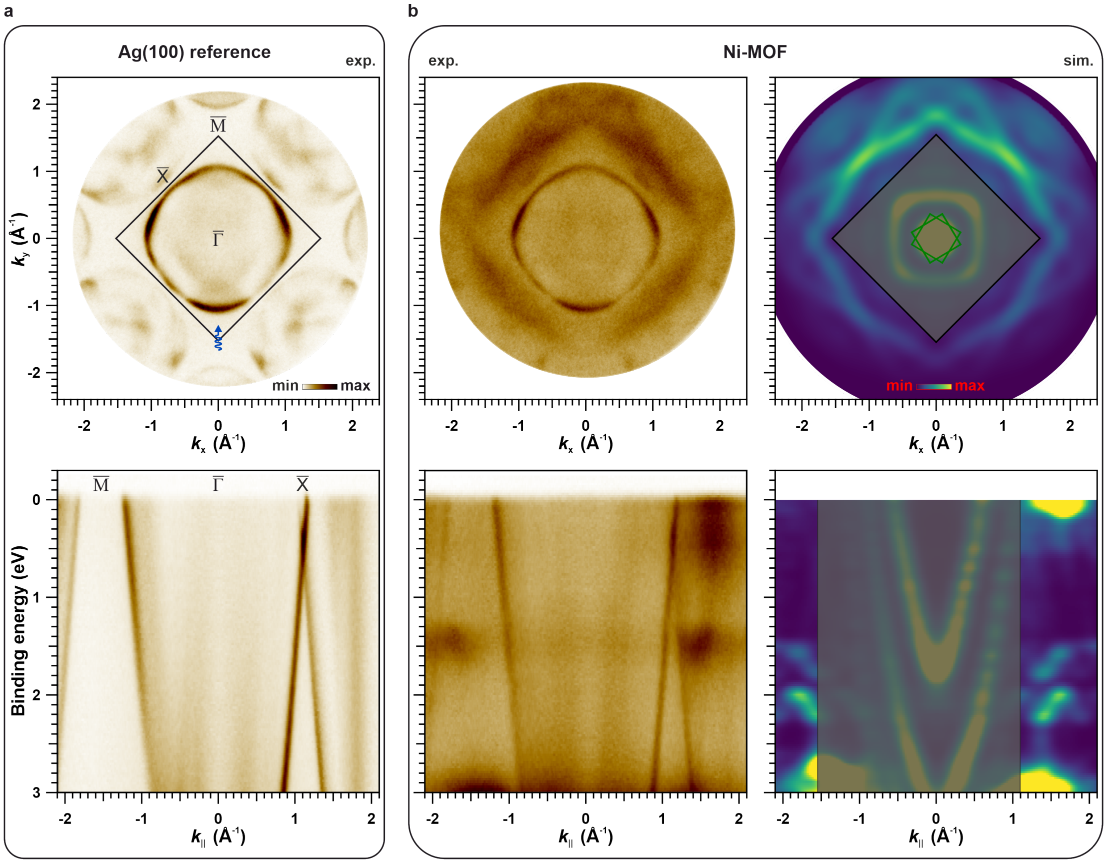

Figure 5.16: Top: Experimental constant binding energy (≈ 1.4 eV) momentum maps for: **(a)** Ag(100); **(b)** Ni-MOF/Ag(100). A simulated constant binding energy (= 1.55 eV) momentum map for Ni-MOF/Ag is included in **(b)**. Bottom: Band maps along $\overline{\mathrm{M}}$-$\overline{\Gamma}$-$\overline{\mathrm{X}}$ of the substrate for: **(a)** Ag(100); **(b)** Ni-MOF/Ag(100). A simulated band map for Ni-MOF/Ag(100) is included in **(b)**. All data have been collected at $h\nu = 30$ eV (p-polarization). As provided for [41].

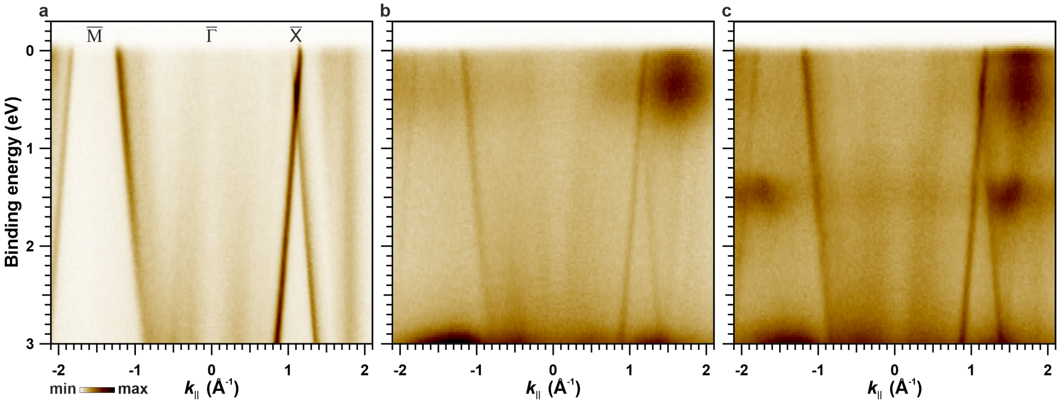

Figure 5.17: Band maps along $\overline{\text{M}}$-$\overline{\Gamma}$-$\overline{\text{X}}$ of the substrate characteristic of: **(a)** Ag(100); **(b)** pristine TCNB/Ag(100); **(c)** Ni-MOF/Ag(100). All data have been collected at $h\nu = 30$ eV (p-polarization). As provided for [41].

6 Conclusion and Outlook

Following the on-surface chemistry approach, the functional properties of a 2D NiTPP-based polymer have been adressed in chapter 4. Covalently linking individual molecular units facilitates the formation of a π-conjugated aromatic nanomesh that exhibits dispersive electronic states and, at the same time, is stable up to very high temperatures. Insights obtained from a multi-technique approach revealed that the single-active site functionality of Ni incorporated in the porphyrin coordination pocket is preserved and remains unaltered upon polymerization. The polymeric nanostructures can be tuned by charge transfer at the interface, similar to their single-molecule counterparts. The increased structural robustness, consequence of the creation of a conjugated system, introduces a certain rigidity to the molecular network since the molecular units are interconnected. This allows tuning of the frontier electronic structure, as expressed by different magnetic properties when activating molecular magnetism on the Cu(111) surface. Surprisingly, perfectly ordered nanomeshes are not required for a defined Ni ion functionality from a spectroscopic perspective.

The reactivity of the Ni centers characteristic of porphyrin networks created on all surfaces during this work has been tested towards the axial ligands CO, NO_2 and pyrazine. Thereby, no interaction has been observed. On-surface stabilized and cyclodehydrogenated TM porphyrins have been demonstrated to exhibit a reactivity different to their parent compounds due to their reduced structural flexibility.[126,153,198] Given the enhanced rigidity characteristic of TM-containing polymers, we envision an additional parameter in the control of the specificity of the interaction with axial ligands, imparting tailoring their reactivity.

The calculations performed for the NiTPP-based network predict an broading in energy for the π-symmetric Ni $3d$-based states upon polymerization. To get further insights representative of the π-conjugation in extended TM-containing 2D metal-organic nanostructures we have realized the formation of a Ni-TCNB MOF in chapter 5. Well-ordered nanostructures mimicking the coordination pocket of NiTPP are observed, thereby making Ni $3d$-based states available within valence band spectroscopy measurements. This has allowed us to confirm the emergence of energy-dispersive Ni $3d$-based states upon the hierarchical self-assembly from Ni-TCNB complexes to the extended Ni-TCNB MOF on Au(111). Finally, we have demonstrated that the electronic structure of the 2D-MOF can be tuned via charge transfer from a more reactive Ag(100) substrate, where the Ni-TCNB MOF is formed in controlled fashion. These findings may serve as a case study and can be applied to various coordination polymers, thereby paving the way towards a better band structure engineering in 2D-MOFs. We also highlight the differences in the electronic levels characteristic of the organic backbones in extended TM-containing polymers and 2D-MOFs. When directly linking the organic units by covalent bonds to create NiTPP-based networks, the observed bandwidth is much wider.

Upon our approach to realize similar Ni coordination environments while tuning the energy level alignment of the characteristic Ni 3*d*-based states we have extended the POT approach, previously only applied to organic-based molecular levels. This is particularly interesting for understanding the reactivity of TM centers stabilized within 2D-MOFs towards axial ligands. The active center formed upon relevant catalytic conversion reactions might be tracked with *k*-resolution. At this point, we further note that 2D-MOFs similar to our Ni-TCNB MOF have been constructed on substrates passivated by graphene.[199] For TM porphyrin/phtalocyanine layers magnetic order has been observed upon stabilization on graphene-passivated ferromagnetic substrates.[200–202] Spin-resolved *k*-PEEM experiments,[203] where we envision reaching a precision down to the level of molecular states derived from TM 3*d* orbitals, appear highly relevant to identify the levels mediating the coupling at the interface.

References

[1] Bartels, L. *Nat. Chem.* **2010**, *2*, 87–95.

[2] Elemans, J. A. A. W.; Lei, S.; De Feyter, S. *Angew. Chem. Int. Ed.* **2009**, *48*, 7298–7332.

[3] Wang, A.; Li, J.; Zhang, T. *Nat. Rev. Chem.* **2018**, *2*, 65–81.

[4] Paolesse, R.; Nardis, S.; Monti, D.; Stefanelli, M.; Di Natale, C. *Chem. Rev.* **2017**, *117*, 2517–2583.

[5] Khajetoorians, A. A.; Wiebe, J.; Chilian, B.; Wiesendanger, R. *Science* **2011**, *332*, 1062–1064.

[6] Gutzler, R.; Stepanow, S.; Grumelli, D.; Lingenfelder, M.; Kern, K. *Acc. Chem. Res.* **2015**, *48*, 2132–2139.

[7] Ballav, N.; Wäckerlin, C.; Siewert, D.; Oppeneer, P. M.; Jung, T. A. *J. Phys. Chem. Lett.* **2013**, *4*, 2303–2311.

[8] Wende, H. et al. *Nat. Mater.* **2007**, *6*, 516–520.

[9] Auwärter, W.; Écija, D.; Klappenberger, F.; Barth, J. V. *Nat. Chem.* **2015**, *7*, 105–120.

[10] Gottfried, J. M. *Surf. Sci. Rep.* **2015**, *70*, 259–379.

[11] Grill, L.; Dyer, M.; Lafferentz, L.; Persson, M.; Peters, M. V.; Hecht, S. *Nat. Nanotechnol.* **2007**, *2*, 687–691.

[12] Côté, A. P.; Benin, A. I.; Ockwig, N. W.; O'Keeffe, M.; Matzger, A. J.; Yaghi, O. M. *Science* **2005**, *310*, 1166–1170.

[13] Tsuda, A.; Osuka, A. *Science* **2001**, *293*, 79–82.

[14] Nitzan, A.; Ratner, M. A. *Science* **2003**, *300*, 1384–1389.

[15] Grill, L.; Hecht, S. *Nat. Chem.* **2020**, *12*, 115–130.

[16] Lin, S.; Diercks, C. S.; Zhang, Y.-B.; Kornienko, N.; Nichols, E. M.; Zhao, Y.; Paris, A. R.; Kim, D.; Yang, P.; Yaghi, O. M.; Chang, C. J. *Science* **2015**, *349*, 1208–1213.

[17] Marianov, A. N.; Kochubei, A. S.; Gu, S.; Jiang, Y. *ACS Catal.* **2022**, *12*, 8610–8622.

[18] Krasnikov, S. A.; Doyle, C. M.; Sergeeva, N. N.; Preobrajenski, A. B.; Vinogradov, N. A.; Sergeeva, Y. N.; Zakharov, A. A.; Senge, M. O.; Cafolla, A. A. *Nano Res.* **2011**, *4*, 376–384.

[19] Barth, J. V.; Costantini, G.; Kern, K. *Nature* **2005**, *437*, 671–679.

[20] Barth, J. V. *Annu. Rev. Phys. Chem.* **2007**, *58*, 375–407.

[21] Grumelli, D.; Wurster, B.; Stepanow, S.; Kern, K. *Nat. Commun.* **2013**, *4*, 1–6.

[22] Dong, R.; Pfeffermann, M.; Liang, H.; Zheng, Z.; Zhu, X.; Zhang, J.; Feng, X. *Angew. Chem. Int. Ed.* **2015**, *54*, 12058–12063.

[23] Santhini, V. M.; Wäckerlin, C.; Cahlík, A.; Ondráček, M.; Pascal, S.; Matěj, A.; Stetsovych, O.; Mutombo, P.; Lazar, P.; Siri, O.; Jelínek, P. *Angew. Chem. Int. Ed.* **2021**, *60*, 439–445.

[24] Liu, J.; Abel, M.; Lin, N. *J. Phys. Chem. Lett.* **2022**, *13*, 1356–1365.

[25] Liu, J.; Lin, N. *ChemPlusChem* **2023**, *88*, e202200359.

[26] Huang, X.; Sheng, P.; Tu, Z.; Zhang, F.; Wang, J.; Geng, H.; Zou, Y.; Di, C.-a.; Yi, Y.; Sun, Y.; Xu, W.; Zhu, D. *Nat. Commun.* **2015**, *6*, 1–8.

[27] Huang, X.; Zhang, S.; Liu, L.; Yu, L.; Chen, G.; Xu, W.; Zhu, D. *Angew. Chem.* **2018**, *130*, 152–156.

[28] Dong, R.; Zhang, Z.; Tranca, D. C.; Zhou, S.; Wang, M.; Adler, P.; Liao, Z.; Liu, F.; Sun, Y.; Shi, W.; Zhang, Z.; Zschech, E.; Mannsfeld, S. C. B.; Felser, C.; Feng, X. *Nat. Commun.* **2018**, *9*, 1–9.

[29] Wang, Z. F.; Liu, Z.; Liu, F. *Nat. Commun.* **2013**, *4*, 1–5.

[30] Wang, Z. F.; Su, N.; Liu, F. *Nano Lett.* **2013**, *13*, 2842–2845.

[31] Dong, L.; Kim, Y.; Er, D.; Rappe, A. M.; Shenoy, V. B. *Phys. Rev. Lett.* **2016**, *116*, 096601.

[32] Zhang, L. Z.; Wang, Z. F.; Huang, B.; Cui, B.; Wang, Z.; Du, S. X.; Gao, H.-J.; Liu, F. *Nano Lett.* **2016**, *16*, 2072–2075.

[33] Sun, H.; Tan, S.; Feng, M.; Zhao, J.; Petek, H. *J. Phys. Chem. C* **2018**, *122*, 18659–18668.

[34] Kumar, A.; Banerjee, K.; Foster, A. S.; Liljeroth, P. *Nano Lett.* **2018**, *18*, 5596–5602.

[35] Zhang, R.; Liu, J.; Gao, Y.; Hua, M.; Xia, B.; Knecht, P.; Papageorgiou, A. C.; Reichert, J.; Barth, J. V.; Xu, H.; Huang, L.; Lin, N. *Angew. Chem. Int. Ed.* **2020**, *59*, 2669–2673.

[36] Hernández-López, L.; Piquero-Zulaica, I.; Downing, C. A.; Piantek, M.; Fujii, J.; Serrate, D.; Ortega, J. E.; Bartolomé, F.; Lobo-Checa, J. *Nanoscale* **2021**, *13*, 5216–5223.

[37] Kraus, S.; Herman, A.; Huttmann, F.; Bianchi, M.; Stan, R.-M.; Holt, A. J.; Tsukamoto, S.; Rothenbach, N.; Ollefs, K.; Dreiser, J.; Bischof, K.; Wende, H.; Hofmann, P.; Atodiresei, N.; Michely, T. *J. Phys. Chem. C* **2022**, *126*, 3140–3150.

[38] Frezza, F.; Schiller, F.; Cahlík, A.; Ortega, J. E.; Barth, J. V.; Arnau, A.; Blanco-Rey, M.; Jelínek, P.; Corso, M.; Piquero-Zulaica, I. *Nanoscale* **2023**, *15*, 2285–2291.

[39] Baranowski, D.; Cojocariu, I.; Sala, A.; Africh, C.; Comelli, G.; Schio, L.; Tormen, M.; Floreano, L.; Feyer, V.; Schneider, C. M. *Angew. Chem. Int. Ed.* **2022**, *61*, e202210326.

[40] Baranowski, D.; Cojocariu, I.; Schio, L.; Gutiérrez Bolaños, C.; Floreano, L.; Dreiser, J.; Carlotto, S.; Casarin, M.; Feyer, V.; Schneider, C. M. *Adv. Mater. Interfaces* **2024**, 2400123.

[41] Baranowski, D.; Thaler, M.; Brandstetter, D.; Windischbacher, A.; Cojocariu, I.; Mearini, S.; Chesnyak, V.; Schio, L.; Floreano, L.; Gutiérrez Bolaños, C.; Puschnig, P.; Patera, L. L.; Feyer, V.; Schneider, C. M. *Submitted to ACS Nano* **2024**.

[42] Ishii, H.; Sugiyama, K.; Ito, E.; Seki, K. *Adv. Mater.* **1999**, *11*, 605–625.

[43] Willenbockel, M.; Lüftner, D.; Stadtmüller, B.; Koller, G.; Kumpf, C.; Soubatch, S.; Puschnig, P.; Ramsey, M. G.; Tautz, F. S. *Phys. Chem. Chem. Phys.* **2015**, *17*, 1530–1548.

[44] Hwang, J.; Wan, A.; Kahn, A. *Materials Science and Engineering: R: Reports* **2009**, *64*, 1–31.

[45] Sturmeit, H. M. et al. *Small* **2021**, *17*, 2104779.

[46] Kahn, O., *Molecular Magnetism*; VCH: 1993.

[47] Hieringer, W.; Flechtner, K.; Kretschmann, A.; Seufert, K.; Auwärter, W.; Barth, J. V.; Görling, A.; Steinrück, H.-P.; Gottfried, J. M. *J. Am. Chem. Soc.* **2011**, *133*, 6206–6222.

[48] Hüfner, S., *Photoelectron Spectroscopy*; Springer: 2003.

[49] Stöhr, J., *The Nature of X-Rays and Their Interactions with Matter*; Springer: 2023.

[50] Hollander, J. M.; Shirley, D. A. *Science* **1981**, *214*, 629–631.

[51] Berglund, C. N.; Spicer, W. E. *Phys. Rev.* **1964**, *136*, A1030–A1044.

[52] Seah, M. P.; Dench, W. A. *Surf. Interface Anal.* **1979**, *1*, 2–11.

[53] Briggs, D.; Seah, M. P., *Practical Surface Analysis by Auger and X-ray Photoelectron Spectroscopy*; Wiley: 1983.

[54] Ertl, G.; Küppers, D., *Low energy electrons and surface chemistry*; VCH: 1985.

[55] Pendry, J. B. *Surf. Sci.* **1976**, *57*, 679–705.

[56] Schattke, W. *Prog. Surf. Sci.* **1997**, *54*, 211–227.

[57] Minár, J.; Braun, J.; Mankovsky, S.; Ebert, H. *J. Electron Spectrosc. Relat. Phenom.* **2011**, *184*, 91–99.

[58] Puschnig, P.; Berkebile, S.; Fleming, A. J.; Koller, G.; Emtsev, K.; Seyller, T.; Riley, J. D.; Ambrosch-Draxl, C.; Netzer, F. P.; Ramsey, M. G. *Science* **2009**, *326*, 702–706.

[59] Puschnig, P.; Ramsey, M. G. In *Encyclopedia of Interfacial Chemistry*; Elsevier: **2018**, 380–391.

[60] Puschnig, P.; Koller, G.; Draxl, C.; Ramsey, M. G. In *Small Organic Molecules on Surfaces*; Springer: **2013**, 3–23.

[61] Stöhr, J., *NEXAFS Spectroscopy*; Springer: 1993.

[62] Van der Laan, G. *J. Phys. Conf. Ser.* **2013**, *430*, 012127.

[63] Hähner, G. *Chem. Soc. Rev.* **2006**, *35*, 1244–1255.

[64] Cudia, C. C. et al. *Surf. Sci.* **2006**, *600*, 4013–4017.

[65] Stöhr, J.; Outka, D. A. *Phys. Rev. B* **1987**, *36*, 7891–7905.

[66] Floreano, L.; Cossaro, A.; Gotter, R.; Verdini, A.; Bavdek, G.; Evangelista, F.; Ruocco, A.; Morgante, A.; Cvetko, D. *J. Phys. Chem. C* **2008**, *112*, 10794–10802.

[67] Schütz, G.; Wagner, W.; Wilhelm, W.; Kienle, P.; Zeller, R.; Frahm, R.; Materlik, G. *Phys. Rev. Lett.* **1987**, *58*, 737–740.

[68] Thole, B. T.; Carra, P.; Sette, F.; van der Laan, G. *Phys. Rev. Lett.* **1992**, *68*, 1943–1946.

[69] Carra, P.; Thole, B. T.; Altarelli, M.; Wang, X. *Phys. Rev. Lett.* **1993**, *70*, 694–697.

[70] Stepanow, S.; Mugarza, A.; Ceballos, G.; Moras, P.; Cezar, J. C.; Carbone, C.; Gambardella, P. *Phys. Rev. B* **2010**, *82*, 014405.

[71] Stöhr, J. *J. Magn. Magn. Mater.* **1999**, *200*, 470–497.

[72] Kolasinski, K. W., *Surface Science*; Wiley: 2012.

[73] Lüth, H., *Solid Surfaces, Interfaces and Thin Films*; Springer: 2015.

[74] Voigtländer, B., *Scanning Probe Microscopy*; Springer: 2015.

[75] Binnig, G.; Rohrer, H.; Gerber, Ch.; Weibel, E. *Phys. Rev. Lett.* **1982**, *49*, 57–61.

[76] Bardeen, J. *Phys. Rev. Lett.* **1961**, *6*, 57–59.

[77] Tersoff, J.; Hamann, D. R. *Phys. Rev. B* **1985**, *31*, 805–813.

[78] Schneider, C. M.; Wiemann, C.; Patt, M.; Feyer, V.; Plucinski, L.; Krug, I. P.; Escher, M.; Weber, N.; Merkel, M.; Renault, O.; Barrett, N. *J. Electron Spectrosc. Relat. Phenom.* **2012**, *185*, 330–339.

[79] Floreano, L.; Naletto, G.; Cvetko, D.; Gotter, R.; Malvezzi, M.; Marassi, L.; Morgante, A.; Santaniello, A.; Verdini, A.; Tommasini, F.; Tondello, G. *Rev. Sci. Instrum.* **1999**, *70*, 3855–3864.

[80] Anthony, M. T.; Seah, M. P. *Surf. Interface Anal.* **1984**, *6*, 95–106.

[81] Seah, M. P.; Gilmore, I. S.; Beamson, G. *Surf. Interface Anal.* **1998**, *26*, 642–649.

[82] Piamonteze, C.; Flechsig, U.; Rusponi, S.; Dreiser, J.; Heidler, J.; Schmidt, M.; Wetter, R.; Calvi, M.; Schmidt, T.; Pruchova, H.; Krempasky, J.; Quitmann, C.; Brune, H.; Nolting, F. *J. Synchrotron Radiat.* **2012**, *19*, 661–674.

[83] Gambardella, P.; Rusponi, S.; Veronese, M.; Dhesi, S. S.; Grazioli, C.; Dallmeyer, A.; Cabria, I.; Zeller, R.; Dederichs, P. H.; Kern, K.; Carbone, C.; Brune, H. *Science* **2003**, *300*, 1130–1133.

[84] Gambardella, P. et al. *Nat. Mater.* **2009**, *8*, 189–193.

[85] Nguyen, G. D. et al. *Nat. Nanotechnol.* **2017**, *12*, 1077–1082.

[86] Kezilebieke, S.; Amokrane, A.; Boero, M.; Clair, S.; Abel, M.; Bucher, J.-P. *Nano Res.* **2014**, *7*, 888–897.

[87] Ullmann, F.; Bielecki, J. *Ber. Dtsch. Chem. Ges.* **1901**, *34*, 2174–2185.

[88] Ullmann, F. *Justus Liebigs Ann. Chem.* **1904**, *332*, 38–81.

[89] Xi, M.; Bent, B. E. *Surf. Sci.* **1992**, *278*, 19–32.

[90] Xi, M.; Bent, B. E. *J. Am. Chem. Soc.* **1993**, *115*, 7426–7433.

[91] Hla, S.-W.; Bartels, L.; Meyer, G.; Rieder, K.-H. *Phys. Rev. Lett.* **2000**, *85*, 2777–2780.

[92] McCarty, G. S.; Weiss, P. S. *J. Am. Chem. Soc.* **2004**, *126*, 16772–16776.

[93] Lackinger, M. *Chem. Commun.* **2017**, *53*, 7872–7885.

[94] Walch, H.; Gutzler, R.; Sirtl, T.; Eder, G.; Lackinger, M. *J. Phys. Chem. C* **2010**, *114*, 12604–12609.

[95] Björk, J.; Hanke, F.; Stafström, S. *J. Am. Chem. Soc.* **2013**, *135*, 5768–5775.

[96] Pham, T. A.; Song, F.; Nguyen, M.-T.; Li, Z.; Studener, F.; Stöhr, M. *Chem. Eur. J.* **2016**, *22*, 5937–5944.

[97] Fritton, M.; Duncan, D. A.; Deimel, P. S.; Rastgoo-Lahrood, A.; Allegretti, F.; Barth, J. V.; Heckl, W. M.; Björk, J.; Lackinger, M. *J. Am. Chem. Soc.* **2019**, *141*, 4824–4832.

[98] Wölfle, T.; Görling, A.; Hieringer, W. *Phys. Chem. Chem. Phys.* **2008**, *10*, 5739–5742.

[99] Donovan, P.; Robin, A.; Dyer, M. S.; Persson, M.; Raval, R. *Chemistry – A European Journal* **2010**, *16*, 11641–11652.

[100] Röckert, M.; Franke, M.; Tariq, Q.; Ditze, S.; Stark, M.; Uffinger, P.; Wechsler, D.; Singh, U.; Xiao, J.; Marbach, H.; Steinrück, H.-P.; Lytken, O. *Chem. Eur. J.* **2014**, *20*, 8948–8953.

[101] Xiang, F.; Gemeinhardt, A.; Schneider, M. A. *ACS Nano* **2018**, *12*, 1203–1210.

[102] Yin, C.; Peng, Z.; Liu, D.; Song, H.; Zhu, H.; Chen, Q.; Wu, K. *Molecules* **2020**, *25*, 3766.

[103] Lu, J.; Da, B.; Xiong, W.; Du, R.; Hao, Z.; Ruan, Z.; Zhang, Y.; Sun, S.; Gao, L.; Cai, J. *Phys. Chem. Chem. Phys.* **2021**, *23*, 11784–11788.

[104] Di Santo, G.; Blankenburg, S.; Castellarin-Cudia, C.; Fanetti, M.; Borghetti, P.; Sangaletti, L.; Floreano, L.; Verdini, A.; Magnano, E.; Bondino, F.; Pignedoli, C. A.; Nguyen, M.-T.; Gaspari, R.; Passerone, D.; Goldoni, A. *Chem. Eur. J.* **2011**, *17*, 14354–14359.

[105] Ruggieri, C.; Rangan, S.; Bartynski, R. A.; Galoppini, E. *J. Phys. Chem. C* **2016**, *120*, 7575–7585.

[106] Zamborlini, G.; Lüftner, D.; Feng, Z.; Kollmann, B.; Puschnig, P.; Dri, C.; Panighel, M.; Di Santo, G.; Goldoni, A.; Comelli, G.; Jugovac, M.; Feyer, V.; Schneider, C. M. *Nat. Commun.* **2017**, *8*, 1–8.

[107] Cojocariu, I.; Sturmeit, H. M.; Zamborlini, G.; Cossaro, A.; Verdini, A.; Floreano, L.; D'Incecco, E.; Stredansky, M.; Vesselli, E.; Jugovac, M.; Cinchetti, M.; Feyer, V.; Schneider, C. M. *Appl. Surf. Sci.* **2020**, *504*, 144343.

[108] Plekan, O.; Feyer, V.; Tsud, N.; Vondráček, M.; Cháb, V.; Matolín, V.; Prince, K. C. *Surf. Sci.* **2012**, *606*, 435–443.

[109] Simonov, K. A.; Vinogradov, N. A.; Vinogradov, A. S.; Generalov, A. V.; Zagrebina, E. M.; Mårtensson, N.; Cafolla, A. A.; Carpy, T.; Cunniffe, J. P.; Preobrajenski, A. B. *J. Phys. Chem. C* **2014**, *118*, 12532–12540.

[110] Fratesi, G.; Achilli, S.; Ugolotti, A.; Lodesani, A.; Picone, A.; Brambilla, A.; Floreano, L.; Calloni, A.; Bussetti, G. *Appl. Surf. Sci.* **2020**, *530*, 147085.

[111] Buchner, F.; Kellner, I.; Hieringer, W.; Görling, A.; Steinrück, H.-P.; Marbach, H. *Phys. Chem. Chem. Phys.* **2010**, *12*, 13082–13090.

[112] Wiengarten, A.; Seufert, K.; Auwärter, W.; Ecija, D.; Diller, K.; Allegretti, F.; Bischoff, F.; Fischer, S.; Duncan, D. A.; Papageorgiou, A. C.; Klappenberger, F.; Acres, R. G.; Ngo, T. H.; Barth, J. V. *J. Am. Chem. Soc.* **2014**, *136*, 9346–9354.

[113] Emtsev, K. V.; Speck, F.; Seyller, Th.; Ley, L.; Riley, J. D. *Phys. Rev. B* **2008**, *77*, 155303.

[114] Sala, A.; Zamborlini, G.; Menteş, T. O.; Locatelli, A. *Small* **2015**, *11*, 5927–5931.

[115] Galeotti, G. et al. *Nat. Mater.* **2020**, *19*, 874–880.

[116] Stredansky, M.; Sala, A.; Fontanot, T.; Costantini, R.; Africh, C.; Comelli, G.; Floreano, L.; Morgante, A.; Cossaro, A. *Chem. Commun.* **2018**, *54*, 3971–3973.

[117] Vasseur, G. et al. *Nat. Commun.* **2016**, *7*, 1–9.

[118] García-Fernández, C.; Sierda, E.; Abadía, M.; Bugenhagen, B.; Prosenc, M. H.; Wiesendanger, R.; Bazarnik, M.; Ortega, J. E.; Brede, J.; Matito, E.; Arnau, A. *J. Phys. Chem. C* **2017**, *121*, 27118–27125.

[119] Klappenberger, F. et al. *Small* **2018**, *14*, 1704321.

[120] Basagni, A.; Vasseur, G.; Pignedoli, C. A.; Vilas-Varela, M.; Peña, D.; Nicolas, L.; Vitali, L.; Lobo-Checa, J.; de Oteyza, D. G.; Sedona, F.; Casarin, M.; Ortega, J. E.; Sambi, M. *ACS Nano* **2016**, *10*, 2644–2651.

[121] Vasseur, G.; Abadia, M.; Miccio, L. A.; Brede, J.; Garcia-Lekue, A.; de Oteyza, D. G.; Rogero, C.; Lobo-Checa, J.; Ortega, J. E. *J. Am. Chem. Soc.* **2016**, *138*, 5685–5692.

[122] Krasnikov, S. A.; Preobrajenski, A. B.; Sergeeva, N. N.; Brzhezinskaya, M. M.; Nesterov, M. A.; Cafolla, A. A.; Senge, M. O.; Vinogradov, A. S. *Chem. Phys.* **2007**, *332*, 318–324.

[123] Krasnikov, S. A.; Sergeeva, N. N.; Brzhezinskaya, M. M.; Preobrajenski, A. B.; Sergeeva, Y. N.; Vinogradov, N. A.; Cafolla, A. A.; Senge, M. O.; Vinogradov, A. S. *J. Phys.: Condens. Matter* **2008**, *20*, 235207.

[124] Chen, M.; Feng, X.; Zhang, L.; Ju, H.; Xu, Q.; Zhu, J.; Gottfried, J. M.; Ibrahim, K.; Qian, H.; Wang, J. *J. Phys. Chem. C* **2010**, *114*, 9908–9916.

[125] Schmidt, N. A.; Fink, R.; Hieringer, W. *J. Chem. Phys.* **2010**, *133*, 054703.

[126] Cojocariu, I.; Carlotto, S.; Baranowski, D.; Jugovac, M.; Dreiser, J.; Schio, L.; Floreano, L.; Casarin, M.; Feyer, V.; Schneider, C. M. *J. Mater. Chem. C* **2023**, *11*, 15521–15530.

[127] Smykalla, L.; Shukrynau, P.; Korb, M.; Lang, H.; Hietschold, M. *Nanoscale* **2015**, *7*, 4234–4241.

[128] Cojocariu, I.; Feyersinger, F.; Puschnig, P.; Schio, L.; Floreano, L.; Feyer, V.; Schneider, C. M. *Chem. Commun.* **2021**, *57*, 3050–3053.

[129] Wang, H.; Butorin, S. M.; Young, A. T.; Guo, J. *J. Phys. Chem. C* **2013**, *117*, 24767–24772.

[130] Calabrese, A.; Floreano, L.; Verdini, A.; Mariani, C.; Betti, M. G. *Phys. Rev. B* **2009**, *79*, 115446.

[131] Zamborlini, G.; Jugovac, M.; Cossaro, A.; Verdini, A.; Floreano, L.; Lüftner, D.; Puschnig, P.; Feyer, V.; Schneider, C. M. *Chem. Commun.* **2018**, *54*, 13423–13426.

[132] Chen, M.; Xiao, J.; Steinrück, H.-P.; Wang, S.; Wang, W.; Lin, N.; Hieringer, W.; Gottfried, J. M. *J. Phys. Chem. C* **2014**, *118*, 6820–6830.

[133] Galeotti, G.; Di Giovannantonio, M.; Lipton-Duffin, J.; Ebrahimi, M.; Tebi, S.; Verdini, A.; Floreano, L.; Fagot-Revurat, Y.; Perepichka, D. F.; Rosei, F.; Contini, G. *Faraday Discuss.* **2017**, *204*, 453–469.

[134] Gutzler, R.; Cardenas, L.; Lipton-Duffin, J.; Garah, M. E.; Dinca, L. E.; Szakacs, C. E.; Fu, C.; Gallagher, M.; Vondráček, M.; Rybachuk, M.; Perepichka, D. F.; Rosei, F. *Nanoscale* **2014**, *6*, 2660–2668.

[135] Di Giovannantonio, M.; El Garah, M.; Lipton-Duffin, J.; Meunier, V.; Cardenas, L.; Fagot Revurat, Y.; Cossaro, A.; Verdini, A.; Perepichka, D. F.; Rosei, F.; Contini, G. *ACS Nano* **2013**, *7*, 8190–8198.

[136] Fan, Q.; Wang, T.; Liu, L.; Zhao, J.; Zhu, J.; Gottfried, J. M. *J. Chem. Phys.* **2015**, *142*, 101906.

[137] Sturmeit, H. M. et al. *J. Mater. Chem. C* **2020**, *8*, 8876–8886.

[138] Mallada, B.; Błoński, P.; Langer, R.; Jelínek, P.; Otyepka, M.; de la Torre, B. *ACS Appl. Mater. Interfaces* **2021**, *13*, 32393–32401.

[139] Fatayer, S.; Veiga, R. G. A.; Prieto, M. J.; Perim, E.; Landers, R.; Miwa, R. H.; de Siervo, A. *Phys. Chem. Chem. Phys.* **2015**, *17*, 18344–18352.

[140] Gargiani, P.; Rossi, G.; Biagi, R.; Corradini, V.; Pedio, M.; Fortuna, S.; Calzolari, A.; Fabris, S.; Cezar, J. C.; Brookes, N. B.; Betti, M. G. *Phys. Rev. B* **2013**, *87*, 165407.

[141] Stöhr, J.; König, H. *Phys. Rev. Lett.* **1995**, *75*, 3748–3751.

[142] Arruda, L. M.; Ali, Md. E.; Bernien, M.; Nickel, F.; Kopprasch, J.; Czekelius, C.; Oppeneer, P. M.; Kuch, W. *J. Phys. Chem. C* **2019**, *123*, 14547–14555.

[143] Cojocariu, I.; Windischbacher, A.; Baranowski, D.; Jugovac, M.; de Campos Ferreira, R. C.; Doležal, J.; Švec, M.; Zamalloa-Serrano, J. M.; Tormen, M.; Schio, L.; Floreano, L.; Dreiser, J.; Puschnig, P.; Feyer, V.; Schneider, C. M. *Adv. Sci.* **2023**, *10*, 2300223.

[144] Köbke, A. et al. *Nat. Nanotechnol.* **2020**, *15*, 18–21.

[145] Girovsky, J. et al. *Nat. Commun.* **2017**, *8*, 1–8.

[146] Stepanyuk, V. S.; Baranov, A. N.; Tsivlin, D. V.; Hergert, W.; Bruno, P.; Knorr, N.; Schneider, M. A.; Kern, K. *Phys. Rev. B* **2003**, *68*, 205410.

[147] Stepanyuk, V. S.; Niebergall, L.; Longo, R. C.; Hergert, W.; Bruno, P. *Phys. Rev. B* **2004**, *70*, 075414.

[148] Simon, E.; Újfalussy, B.; Lazarovits, B.; Szilva, A.; Szunyogh, L.; Stocks, G. M. *Phys. Rev. B* **2011**, *83*, 224416.

[149] Sun, Q.; Mateo, L. M.; Robles, R.; Ruffieux, P.; Bottari, G.; Torres, T.; Fasel, R.; Lorente, N. *Adv. Sci.* **2022**, *9*, 2105906.

[150] Cojocariu, I.; Carlotto, S.; Sturmeit, H. M.; Zamborlini, G.; Cinchetti, M.; Cossaro, A.; Verdini, A.; Floreano, L.; Jugovac, M.; Puschnig, P.; Piamonteze, C.; Casarin, M.; Feyer, V.; Schneider, C. M. *Chem. Eur. J.* **2021**, *27*, 3526–3535.

[151] Cojocariu, I.; Carlotto, S.; Zamborlini, G.; Jugovac, M.; Schio, L.; Floreano, L.; Casarin, M.; Feyer, V.; Schneider, C. M. *J. Mater. Chem. C* **2021**, *9*, 12559–12565.

[152] Carlotto, S.; Cojocariu, I.; Feyer, V.; Floreano, L.; Casarin, M. *Nanomaterials* **2022**, *12*, 218.

[153] Cojocariu, I.; Carlotto, S.; Baranowski, D.; Jugovac, M.; Schio, L.; Floreano, L.; Casarin, M.; Feyer, V.; Schneider, C. M. *Inorg. Chim. Acta* **2023**, *556*, 121657.

[154] Nalewajski, R. F.; Mrozek, J. *Int. J. Quantum Chem.* **1994**, *51*, 187–200.

[155] Zhao, C.-X.; Liu, X.; Liu, J.-N.; Wang, J.; Wan, X.; Wang, C.; Li, X.-Y.; Shui, J.; Song, L.; Peng, H.-J.; Li, B.-Q.; Zhang, Q. *Angew. Chem. Int. Ed.* **2023**, *62*, e202313028.

[156] Dong, L.; Gao, Z.; Lin, N. *Prog. Surf. Sci.* **2016**, *91*, 101–135.

[157] Tseng, T.-C.; Abdurakhmanova, N.; Stepanow, S.; Kern, K. *J. Phys. Chem. C* **2011**, *115*, 10211–10217.

[158] Torrente, I. F.; Franke, K. J.; Pascual, J. I. *Int. J. Mass Spectrom.* **2008**, *277*, 269–273.

[159] Faraggi, M. N.; Jiang, N.; Gonzalez-Lakunza, N.; Langner, A.; Stepanow, S.; Kern, K.; Arnau, A. *J. Phys. Chem. C* **2012**, *116*, 24558–24565.

[160] Fleischer, E. B. *Acc. Chem. Res.* **1970**, *3*, 105–112.

[161] Koudia, M.; Abel, M. *Chem. Commun.* **2014**, *50*, 8565–8567.

[162] Piantek, M.; Serrate, D.; Moro-Lagares, M.; Algarabel, P.; Pascual, J. I.; Ibarra, M. R. *J. Phys. Chem. C* **2014**, *118*, 17895–17899.

[163] Kezilebieke, S.; Amokrane, A.; Abel, M.; Bucher, J.-P. *J. Phys. Chem. Lett.* **2014**, *5*, 3175–3182.

[164] Nardi, E.; Chen, L.; Clair, S.; Koudia, M.; Giovanelli, L.; Feng, X.; Müllen, K.; Abel, M. *J. Phys. Chem. C* **2014**, *118*, 27549–27553.

[165] Zhao, Y.; Yuan, B.; Li, C.; Zhang, P.; Mai, Y.; Guan, D.; Li, Y.; Zheng, H.; Liu, C.; Wang, S.; Jia, J. *ChemPhysChem* **2019**, *20*, 2394–2397.

[166] Messina, P.; Dmitriev, A.; Lin, N.; Spillmann, H.; Abel, M.; Barth, J. V.; Kern, K. *J. Am. Chem. Soc.* **2002**, *124*, 14000–14001.

[167] Abdurakhmanova, N.; Floris, A.; Tseng, T.-C.; Comisso, A.; Stepanow, S.; De Vita, A.; Kern, K. *Nat. Commun.* **2012**, *3*, 1–7.

[168] Repp, J.; Meyer, G.; Paavilainen, S.; Olsson, F. E.; Persson, M. *Science* **2006**, *312*, 1196–1199.

[169] Albrecht, F.; Neu, M.; Quest, C.; Swart, I.; Repp, J. *J. Am. Chem. Soc.* **2013**, *135*, 9200–9203.

[170] Bässler, M.; Fink, R.; Buchberger, C.; Väterlein, P.; Jung, M.; Umbach, E. *Langmuir* **2000**, *16*, 6674–6681.

[171] Fraxedas, J.; Lee, Y. J.; Jiménez, I.; Gago, R.; Nieminen, R. M.; Ordejón, P.; Canadell, E. *Phys. Rev. B* **2003**, *68*, 195115.

[172] Pettersson, L. G. M.; Ågren, H.; Luo, Y.; Triguero, L. *Surf. Sci.* **1998**, *408*, 1–20.

[173] Chernenkaya, A.; Medjanik, K.; Nagel, P.; Merz, M.; Schuppler, S.; Canadell, E.; Pouget, J.-P.; Schönhense, G. *Eur. Phys. J. B* **2015**, *88*, 1–6.

[174] Ruehl, E.; Hitchcock, A. P. *J. Am. Chem. Soc.* **1989**, *111*, 5069–5075.

[175] Abdurakhmanova, N.; Tseng, T.-C.; Langner, A.; Kley, C. S.; Sessi, V.; Stepanow, S.; Kern, K. *Phys. Rev. Lett.* **2013**, *110*, 027202.

[176] Lindquist, J. M.; Hemminger, J. C. *Chem. Mater.* **1989**, *1*, 72–78.

[177] Diller, K.; Klappenberger, F.; Marschall, M.; Hermann, K.; Nefedov, A.; Wöll, Ch.; Barth, J. V. *J. Chem. Phys.* **2012**, *136*, 014705.

[178] Fujita, D.; Amemiya, K.; Yakabe, T.; Nejoh, H.; Sato, T.; Iwatsuki, M. *Surf. Sci.* **1999**, *423*, 160–168.

[179] Reinert, F.; Nicolay, G. *Appl. Phys. A* **2004**, *78*, 817–821.

[180] Haags, A.; Yang, X.; Egger, L.; Brandstetter, D.; Kirschner, H.; Bocquet, F. C.; Koller, G.; Gottwald, A.; Richter, M.; Gottfried, J. M.; Ramsey, M. G.; Puschnig, P.; Soubatch, S.; Tautz, F. S. *Sci. Adv.* **2022**, *8*, eabn0819.

[181] Bendounan, A.; Aït-Ouazzou, S. *J. Phys. Chem. C* **2016**, *120*, 11456–11464.

[182] Faraggi, M. N.; Golovach, V. N.; Stepanow, S.; Tseng, T.-C.; Abdurakhmanova, N.; Kley, C. S.; Langner, A.; Sessi, V.; Kern, K.; Arnau, A. *J. Phys. Chem. C* **2015**, *119*, 547–555.

[183] Abel, M.; Clair, S.; Ourdjini, O.; Mossoyan, M.; Porte, L. *J. Am. Chem. Soc.* **2011**, *133*, 1203–1205.

[184] Giovanelli, L.; Savoyant, A.; Abel, M.; Maccherozzi, F.; Ksari, Y.; Koudia, M.; Hayn, R.; Choueikani, F.; Otero, E.; Ohresser, P.; Themlin, J.-M.; Dhesi, S. S.; Clair, S. *J. Phys. Chem. C* **2014**, *118*, 11738–11744.

[185] Park, C.; Rojas, G. A.; Jeon, S.; Kelly, S. J.; Smith, S. C.; Sumpter, B. G.; Yoon, M.; Maksymovych, P. *Phys. Rev. B* **2014**, *90*, 125432.

[186] Shimooka, T.; Inukai, J.; Itaya, K. *J. Electrochem. Soc.* **2001**, *149*, E19.

[187] Klink, C.; Stensgaard, I.; Besenbacher, F.; Lægsgaard, E. *Surf. Sci.* **1995**, *342*, 250–260.

[188] Blowey, P. J.; Velari, S.; Rochford, L. A.; Duncan, D. A.; Warr, D. A.; Lee, T.-L.; De Vita, A.; Costantini, G.; Woodruff, D. P. *Nanoscale* **2018**, *10*, 14984–14992.

[189] Blowey, P. J.; Sohail, B.; Rochford, L. A.; Lafosse, T.; Duncan, D. A.; Ryan, P. T. P.; Warr, D. A.; Lee, T.-L.; Costantini, G.; Maurer, R. J.; Woodruff, D. P. *ACS Nano* **2020**, *14*, 7475–7483.

[190] Mousley, P. J.; Rochford, L. A.; Ryan, P. T. P.; Blowey, P.; Lawrence, J.; Duncan, D. A.; Hussain, H.; Sohail, B.; Lee, T.-L.; Bell, G. R.; Costantini, G.; Maurer, R. J.; Nicklin, C.; Woodruff, D. P. *J. Phys. Chem. C* **2022**, *126*, 7346–7355.

[191] Ryan, P.; Blowey, P. J.; Sohail, B. S.; Rochford, L. A.; Duncan, D. A.; Lee, T.-L.; Starrs, P.; Costantini, G.; Maurer, R. J.; Woodruff, D. P. *J. Phys. Chem. C* **2022**, *126*, 6082–6090.

[192] Mousley, P. J.; Rochford, L. A.; Hussain, H.; Moro, S.; Ding, P.; Bell, G. R.; Costantini, G.; Nicklin, C.; Woodruff, D. P. *J. Phys. Chem. C* **2023**, *127*, 4266–4272.

[193] Maccariello, D.; Garnica, M.; Niño, M. A.; Navío, C.; Perna, P.; Barja, S.; Vázquez de Parga, A. L.; Miranda, R. *Chem. Mater.* **2014**, *26*, 2883–2890.

[194] Wäckerlin, C.; Iacovita, C.; Chylarecka, D.; Fesser, P.; Jung, T. A.; Ballav, N. *Chem. Commun.* **2011**, *47*, 9146–9148.

[195] Blowey, P. J.; Rochford, L. A.; Duncan, D. A.; Warr, D. A.; Lee, T.-L.; Woodruff, D. P.; Costantini, G. *Faraday Discuss.* **2017**, *204*, 97–110.

[196] Yang, X.; Egger, L.; Fuchsberger, J.; Unzog, M.; Lüftner, D.; Hajek, F.; Hurdax, P.; Jugovac, M.; Zamborlini, G.; Feyer, V.; Koller, G.; Puschnig, P.; Tautz, F. S.; Ramsey, M. G.; Soubatch, S. *J. Phys. Chem. Lett.* **2019**, *10*, 6438–6445.

[197] Lüftner, D.; Weiß, S.; Yang, X.; Hurdax, P.; Feyer, V.; Gottwald, A.; Koller, G.; Soubatch, S.; Puschnig, P.; Ramsey, M. G.; Tautz, F. S. *Phys. Rev. B* **2017**, *96*, 125402.

[198] Knecht, P.; Reichert, J.; Deimel, P. S.; Feulner, P.; Haag, F.; Allegretti, F.; Garnica, M.; Schwarz, M.; Auwärter, W.; Ryan, P. T. P.; Lee, T.-L.; Duncan, D. A.; Seitsonen, A. P.; Barth, J. V.; Papageorgiou, A. C. *Angew. Chem. Int. Ed.* **2021**, *60*, 16561–16567.

[199] Jakub, Z.; Kurowská, A.; Herich, O.; Černá, L.; Kormoš, L.; Shahsavar, A.; Procházka, P.; Čechal, J. *Nanoscale* **2022**, *14*, 9507–9515.

[200] Hermanns, C. F.; Tarafder, K.; Bernien, M.; Krüger, A.; Chang, Y.-M.; Oppeneer, P. M.; Kuch, W. *Adv. Mater.* **2013**, *25*, 3473–3477.

[201] Candini, A.; Bellini, V.; Klar, D.; Corradini, V.; Biagi, R.; De Renzi, V.; Kummer, K.; Brookes, N. B.; del Pennino, U.; Wende, H.; Affronte, M. *J. Phys. Chem. C* **2014**, *118*, 17670–17676.

[202] Avvisati, G.; Cardoso, C.; Varsano, D.; Ferretti, A.; Gargiani, P.; Betti, M. G. *Nano Lett.* **2018**, *18*, 2268–2273.

[203] Kutnyakhov, D. et al. *Ultramicroscopy* **2013**, *130*, 63–69.

[204] Te Velde, G.; Bickelhaupt, F. M.; Baerends, E. J.; Guerra, C. F.; van Gisbergen, S. J. A.; Snijders, J. G.; Ziegler, T. *J. Comput. Chem.* **2001**, *22*, 931–967.

[205] Perdew, J. P. *Phys. Rev. B* **1986**, *33*, 8822–8824(R).

[206] Becke, A. D. *Phys. Rev. A* **1988**, *38*, 3098–3100.

[207] Grimme, S.; Ehrlich, S.; Goerigk, L. *J. Comput. Chem.* **2011**, *32*, 1456–1465.

[208] Mulliken, R. S. *J. Chem. Phys.* **1955**, *23*, 1833–1840.

[209] Brandstetter, D.; Yang, X.; Lüftner, D.; Tautz, F. S.; Puschnig, P. *Comput. Phys. Commun.* **2021**, *263*, 107905.

[210] Aprà, E. et al. *J. Chem. Phys.* **2020**, *152*, 184102.

[211] Kresse, G.; Hafner, J. *Phys. Rev. B* **1993**, *47*, 558–561(R).

[212] Kresse, G.; Joubert, D. *Phys. Rev. B* **1999**, *59*, 1758–1775.

[213] Perdew, J. P.; Burke, K.; Ernzerhof, M. *Phys. Rev. Lett.* **1996**, *77*, 3865–3868.

[214] Dudarev, S. L.; Botton, G. A.; Savrasov, S. Y.; Humphreys, C. J.; Sutton, A. P. *Phys. Rev. B* **1998**, *57*, 1505–1509.

[215] Neugebauer, J.; Scheffler, M. *Phys. Rev. B* **1992**, *46*, 16067–16080.

[216] Carrillo-Aravena, E.; Finzel, K.; Ray, R.; Richter, M.; Heider, T.; Cojocariu, I.; Baranowski, D.; Feyer, V.; Plucinski, L.; Gruschwitz, M.; Tegenkamp, C.; Ruck, M. *Phys. Status Solidi B* **2022**, *259*, 2100447.

[217] Janas, D. M. et al. *Inorg. Chim. Acta* **2023**, *557*, 121705.

[218] Tan, X. L.; Hagiwara, K.; Chen, Y.-J.; Schusser, J.; Cojocariu, I.; Baranowski, D.; Feyer, V.; Minár, J.; Schneider, C. M.; Tusche, C. *Ultramicroscopy* **2023**, *253*, 113820.

[219] Chesnyak, V.; Cuxart, M. G.; Baranowski, D.; Seufert, K.; Cojocariu, I.; Jugovac, M.; Feyer, V.; Auwärter, W. *Small* **2023**, *20*, 2304803.

[220] Strasdas, J. et al. *Nano Lett.* **2023**, *23*, 10342–10349.

A Appendix

A.1 Theoretical Modeling of Covalent Nickel Tetraphenylporphyrin Network

The calculations presented in chapter 4 have been performed by Carlotto, S. and Casarin, M.. Thereby, the Amsterdam Density Functional (ADF) software package has been used for geometry optimization calculations.[204] For optimized geometrical parameters spin-unrestricted, nonrelativistic density functional theory calculations have been performed. Self-consistent generalized gradient corrections are included through the B3LYP[205,206] functional used and through a triple-ζ adaption characterized by a polarization function Slater-type basis set for all atoms. Grimme dispersion corrections have been further included.[207] In accordance with previous studies, a molecular cluster has been considered for the interaction of dh-NiTPP with the Cu(111) substrate.[143,150–153] The Ni-Cu distance (2.1 Å) obtained from periodic calculations on similar systems, where the central Ni centers of porphyrins were experiencing similar charge transfer and consequently reduced to Ni(I) on Cu(100), has been used thereby.[106] Calculations on the NiTPP network have been performed analogously. The obtained ground state theoretical results have been displayed graphically as the partial density of states (PDOS) at a Lorentzian broadening factor of 250 meV (or 5 meV) for better comprehensibility. From overlap densities that have been partitioned within the Mulliken approach, molecular orbitals (MOs) can easily be inspected based on the contribution from different atoms. PDOS are calculated as:

$$\mathrm{PDOS}_{\mathrm{nl}}^{\upsilon}(E) = \sum_{\mathrm{p}} \frac{\gamma f_{\mathrm{nl}}^{\upsilon}}{\pi(E - E_{\mathrm{p}})} \tag{A.1}$$

where γ denotes the Lorentzian broadening factor and $f_{\mathrm{nl}}^{\upsilon}$ is the Mulliken's population contribution from atom υ, state (nl) to the pth MO of energy E_{p}.[208] The isosurfaces for displayed contour plots of selected MOs correspond to $\pm\ 0.03 \cdot e^{1/2} \cdot \text{Å}^{-3/2}$.

A.2 Photoemission Orbital Tomography and Theoretical Modeling of Metal-Organic Nickel-1,2,4,5-Tetracyanobenzene Nanostructures

The calculations presented in chapter 5 have been performed by Brandstetter, D., Windischbacher, A. and Puschnig, P.. Thereby, the kMap.py program has been used for the simulation of the TCNB photoemission patterns.[209] TCNB gas-phase MOs, used thereby, have been calculated at the B3LYP level of theory with 6-31G* basis sets using the NWChem 7.0.2 package.[210]

The clarification of the electronic structure of the (metal-)organic layers required advanced theoretical modeling. To this end, ground state DFT calculations using the Vienna Ab-initio Simulation Package (VASP) versions 6.4.1 on the Vienna Scientific Cluster 5 (VSC-5) and 5.4.4 on VSC-4 have been conducted.[211,212] The exchange-correlation effects have been incorporated via the Perdew-Burke-Enzerdorf generalized gradient approximation (PBE-GGA)[213] with a Grimme D3 van der Waals correction with Becke-Johnson damping.[207] Within such an GGA-type xc-function, the inclusion of some form of self-interaction error correction for the strongly localized *d*-orbitals in the transition metal is crucial for an accurate model of the hybridization observed in the experiments. Therefore, an effective Hubbard-U parameter of 3 eV using the Dudarev ansatz has been added.[214] Starting with the experimentally determined structures, all systems have been relaxed until all atomic forces are below 0.01 eV/Å. The interface has been modeled in the repeated slab approach with a 15 Å vacuum layer, adding a dipole layer within the vacuum region to address the electric field discrepancy between either side of the slab.[215] The bulk of the silver substrate has been represented by five layers in total, allowing relaxation only in the top two layers during geometry optimization. The first Brillouin zone has been sampled using a Γ-centered 8x8x1 grid. For the simulation of the photoelectron distribution, the photoemission process has been simulated as a one-step process where the final state has been approximated as a plane wave. Additionally, we included a damping of the substrate emissions according to [197] of $\Gamma = 0.5$ Å^{-1}.

List of Tables

List of Figures

Acknowledgments

With the conclusion of this dissertation, a significant chapter of my life comes to an end. The narrative of this chapter would not have been complete without the involvement of many people. Therefore, I would like to express my utmost gratitude to everyone who helped me reaching this point.

I extend my sincere thanks to my dissertation advisor, Prof. Dr. Claus M. Schneider, for consistently holding meetings and being readily available for valuable feedback. I am deeply appreciative of his ongoing support and reliability. Despite the limited opportunities to meet in Jülich, he ensured that I had a welcoming place in his office, especially after enduring heavy rainfall in the research center area.

I express my gratitude to my daily supervisor in Trieste, Dr. Vitaliy Feyer, for his day-to-day guidance, offered with great spirit and enthusiasm right from the beginning on. His positive attitude, permanent reachability and enduring excitement has created an encouraging work atmosphere.

I want to thank all current and former members of PGI-6 who have been involved throughout this period. Specifically, I convey my gratitude to Dr. Iulia Cojocariu, who was about to complet her Ph.D. when I joined the group. Thanks to her hard-working attitude, I have had the opportunity to learn many things from her and to benefit from her ongoing support, which continues to this day. I am happy that Simone Mearini has joined the group with me at the same state as Dr. Iulia Cojocariu was when I joined the group. He has brought sunshine from the south of Italy to Trieste. I would like to further thank Margret Frey for helping with any bureaucratic obstacle I have experienced during this journey.

Working at a beamline has proven to be an exciting experience. I am sincerely grateful for the opportunity to work with users and being involved in other projects, which has expanded my view on the world.

I have been further fortunate to have had Dr. Matteo Jugovac as a neighbor, a former Ph.D. student of PGI-6 offering his support in every emergency situation and beeing available for any advice. I also want to thank my other great neighbors Carlo A. Brondin, who provided me with great moral support and engaging discussions, and Dr. Tevfik O. Menteş, a superb teacher who has been always available whenever I encountered difficulties.

I am grateful and want to acknowledge the great collaboration with the members of the TASC laboratory in Trieste. Working with Dr. Alessandro Sala, Dr. Valeria Chesnyak, Dr. Cristina Africh and Prof. Giovanni Comelli from the STRAS laboratory, as well as Dr. Massimo Tormen, Carolina Gutiérrez Bolaños, Dr. Luca Schio and Dr. Luca Floreano from the ALOISA beamline

has been a truly enriching experience. Whenever I have joined the respective facility, I have felt warmly welcomed, not just in a professional sense, but in an accustomed one as well. A special thanks goes to Dr. Alessandro Sala for his leading contribution to STM experiments and analysis with immersive commitment, and to il gentile signor Dr. Luca Floreano for the endless amount of fruitful discussions, each unique on its own right.

I am thankful to Dr. Silvia Carlotto and Prof. Dr. Maurizio Casarin from the University of Padova for enriching the experimental findings by their theoretical support. I have savored the kind atmosphere around them and their tremendous helpfulness throughout.

I gratefully appreciate the opportunity to conduct a visiting student period at the University of Innsbruck. Thereby, I have had the pleasure to work with Marco Thaler and Prof. Dr. Laerte L. Patera. I am beholden to them for making my stay abroad so pleasant and exciting while leading STM experiments with extraordinary involvement.

I am indebted to Dr. Jan Dreiser for helping with the XMCD experiments at the X-Treme beamline and his valuable feedback in the process of data analysis. He has been eagerly involved in various meetings where I had the opportunity to benefit from his expertise.

I express my gratitude to Dominik Brandstetter, Dr. Andreas Windischbacher and Prof. Dr. Peter Puschnig from the University of Graz for performing calculations to corroborate the experimental observations. I really appreciate their invaluable dedication and their readiness to carry out numerous iterations with lively exchange.

I convey my heartfelt appreciation to my family and friends for their continuous and unconditional support, without which I would not be here. I extend my gratitude to my partner for her patience, encouragement, and her family as well.

Curriculum Vitae

Personal Data

Name	Daniel Baranowski
Birthdate	Mar 9, 1996
Birthplace	Traunstein, Germany
Nationality	German

Education

Ph.D. student Dec, 2020–Jun, 2024	PGI-6, Jülich Research Center
M.Sc. in Chemistry Oct, 2017–Sep, 2020	Technical University of Munich
B.Sc. in Chemistry Oct, 2014–Sep, 2017	Technical University of Munich
High-school diploma Sep, 2006–Jun, 2014	Johannes-Heidenhain Gymnasium Traunreut

Publications

Articles

- Conservation of Nickel Ion Single-Active Site Character in a Bottom-Up Constructed π-Conjugated Molecular Network by **Baranowski, D.**; Cojocariu, I.; Sala, A.; Africh, C.; Comelli, G.; Schio, L.; Tormen, M.; Floreano, L.; Feyer, V.; Schneider, C. M. in *Angew. Chem. Int. Ed.* **2022**, *61*, e202210326.[39]
- $Bi_{12}Rh_3Cu_2I_5$: A 3D Weak Topological Insulator with Monolayer Spacers and Independent Transport Channels by Carrillo-Aravena, E.; Finzel, K.; Ray, R.; Richter, M.; Heider, T.; Cojocariu, I.; **Baranowski, D.**; Feyer, V.; Plucinski, L.; Gruschwitz, M.; Tegenkamp, C.; Ruck, M. in *Phys. Status Solidi B* **2022**, *259*, 2100447.[216]
- Surface-Mediated Spin Locking and Thermal Unlocking in a 2D Molecular Array by Cojocariu, I.; Windischbacher, A.; **Baranowski, D.**; Jugovac, M.; de Campos Ferreira, R. C.; Doležal, J.; Švec, M.; Zamalloa-Serrano, J. M.; Tormen, M.; Schio, L.; Floreano, L.; Dreiser, J.; Puschnig, P.; Feyer, V.; Schneider, C. M. in *Adv. Sci.* **2023**, *10*, 2300223.[143]
- Substitutional flexibility and molecular pinning in porphyrin-based interfaces sensitive to NO_2 by Cojocariu, I.; Carlotto, S.; **Baranowski, D.**; Jugovac, M.; Schio, L.; Floreano, L.; Casarin, M.; Feyer, V.; Schneider, C. M. in *Inorg. Chim. Acta* **2023**, *556*, 121657.[153]
- Metalloporphyrins on oxygen-passivated iron: Conformation and order beyond the first layer by Janas, D. M. et al. in *Inorg. Chim. Acta* **2023**, *557*, 121705.[217]
- Soft X-ray Fermi surface tomography of palladium and rhodium via momentum microscopy by Tan, X. L.; Hagiwara, K.; Chen, Y.-J.; Schusser, J.; Cojocariu, I.; **Baranowski, D.**; Feyer, V.; Minár, J.; Schneider, C. M.; Tusche, C. in *Ultramicroscopy* **2023**, *253*, 113820.[218]
- Stripe-Like hBN Monolayer Template for Self-Assembly and Alignment of Pentacene Molecules by Chesnyak, V.; Cuxart, M. G.; **Baranowski, D.**; Seufert, K.; Cojocariu, I.; Jugovac, M.; Feyer, V.; Auwärter, W. in *Small* **2023**, *20*, 2304803.[219]
- Extended π-conjugation: a key to magnetic anisotropy preservation in highly reactive porphyrins by Cojocariu, I.; Carlotto, S.; **Baranowski, D.**; Jugovac, M.; Dreiser, J.; Schio, L.; Floreano, L.; Casarin, M.; Feyer, V.; Schneider, C. M. in *J. Mater. Chem. C* **2023**, *11*, 15521–15530.[126]
- Electronic Band Structure Changes across the Antiferromagnetic Phase Transition of Exfoliated $MnPS_3$ Flakes Probed by μ-ARPES by Strasdas, J. et al. in *Nano Lett.* **2023**, *23*, 10342–10349.[220]

- Tuning Transition Metal-Containing Molecular Magnets by On-Surface Polymerization by **Baranowski, D.**; Cojocariu, I.; Schio, L.; Gutiérrez Bolaños, C.; Floreano, L.; Dreiser, J.; Carlotto, S.; Casarin, M.; Feyer, V.; Schneider, C. M. in *Adv. Mater. Interfaces* **2024**, 2400123.[40]
- Emergence of band structure in a two-dimensional metal-organic framework upon hierarchical self-assembly by **Baranowski, D.**; Thaler, M.; Brandstetter, D.; Windischbacher, A.; Cojocariu, I.; Mearini, S.; Chesnyak, V.; Schio, L.; Floreano, L.; Gutiérrez Bolaños, C.; Puschnig, P.; Patera, L. L.; Feyer, V.; Schneider, C. M. in *Submitted to ACS Nano* **2024**.[41]

Conference Contributions

- Single-active site character of Ni ion cores in two-dimensional network based on covalently linked NiTPP units (Talk) by **Baranowski, D.**; Cojocariu, I.; Sala, A.; Africh, C.; Comelli, G.; Schio, L.; Tormen, M.; Floreano, L.; Feyer, V.; Schneider, C. M. at *EWEG/2D* **2022**.
- Conservation of Nickel Ion Single-Active Site Character in a Bottom-Up Constructed π-Conjugated Molecular Network (Poster) by **Baranowski, D.**; Cojocariu, I.; Sala, A.; Africh, C.; Comelli, G.; Schio, L.; Tormen, M.; Floreano, L.; Feyer, V.; Schneider, C. M. at *747. WE-Heraeus-Seminar* **2023**.
- Angle-resolved photoemission mapping of hybrid states characteristic of metal-organic nanostructures (Talk) by **Baranowski, D.**; Thaler, M.; Brandstetter, D.; Windischbacher, A.; Cojocariu, I.; Mearini, S.; Chesnyak, V.; Schio, L.; Floreano, L.; Gutiérrez Bolaños, C.; Puschnig, P.; Patera, L. L.; Feyer, V.; Schneider, C. M. at *36. Symposium on Surface Science* **2024**.

Erklärung

Hiermit erkläre ich, dass ich die eingereichte Dissertation zur Erlangung des Doktorgrades Dr. rer. nat. selbstständig verfasst habe. Bei der Abfassung dieser Dissertation habe ich nur die angegebenen Hilfsmittel benutzt und wörtlich oder inhaltlich übernommenen Stellen als solche gekennzeichnet. Die Dissertation habe ich nur in diesem Promotionsverfahren eingereicht. Ich erkläre, dass ich bisher keine erfolglosen Promotionsversuche in diesem oder einem anderen Fach unternommen habe. Außerdem erkläre ich, dass das Promotionsverfahren nicht durch eine kommerzielle Vermittlung des Betreuungsverhältnisses oder sonstige prüfungsrechtlich unzulässige und wissenschaftlich unvertretbare entgeltliche oder unentgeltliche Hilfe Dritter zustande gekommen ist.

Daniel Baranowski

Jülich, 21.06.2024

Band / Volume 271
Neutron scattering
Experimental Manuals of the JCNS Laboratory Course held at Forschungszentrum Jülich and at the Heinz-Maier-Leibnitz Zentrum Garching
edited by T. Brückel, S. Förster, K. Friese, M. Kruteva, M. Zobel and R. Zorn
(2023), ca 150 pp
ISBN: 978-3-95806-705-9

Band / Volume 272
Ab-initio investigation of the interplay between the hyperfine interaction and complex magnetism at the nanoscale
S. R. S. Shehada (2023), ix, xi, 119 pp
ISBN: 978-3-95806-718-9

Band / Volume 273
Analysis of the signal transduction cascade tuning the 2-oxoglutarate dehydrogenase activity in *Corynebacterium glutamicum*
L. Sundermeyer (2023), VI, 119 pp
ISBN: 978-3-95806-722-6

Band / Volume 274
Multicellular defense against phage infection in *Streptomyces* – impact of secondary metabolites and mycelial development
L. Kever (2023), iv, 246 pp
ISBN: 978-3-95806-724-0

Band / Volume 275
Investigation of the electronic band structure of 2D transition metal dichalcogenides via angle-resolved photoemission spectroscopy
B. Parashar (2023), xvii, 156 pp
ISBN: 978-3-95806-725-7

Band / Volume 276
Strain- and process engineering for polyketides production with *Pseudomonas taiwanensis* VLB120 in two-phase cultivations
T. P. Schwanemann (2023), 230 pp
ISBN: 978-3-95806-726-4

Band / Volume 277
Quantitative atomic-level investigation of solid materials through multidimensional electron diffraction measurements
H. L. Lalandec-Robert (2024), xxi, 152 pp
ISBN: 978-3-95806-735-6

Schriften des Forschungszentrums Jülich
Reihe Schlüsseltechnologien / Key Technologies

Band / Volume 278
Studies on the cAMP-responsive regulatory network of *Corynebacterium glutamicum*
N. Wolf (2024), iii, 122 pp
ISBN: 978-3-95806-736-3

Band / Volume 279
Rare-earth atoms on two-dimensional materials: ab initio investigation of magnetic properties
J. P. Carbone (2024), 235 pp
ISBN: 978-3-95806-740-0

Band / Volume 280
Communities of Niche-optimized Strains (CoNoS) –
a novel concept for improving biotechnological production
R. Zuchowski (2024), VIII, 168 pp
ISBN: 978-3-95806-743-1

Band / Volume 281
Enabling mixed microbial upcycling of plastic monomers
Y. S. Ackermann (2024), XVI, 203 pp
ISBN: 978-3-95806-749-3

Band / Volume 282
Folding and structural studies of *saccharomyces cerevisiae* Phosphoglycerate Kinase
N. Bustorff (2024), xxvi, 126 pp
ISBN: 978-3-95806-754-7

Band / Volume 283
The role of cellular development in multicellular antiphage
defense of *Streptomyces*
T. Luthe (2024), vi, 173 pp
ISBN: 978-3-95806-768-4

Band / Volume 284
Probing the Transformation from Transition Metal Complexes to Extended Two-Dimensional Nanostructures
D. Baranowski (2024), XII, 103 pp
ISBN: 978-3-95806-772-1

Weitere ***Schriften des Verlags im Forschungszentrum Jülich*** unter
http://wwwzb1.fz-juelich.de/verlagextern1/index.asp

Schlüsseltechnologien / Key Technologies
Band / Volume 284
ISBN 978-3-95806-772-1

Mitglied der Helmholtz-Gemeinschaft

JÜLICH
Forschungszentrum